ECAP-2018-029

Design and characterization of an intensity interferometer with thermal light sources

Master's Thesis in Physics

Presented by

Andreas Zmija

19.12.2018

Erlangen Centre for Astroparticle Physics
Friedrich-Alexander-Universität Erlangen-Nürnberg

Supervisor: **Prof. Dr. Gisela Anton**
Co-advisor: **PD Dr. Thilo Michel**

Overview

Intensity interferometry can be used to determine the **angular sizes of stars**. It is an alternative to the conventional amplitude interferometry. Amplitude interferometers measure the interference pattern of starlight at different positions. Hence extreme high accuracy of measuring the electromagnetic waves is required. In contrast, intensity interferometers make use of a property of chaotic light sources called "**photon bunching**". **Intensity fluctuations** of such light sources are **correlated** at different positions in the observation plane. This effect can be analyzed by detecting the arriving photons at two detector-telescopes. The advantage is that this method is insensitive to the phases of electromagnetic waves. Hence increasing telescope baselines are possible without restrictions due to atmospheric turbulences. This allows for measuring smaller and smaller angular diameters.
The first stellar intensity interferometer was successfully developed by Hanbury Brown and Twiss already in the late 1950s [1][2]. Due to these two pioneers such an intensity interferometry experiment is also called "**Hanbury Brown-Twiss experiment**".
However, there are difficulties in detecting bunching signals of light sources with a broad wavelength spectrum. The height of these signals in the so-called **second-order correlation function** is indirect proportional to the optical bandwidth of the detected light and the time resolution of the detection system. Electronics providing a high time resolution are needed to measure a significant signal. These challenging requirements are the reasons why the concept of stellar intensity interferometry was not pursued forceful since Hanbury Brown and Twiss until nowadays.

In this thesis a setup for intensity interferometry is tested. By time tagging the arrival times of photons in two detectors their correlations can be analyzed. The correlations are calculated by a software that is written. Time differences of the photons are computed, in this way the bunching signal can be evaluated out of the raw time tags. The (temporal) correlation signals of three different light sources are measured for this thesis. At first, a **laser** illuminating a **rotating ground glass disc** is taken. This artificial chaotic light source generates a big correlation signal and is a convenient source for first tests. Afterwards a **mercury lamp** with a shorter **coherence time** and finally a **light-emitting diode** are used. The LED is the most challenging one, its light has to be optical bandwidth-filtered to see a bunching signal. The LED is a suitable light source to simulate measuring a star in the lab.

Contents

1. Introduction to intensity interferometry

To understand the benefits of intensity interferometry it is useful to recall conventional methods of star observations. Michelson interferometers replaced traditional telescopes as standard instrument for optical investigation of stars. However, Michelson interferometry has already been improved to observation limits restricted by atmospheric turbulences. For measuring even smaller objects in angular size intensity interferometers which have not been established yet seem to overcome these challenges and may be predestined to be used when reaching increasing angular resolution.
Since intensity interferometers rely on optical coherence effects the term *coherence* is introduced in this section as well as quantification of it in terms of the first- and second-order correlation functions. Some theorems and relations that are given allow the calculations of the correlation functions for known source parameters. Reversely the source geometry can be deduced up to some limits from measurement of the correlation functions.
Possible realizations of intensity interferometers are discussed as well to demonstrate the - in principle - manageable way of setting up intensity interferometers by i.e. implementing intensity interferometry electronics in large telescope arrays.

Contents

1.1. Observations of stars

1.1.1. Image-resolving of stars

Looking at the sun (of course using special sunlight filters or glasses) immediately reveals that the sun is extent even if no telescope is used. One can see a disc with a similar angular diameter as the moon, therefore it is no problem to image the disc of the sun. The angular diameter is $\alpha_{\text{sun}} \approx 30\,\text{arcmin}$ [3]. However, all other stars cannot be resolved by the naked eye, when looking into the sky at night one actually does not see stars but starlight extended by atmospheric fluctuations.
Even telescopes are struggling to resolve stars other than the sun. The resolution of an ideal telescope is diffraction-limited. A telescope with a circular aperture D produces an interference pattern in the observation plane with the first minimum at $\sin\alpha = 1.22\frac{\lambda}{D}$, where λ is the wavelength of the observed light [4]. Such an interference pattern is produced by plane waves. Another point of the star with a different incident angle produces a pattern shifted in the observation plane. When the two interference maxima are close together which holds for light beams with a small mutual angle the two points cannot be resolved any more. One usually sets the first minimum of one diffraction pattern as minimum distance criterion for resolving the other point (Rayleigh Criterion)[5]. Therefore the angular resolution α_{min} of a traditional telescope can be determined from its aperture D.

$$\alpha_{\text{min}} \approx \sin\alpha_{\text{min}} = 1.22\frac{\lambda}{D} \tag{1.1}$$

The bigger the aperture the better the optical resolution. However, large lens or mirror telescopes are rare, expensive and challenging. The biggest optical telescopes nowadays have mirror diameters of about 10 m [6]. Observing in the optical range at i.e. $\lambda = 550\,\text{nm}$ the resolution is restricted to $1.22 \cdot \frac{550\,\text{nm}}{10\,\text{m}} = 13\,\text{mas}$.

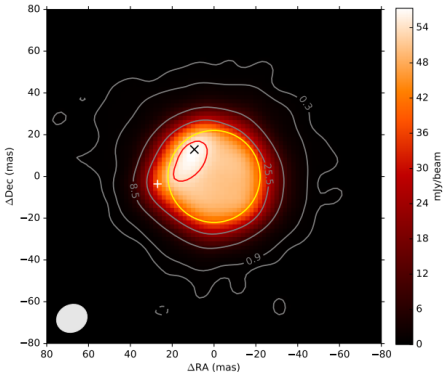

Figure 1.1.: Image of Betelgeuse taken with the ALMA telescope array. Taken from [7]

The Atacama Large Millimeter/submillimeter Array (ALMA) in Chile resolved the red supergiant Betelgeuse using different wavelengths in the range of 275 to 373 GHz ($\approx 0.8 - 1\,\text{mm}$) corresponding to infrared/radio part of the electromagnetic spectrum [8][7]. In figure 1.1 it can be seen that the angular diameter in both dimensions is $\alpha_{\text{Betelgeuse}} \approx 50\,\text{mas}$.

While there are still some star properties visible like the non-circular shape of Betelgeuse, it gets even more difficult at smaller angular diameters. It should be mentioned that even the ALMA telescope is an array of telescopes not acting like a conventional telescope but as an interferometer [8].

1.1.2. Michelson interferometry

Michelson interferometry has established as standard method of measuring the angular diameters of stars to date. A Michelson stellar interferometer actually acts as a double slit interferometer with variable distance D between the slits. Observed is the interference pattern produced by the slits coherently illuminated by the star. Figure 1.2 visualizes the parameters used below. The angle of the first minimum of the pattern is

$$\sin\alpha \approx \alpha \approx \frac{g_1}{L} = \frac{s}{D} \tag{1.2}$$

where s is the difference in distance of the scattered beams from the slit to the detector plane and $s = \frac{\lambda}{2}$ for a minimum as the two light waves from the slits cancel out then. Therefore it holds

$$g_1 = \frac{\lambda L}{2D} \tag{1.3}$$

The interference pattern shows clear maxima and minima when the source is point-like. However, when the source is extent each point of the surface produces its own interference pattern with shifted positions.

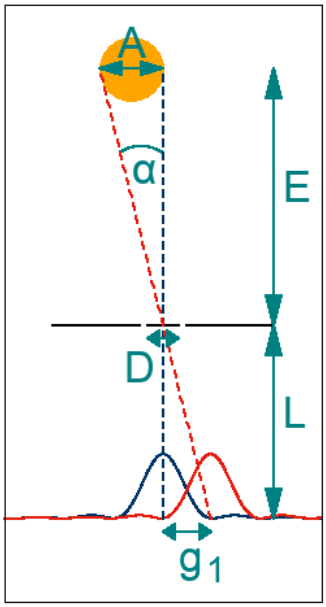

Figure 1.2.: Michelson stellar interferometer principle

When the main maximum of the "left" margin of the star matches with the position of the first minimum of the "right" margin the interference pattern vanishes. This happens when

$$\frac{g_1}{L} = \frac{A}{E} \Rightarrow \frac{\lambda}{2D} = \frac{A}{E} = \alpha \tag{1.4}$$

By increasing the baseline distance D the visibility of the interference pattern decreases until the pattern vanishes at $\alpha = \frac{\lambda}{2D}$.

The advantage of stellar interferometers compared to traditional "normal" telescopes is the long baseline. An optical telescope needs large aperture diameters to resolve small objects. Interferometers do not, important is the distance between two or more telescopes.
Measurements with the Mark III optical interferometer between 1988 and 1990 revealed angular diameters of 85 stars down to 2 mas with uncertainties of tens of a microarcsecond using a maximum baseline of 31.5 m [9]. The CHARA Array on Mount Wilson provides baselines up to 330 m allowing measurements of angular diameters of 0.2 mas with uncertainties of only 7 microarcseconds [10].
Amplitude interferometers have to deal with major challenges, since amplitude interferometry requests coherence of the light detected at the different telescopes. Electromagnetic waves must be detected with a **precision smaller than a wavelength of the observed light** at the two detection points to still recognize the interference. For optical telescopes sub-micrometer precision is demanded. However, atmospheric turbulences and the fact that the light from the different telescopes has to be brought together with the same precision make Michelson interferometry practical impossible for kilometer baselines or more.

1.1.3. The Hanbury Brown-Twiss (HBT) interferometer

A way out of this dilemma is intensity interferometry not measuring light amplitudes at different positions but intensities, collecting photons in other words. To be more precise, intensity interferometers measure correlated intensity fluctuations being insensitive to the phases of the electromagnetic waves.
Already in 1956 Hanbury Brown and Twiss made use of the correlations of intensities of starlight to determine the diameter of Sirius using a primitive equipment with two mirrors focusing starlight on photo-multipliers, whose signals were multiplied [1]. Between 1964 and 1972 they continued intensity interferometry measurements with the Narrabri Stellar Intensity Interferometer seen in figure **1.3**. The circular railway has a diameter of 188 m which is the longest possible baseline. Angular sizes down to (0.41 ± 0.03) mas were measured with this interferometer [2].
The advantage of an intensity interferometer lies in the fact that it is not measuring amplitudes but numbers of photons. Hence, atmospheric turbulences which change the phase of an electromagnetic wave on nanometer scale do not disturb the measurement totally. Rather it is important that the time difference of two originally correlated photons arriving in the two detectors does not become too large due to atmosphere. However, since the time difference will be convoluted with the time resolution of the system which is in the range of nanoseconds, the spatial sensitivity needed for a successful measurement is not in the range of nanometers any more but in the range of $c \cdot 1\,\text{ns} \approx 30\,\text{cm}$. Furthermore the photons are detected at the distant photodetectors, the signals then can be carried electronically to the

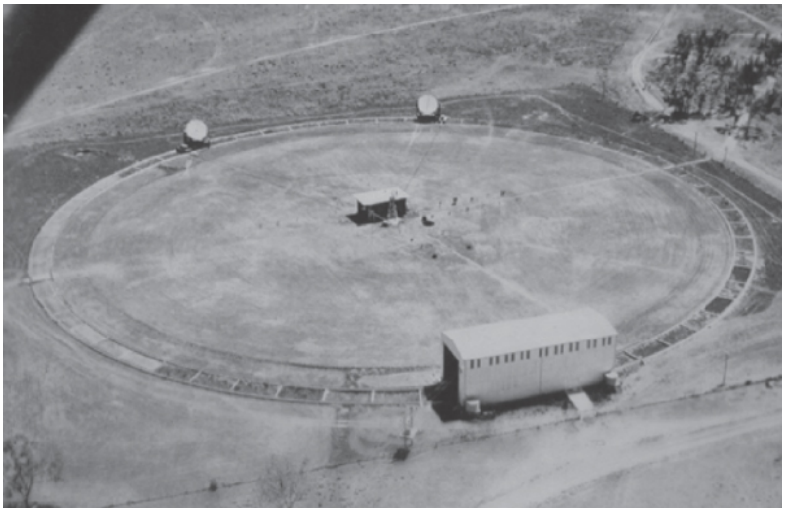

Figure 1.3.: The intensity interferometer near Narrabri (Australia). The two telescopes could be moved on the circular tracks to vary the baseline and to change the angle of sight. Taken from [11]

correlator without optical challenges. This allows in principle kilometer-baselines or even more.
Since electronics in the 1970s have not been as good as today intensity interferometry faced immense technical challenges in that time, the requirements for electronics will be discussed later in this thesis. For that reason the approach of Hanbury Brown and Twiss was not pursued, however, nowadays stellar intensity interferometry has a huge potential. Especially since there are built and planned big telescope arrays which can be used for intensity interferometry as well with a very small effort.

1.2. Physics of intensity interferometry

1.2.1. Coherence

Coherence is one of the most important terms when talking about optical systems. Interference patterns are only visible if the light has a sufficient degree of coherence and since intensity interferometry is strongly related to interference patterns as it will be shown in section 1.2.3 it plays a key role in the whole topic of interferometry. Coherence describes the "stability of light" [12] when propagating in space or time. Attitudes (amplitude, phase) of light that has a high degree of coherence are correlated at different positions (spatial coherence) or time points (temporal coherence). To quantify coherence one defines the **coherence time** τ_c and the

coherence length l_c. Within a coherence time or length light is said to be coherent, meaning that the light's attitudes at a certain position or time can be deduced with a high certainty from a known position or time. [12]
In ideal interference experiments the used light is monochromatic. Interference patterns are built of summing up amplitudes of light. Only if one observes light of the same wavelength or at least of a very narrow interval the phases and therefore summarized amplitudes show clear relations at different points. With increasing optical bandwidth interference effects become less visible. Coherence is therefore indirect proportional to the optical bandwidth. One may therefore define the coherence time as

$$\tau_c = \frac{1}{\Delta\nu} \tag{1.5}$$

where $\Delta\nu$ is the frequency bandwidth of the light. Via $c = \lambda\nu$ with the speed of light c the coherence time is supposed to be expressed by the wavelength bandwidth $\Delta\lambda$.

There is no precise relation between $\Delta\lambda$ and $\Delta\nu$ that holds for every center wavelength λ_0, however, for small bandwidths where the hyperbolic curve can be assumed to be linear one can approximate

$$\Delta\nu = \left.\frac{d\nu}{d\lambda}\right|_{\lambda_0} \cdot \Delta\lambda = (-)\frac{c}{\lambda_0^2}\Delta\lambda \tag{1.6}$$

where λ_0 is the central wavelength and the minus sign can be omitted since $\Delta\nu$ or $\Delta\lambda$ have no direction. This leads to an expression of the coherence time in dependence of wavelength bandwidth

$$\tau_c = \frac{\lambda_0^2}{c\Delta\lambda} \tag{1.7}$$

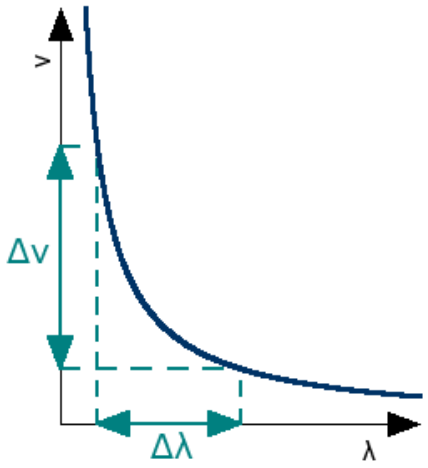

Figure 1.4.: Relation between $\Delta\lambda$ and $\Delta\nu$

The broader the optical bandwidth the shorter the coherence time and the weaker coherence effects. There is the need of optical filtering when observing signals coming from coherence.
The terms "coherence" and "correlation" are strongly related to each other, thus the coherence time can also be called correlation time.

1.2.2. The $g^{(1)}$ and $g^{(2)}$ correlation functions

The normalized n-th order correlation functions $g^{(n)}$ quantify correlations at any positions and times (better: time differences) and are a tool to describe coherence effects. The first and second order correlation functions $g^{(1)}$ and $g^{(2)}$ are of special interest, latter one will be the observed quantity in intensity interferometry. The general form of the first-order correlation function is [13]

$$g^{(1)}(P_1, P_2, \tau) = \frac{\langle E^*(P_1, t)E(P_2, t+\tau)\rangle}{\langle E^*(P_1, t)E(P_1, t)\rangle} \tag{1.8}$$

where P_1 and P_2 are two positions in space and τ is a time difference. The brackets $\langle\rangle$ denote averaging over time, $\langle E(t)\rangle = \frac{1}{T}\int_0^T E(t)dt$ for large T compared to τ. The first order correlation function compares the electromagnetic field amplitude at a point P_1 with the amplitude at point P_2 at a time difference τ. Time-averaging is the reason why the time t is not a parameter of the $g^{(1)}$ function. The denominator is a normalization term[1], in equation 1.8 position P_1 is used for normalization, however, since the parameter do not require a preferred position also P_2 could be used. Since $E^* \cdot E = I$ the normalization is a time-averaging over the intensity at P_1 or P_2, in general one can assume that the average intensities hardly differ, imagine a star observed at different positions on earth, therefore the choice of P_1 or P_2 does not matter.
As already discussed intensity interferometers do not measure amplitudes at all but only intensities, for that purpose the second-order correlation function can be considered: [13]

$$g^{(2)}(P_1, P_2, \tau) = \frac{\langle E^*(P_1, t)E^*(P_2, t+\tau) \cdot E(P_1, t)E(P_2, t+\tau)\rangle}{\langle E^*(P_1, t)E(P_1, t)\rangle \cdot \langle E^*(P_2, t)E(P_2, t)\rangle} \tag{1.9}$$

This equation can be simplified in terms of intensities again by using $I = E^*E$

$$g^{(2)}(P_1, P_2, \tau) = \frac{\langle I(P_1, t) \cdot I(P_2, t+\tau)\rangle}{\langle I(P_1, t)\rangle \cdot \langle I(P_2, t+\tau)\rangle} \tag{1.10}$$

This quantity can be measured with photo-detectors at positions P_1 and P_2 simply by measuring the intensities at these positions. The correlation (multiplication of the intensities) can be done either electronically (a time delay corresponding to τ in one channel can be used for $\tau \neq 0$) or digitally when the intensities of both channels are recorded over time. A more detailed look at the measuring possibilities of the $g^{(2)}$ function is given in section 1.3.1.
Correlations can be observed separately in space and time. Choosing $\tau = 0$ the spatial correlation can be considered, if the two detection points are the same

[1] In literature there is also the unnormalized $G^{(1)}$ function, where the denominator is omitted [14], same holds for higher-order correlations

$P_1 = P_2$ an observation of the temporal $g^{(2)}$ function is possible. Both cases will be further discussed in the theory section since each of them has certain consequences on measurement and concept.
The $g^{(2)}$ function can be interpreted as quantification of the intensity **fluctuations**. In the following I_j will be used for $I(P_j, t+\tau)$ where τ is not further specified. Using $I(t) = \langle I(t)\rangle + \Delta I(t)$ to observe fluctuations around the average intensity the numerator of equation **1.10** can be written as

$$\langle [\langle I_1\rangle + \Delta I_1] \cdot [\langle I_2\rangle + \Delta I_2]\rangle = \langle \langle I_1\rangle \langle I_2\rangle + \langle I_1\rangle \Delta I_2 + \Delta I_1 \langle I_2\rangle + \Delta I_1 \Delta I_2\rangle \quad (1.11)$$

Since $\langle a+b\rangle = \langle a\rangle + \langle b\rangle$ and $\langle const \cdot a\rangle = const \cdot \langle a\rangle$ four terms appear. Two of them vanish since fluctuations over time become zero:

$$\underbrace{\langle \langle I_1\rangle \langle I_2\rangle\rangle}_{\langle I_1\rangle\langle I_2\rangle} + \langle I_1\rangle \cdot \underbrace{\langle \Delta I_2\rangle}_{0} + \langle I_2\rangle \cdot \underbrace{\langle \Delta I_1\rangle}_{0} + \langle \Delta I_1 \Delta I_2\rangle = \langle I_1\rangle \langle I_2\rangle + \langle \Delta I_1 \Delta I_2\rangle \quad (1.12)$$

The $g^{(2)}$ function from equation **1.10** can therefore be written as

$$g^{(2)}(P_1, P_2, \tau) = \frac{\langle I_1\rangle \langle I_2\rangle + \langle \Delta I_1 \Delta I_2\rangle}{\langle I_1\rangle \langle I_2\rangle} = 1 + \frac{\langle \Delta I_1 \Delta I_2\rangle}{\langle I_1\rangle \langle I_2\rangle} \quad (1.13)$$

The $g^{(2)}$ function is different from 1 if the *time-averaged product of intensity fluctuations* at P_1 and P_2 is different from zero. Three cases can be discussed.

- $\langle \Delta I_1 \Delta I_2\rangle = 0$: the intensity fluctuations are totally random, the product averages out, no correlation signal is measured, $g^{(2)} = 1$, which holds for coherent light [15].
- $\langle \Delta I_1 \Delta I_2\rangle > 0$: the intensity fluctuations do not average out, if one of the detectors measures a fluctuation in many cases the other detector measures a fluctuation of the **same sign**. In other words, if a photon increase is measured at one detector, there often is also a photon increase measured at the other detector. For $\tau \approx 0$ it means photons appear (nearly) at the same time, they are *bunched*, $g^{(2)} > 1$. This is the case for chaotic light [15] and is subject of investigation in intensity interferometers.
- $\langle \Delta I_1 \Delta I_2\rangle < 0$: intensity fluctuations do not average out in a way, that there is a drop of intensity in one detector when the other one measures an excess (or on single-photon level: one detector does not detect a photon when the other one does). For $\tau = 0$ it means photons appear not at the same time, they are *anti-bunched*, $g^{(2)} < 1$. This can e.g. be modeled by considering a single

light emitter like one atom. When it emits a photon it needs time to reexcite to emit another photon. Anti-bunching is a signature only explainable by quantum effects [15].

Siegert relation

The Siegert relation links the first and second-order correlation functions in the case of thermal light. Assuming the thermal light source to consist of a huge number of equivalent atoms emitting electromagnetic waves that interfere at the observer the $g^{(2)}$ function can be expressed by $g^{(1)}$ [13]:

$$g^{(2)}(P_1, P_2, \tau) = 1 + |g^{(1)}(P_1, P_2, \tau)|^2 \tag{1.14}$$

This resembles the insensitivity of intensity interferometers to phases as $|e^{i\omega t}| = 1$. Since the first-order correlation function can be deduced easily from the shape of the source as it will be shown in section 1.2.3 the second-order correlation can be as well for thermal light which allows the determination of the shape of the light source by measuring the $g^{(2)}$ function.

A simple approach for spatial correlations: Two-emitter model

To get an impression of the general principle of the (spatial) variation of the $g^{(2)}$ function assume the following model. Two points a and b emit electromagnetic waves propagating towards an observation plane in a distance L. In the observation plane two photo-detectors 0 and 1 measure intensities at their positions. The detectors are separated by the distance d which can be varied by moving one of the detectors. In the following, the spatial $g^{(2)}$ function is calculated. The following calculations are strongly oriented to a published document by Gordon Baym [16] which is already an extension of a calculation in his book [17].
a and b emit spherical electromagnetic waves of the form $E_a(r) = \frac{\alpha}{r} e^{ikr + i\Phi_a}$ and $E_b(r) = \frac{\beta}{r} e^{ikr + i\Phi_b}$ with amplitudes α and β and same wave number $k = \frac{2\pi}{\lambda}$ reflecting a monochromatic emission. The amplitude at detector $j \in 1, 2$ due to superposition of the waves is

$$E_j = \frac{1}{L} \left(\alpha e^{ikr_{aj} + i\Phi_a} + \beta e^{ikr_{bj} + i\Phi_b} \right) \tag{1.15}$$

when $L \gg R, d$ representing a system where the distance of observer and source is large, like for a star observed on earth. The intensity I_j at position j turns out to be

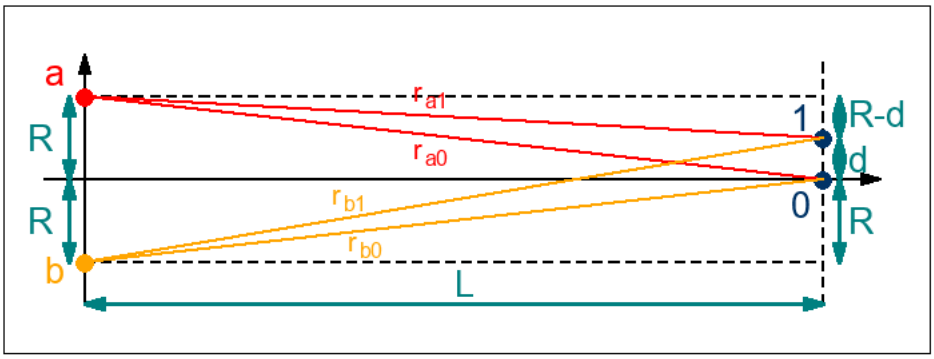

Figure 1.5.: A simple model with two emitters a and b and two detectors 0 and 1 to see the principle of varying intensity correlations

$$I_j = E_j^* E_j = \frac{1}{L^2}\left[\underbrace{|\alpha|^2}_{A_j} + \underbrace{|\beta|^2}_{B_j} + \underbrace{\alpha^*\beta e^{ik(r_{bj}-r_{aj})+i(\Phi_b-\Phi_a)}}_{C_j} + \underbrace{\beta^*\alpha e^{ik(r_{aj}-r_{bj})+i(\Phi_a-\Phi_b)}}_{D_j}\right] \tag{1.16}$$

When the formula for the intensities is known $g^{(2)} = \frac{\langle I_0 I_1\rangle}{\langle I_0\rangle\langle I_1\rangle}$ can be computed. The denominator is easy to calculate since the C_j and D_j terms average to zero as one averages the intensities over time and thus over the phases $\Phi_{a,b}$.

$$\langle I_0\rangle = \langle I_1\rangle = \frac{1}{L^2}\left[|\alpha|^2 + |\beta|^2\right] \tag{1.17}$$

For the numerator one has to multiply I_0 with I_1 before time-averaging. Multiplication according to equation 1.16 gives 16 terms (all combinations of the A_j, B_j, C_j and D_j), however, many of them vanish when averaging over time:

- Terms with exactly one C or D (and therefore exactly one A or B) vanish due to phase-averaging over time.
- Even terms with only C or D, namely $\langle C_0 C_1\rangle$ and $\langle D_0 D_1\rangle$ vanish for the same reason: The phase remains in the terms:

$$C_0 C_1 = (\alpha^*\beta)^2 \cdot e^{ik(r_{b0}-r_{a0}+r_{b1}-r_{a1})+2i(\Phi_b-\Phi a)} \tag{1.18}$$

Other terms remain:

- Terms with only A and B survive averaging as they contain no phase.

- Terms with one C and one D, namely $\langle C_0 D_1 \rangle$ and $\langle C_1 D_0 \rangle$ survive as the phases cancel out

$$C_0 D_1 = |\alpha|^2 |\beta|^2 \cdot e^{ik(r_{b0} - r_{a0} + r_{a1} - r_{b1}) + i\overbrace{(\Phi_b - \Phi_a + \Phi_a - \Phi_b)}^{=0}} \tag{1.19}$$

Introducing $l := r_{b0} - r_{a0} + r_{a1} - r_{b1}$ the total expression for the numerator of the $g^{(2)}$ function is

$$\langle I_0 I_1 \rangle = \frac{1}{L^4} \left(|\alpha|^4 + |\beta|^4 + 2 \cdot |\alpha|^2 |\beta|^2 \cdot [1 + \cos(kl)] \right) \tag{1.20}$$

With

$$\langle I_0 \rangle \langle I_1 \rangle = \frac{1}{L^4} \left(|\alpha|^4 + |\beta|^4 + 2|\alpha|^2 |\beta|^2 \right) \tag{1.21}$$

the entire $g^{(2)}$ function becomes

$$g^{(2)} = \frac{\langle I_0 I_1 \rangle}{\langle I_0 \rangle \langle I_1 \rangle} = 1 + \frac{2|\alpha|^2 |\beta|^2}{\left(|\alpha|^2 + |\beta|^2 \right)^2} \cdot \cos(kl) \tag{1.22}$$

Hence there is an oscillating part of the $g^{(2)}$ function depending on l. In the sketch of figure 1.5, where $r_{a0} = r_{b0}$ the simple expression for l is

$$l = r_{a1} - r_{b1} \tag{1.23}$$

The oscillation of the $g^{(2)}$ function is therefore a function of the difference between the distances from the emission points a and b to detector 1. When varying the distance d by moving detector1 in the observation plane the value of the measured $g^{(2)}$ function changes.
Furthermore also the separation of a and b and thus the size of the source $2R$ affects l. If the two points were put together $l = r_{a1} - r_{b1} = 0$ and no oscillation of the $g^{(2)}$ function could be measured but $g^{(2)} = const > 1$ for all possible distances. Intensities of a point source are correlated everywhere in the observation plane. However, the larger the two points are separated the more significant the distance differences get and the shorter the oscillation of the $g^{(2)}$ function becomes. The spatial $g^{(2)}$ pattern in the observation plane is therefore a tool to draw conclusions on the source geometry. A general mathematical formulation of this issue not using single emission points but an arbitrary emission area is described in the van Cittert-Zernike theorem.

1.2.3. Temporal and spatial correlations

Spatial correlations: the van Cittert-Zernike theorem

Imagine a planar emission source of incoherent monochromatic light[2]. The van Cittert-Zernike theorem describes a relation between the source geometry and the spatial first-order correlation function. In the far field of the source the theorem is the following [18]:

$$g^{(1)}(\vec{r}_1, \vec{r}_2) = e^{ik(r_2 - r_1)} \frac{\int_\sigma I(\vec{r}') e^{-ik(\vec{s}_2 - \vec{s}_1)\vec{r}'} d^2\vec{r}'}{\int_\sigma I(\vec{r}') d^2\vec{r}'} \tag{1.24}$$

The geometry of this equation is seen in figure 1.6. $I(\vec{r}')$ is the intensity of the source described by σ at position $\vec{r}'$, the two detectors P_1 and P_2 are located at $\vec{r}_1 = r_1\vec{s}_1$ and $\vec{r}_2 = r_2\vec{s}_2$.

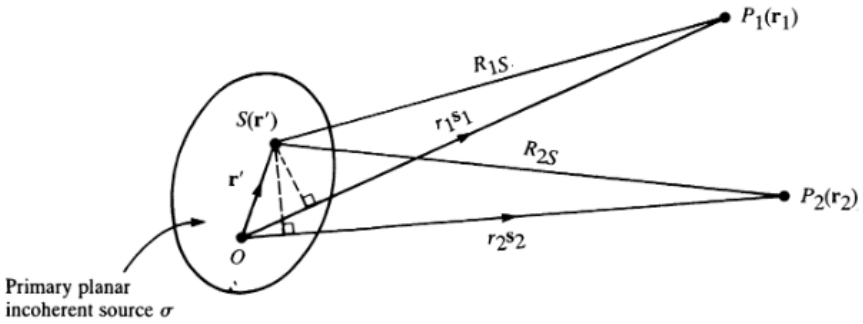

Figure 1.6.: Geometry for the van Cittert-Zernike theorem in the far field. Sketch is taken from [18]

Especially when the distances of the detectors to the origin O is the same ($r_1 = r_2$) the front exponential function vanishes and - except for the normalization in the denominator - the first-order correlation function is exactly the Fourier transform of the intensity distribution of the light source.
However, as it is well known, there is an other goal of calculating the Fourier transformation of an intensity distribution: calculation of the (Fraunhofer) diffraction pattern of an aperture [19]. One can conclude that the *first-order correlation function generated by an incoherent light source* has the same shape as the *diffraction pattern of a coherently illuminated aperture*, including the positions of zeros, maxima and minima.

[2] Stars are actually not planar, light from the margin of the disc is emitted further away from the detector on earth than light from the center, however, important is the bending radius of the electromagnetic waves. Then the difference is negligible here

This has a convenient consequence: It allows the calculation of the $g^{(1)}$ function in the observation plane without using complex mathematical formulations but only simple considerations. Imagine a one-dimensional incoherent light source of the size D. In the observation plane the size of the coherence cell shall be calculated. The borders of the coherence cell are defined as the first minima of the $g^{(1)}$ function. For that one can use the same maths as for calculation of interference minima of a coherently illuminated slit. The geometry is shown in figure 1.7.

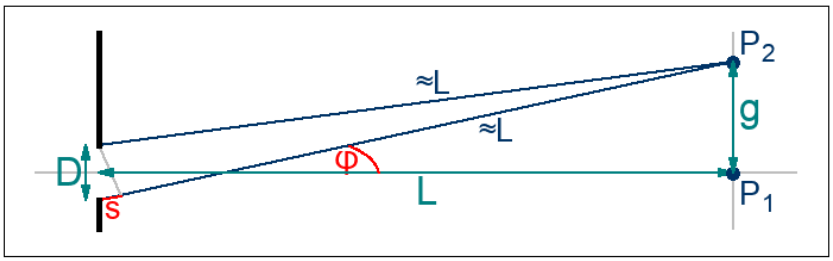

Figure 1.7.: The geometry of calculating diffraction extrema of a (1D)-slit

While the diffraction pattern has its maximum at P_1, the minimum should be at P_2 in a distance g from P_1. The path difference s of the light beams from the borders of the slit s can be calculated via

$$\sin\varphi = \frac{g}{L} = \frac{s}{D} \tag{1.25}$$

The criterion for a minimum at P_2 is that $s = n \cdot \lambda$ where $n \in \mathbb{N}$, and for the first minimum $n = 1$, since here every part of the slit that is producing a positive amplitude at P_2 has its counterpart. The total size $G = 2g$ from minimum to minimum turns out to be

$$G = 2g = 2L \cdot \frac{\lambda}{D} \tag{1.26}$$

According to the van Cittert-Zernike theorem this is equal to the size of the coherence cell (minima of the $g^{(1)}$ function). Taking the Siegert relation into account, the $g^{(2)}$ function can be easily calculated and has actually the same properties.
Equation 1.26 reveals some important attitudes of coherence:

- The larger the wavelength λ that is observed the larger the coherence cell is at a certain distance L. When considering the stellar HBT experiment this

parameter is the only one that can be chosen by using a special wavelength filter[3] since L and D are star-specific on earth.

- The smaller the light source, the bigger the coherence cell. This inverse relation is the most important one for the measurement of (angular) sizes using intensity interferometry. It is the reason for a broad range of coherence cell sizes of different stars starting with a few meters up to kilometers. A multi-usable intensity interferometer should therefore cover possible baselines of different orders of magnitude. On the other hand in the lab where especially L is restricted to be small (a few meters) the source size D has to be kept tiny to create a macroscopic size of the coherence cell. Therefore pinholes with apertures of $< 1\,\mathrm{mm}$ are placed after the source to restrict the transmission size to a small area.

- The larger the distance L of the source from the detection plane the bigger the coherence cell. That means incoherently emitted light becomes more and more spatially coherent when propagating.

Latter connection might seem a bit counter-intuitive. However, there are some suitable point of views on this issue that are helpful for understanding.
Imagine a bridge over a pond and ducks jumping into the water [20]. Their impacts on the water surface creating spherical water waves are totally uncorrelated ("incoherent wave source") analog to the uncorrelated emissions of photons in chaotic light sources. The resulting wave pattern can be seen in figure 1.8.
Consider two detectors measuring the amplitude[4] at any two points 1 and 2 near the ducks. It is very difficult to find wave correlations as the interference pattern is quite chaotic close to the emission points since the different spherical waves have small radii of curvature. However, moving further away to 3 und 4 the pattern becomes less and less chaotic, the spatial coherence increases.
Another perspective is looking at a source in different distances. The further away the source is, the smaller and therefore more point-like it looks. A point source cannot produce a (spatially) chaotic interference pattern since every spherical wave is emitted at the same position. [20]
In one dimension the Fourier transform of a slit happens to be a *sinc* function[5]. According to the Siegert relation the second-order correlation function of chaotic light can be computed.

[3] It has to be ensured that the photodetectors have a sufficient good quantum efficiency at the selected wavelength
[4] Since still the $g^{(1)}$ function is observed, amplitudes are considered and not intensities
[5] Although this fact is well known it will be shown below when calculating the temporal $g^{(2)}$ function out of a frequency spectrum

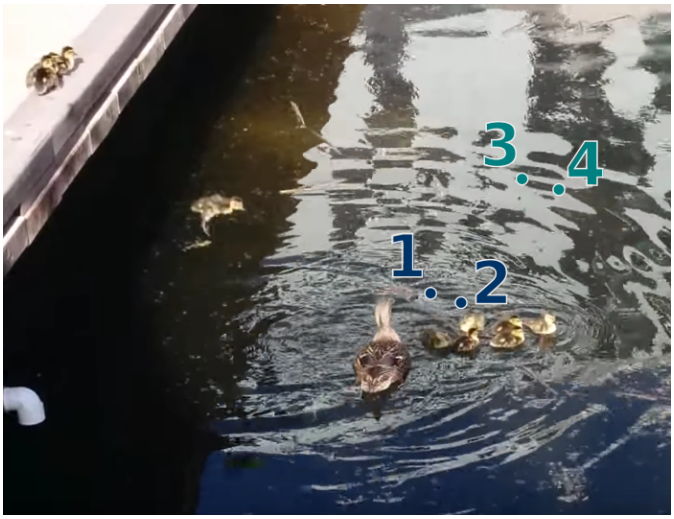

Figure 1.8.: Water waves created by ducks become spatially coherent at large distances. Image is a screenshot from [21]

$$g^{(2)}(d) = 1 + |g^{(1)}(d)|^2 = 1 + \mathrm{sinc}^2(d) \tag{1.27}$$

When the detectors are close together the correlation is maximal. The $g^{(2)}$ function has a value of 2 meaning that correlated intensity fluctuations are of the same strength as the intensities theirselves (see equation **1.13**). When the detectors are separated the correlation decreases until one enters the border at the coherence cell where no correlation is measured at all. Going even further away one could in principle find other correlation maxima, however, these are already that small that they effectively cannot be measured any more.
Since the theoretical formula is completely known there is no need to fully reach the size of a coherence cell with telescopes, instead a few distances can be adjusted and a fit into the results yield the $g^{(2)}$ function.
Note that these mathematical considerations have dealt with one-dimensional sources. For a two-dimensional rectangular aperture the same condition for minima and maxima holds, however, considering a circular aperture with diameter D the $g^{(2)}$ function can be described by the two-dimensional Bessel function of the first kind [22].

$$g^{(2)}_{\mathrm{circ}}(d) = 1 + \left| 2\frac{J_1(\pi D \nu_d)}{\pi D \nu_d} \right|^2 \tag{1.28}$$

where $\nu_d = \frac{d}{\lambda L}$. There is an additional factor 1.22 when calculating the first zero of the $g^{(1)}$ function or the first minimum of $g^{(2)}$ respectively. [23]

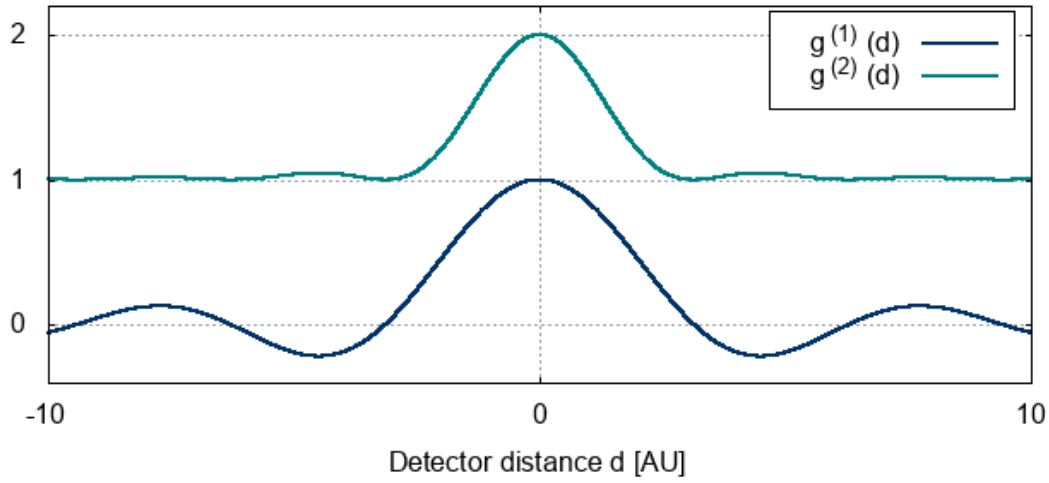

Figure 1.9.: Spatial $g^{(1)}$ an $g^{(2)}$ functions produced by a slit-like source.

$$G_{\text{circ}} = 1.22 \cdot \frac{2L\lambda}{D} \tag{1.29}$$

Temporal correlations: the Wiener-Khinchin theorem

The Wiener-Khinchin theorem relates the temporal first-order correlation function $g^{(1)}(\tau)$ with the normalized power spectrum $F(\omega)$ of the light source, namely [13]

$$F(\omega) = \frac{1}{2\pi} \int_{-\infty}^{\infty} g^{(1)}(\tau) e^{i\omega\tau} d\tau \tag{1.30}$$

Again, Fourier transforms come into play. The back transformation can be used as well to calculate the temporal $g^{(1)}$ function out of the power spectrum.

$$g^{(1)}(\tau) = \int_{-\infty}^{\infty} F(\omega) e^{-i\omega\tau} d\omega \tag{1.31}$$

As an example imagine an optical filter only passing frequencies in a range $[\omega_0 - \frac{\Delta\omega}{2} : \omega_0 + \frac{\Delta\omega}{2}]$ around the central frequency ω_0 with a bandwidth $\Delta\omega$. The filter is assumed to be rectangular in the frequency regime with normalized amplitude $\frac{1}{\Delta\omega}$ so that $\int F(\omega) d\omega = 1$. Let's denote $\omega_a = \omega_0 - \frac{\Delta\omega}{2}$ and $\omega_b = \omega_0 + \frac{\Delta\omega}{2}$. The temporal $g^{(1)}$ function can be calculated according to equation 1.31

$$g^{(1)}(\tau) = \int_{-\infty}^{\infty} F(\omega) e^{-i\omega\tau} d\omega = \frac{1}{\Delta\omega} \int_{\omega_1}^{\omega_2} e^{-i\omega\tau} d\omega \tag{1.32}$$

Integration gives

$$g^{(1)}(\tau) = \frac{-1}{\Delta\omega i\tau}\left[e^{-i\tau\omega_b} - e^{-i\tau\omega_a}\right] = \frac{-1}{\Delta\omega i\tau}e^{-i\tau\omega_0}\left[e^{-i\tau(\omega_b-\omega_0)} - e^{-i\tau(\omega_1-\omega_0)}\right] \quad (1.33)$$

Since ω_0 is the mean between ω_a and ω_b one can introduce $\tilde{\omega} = \omega_b - \omega_0$ so that $\omega_a - \omega_0 = -\tilde{\omega}$. Equation 1.33 becomes

$$g^{(1)}(\tau) = \frac{-2e^{-i\tau\omega_0}}{\Delta\omega\tau}\frac{1}{2i}\left[e^{i(-\tau\tilde{\omega})} - e^{-i(-\tau\tilde{\omega})}\right] = \frac{-2e^{-i\tau\omega_0}}{\Delta\omega\tau}\sin(-\tau\tilde{\omega}) \quad (1.34)$$

Since the sinus is point-symmetrical and $\tilde{\omega} = \frac{1}{2}\Delta\omega$ one gets

$$g^{(1)}(\tau) = \frac{e^{-i\tau\omega_0}}{\tau\Delta\omega/2}\sin\left(\frac{\tau\Delta\omega}{2}\right) = e^{-i\tau\omega_0}\mathrm{sinc}\left(\frac{\tau\Delta\omega}{2}\right) \quad (1.35)$$

Using the Siegert relation the $g^{(2)}$ function is

$$g^{(2)}(\tau) = 1 + \mathrm{sinc}^2\left(\frac{\tau\Delta\omega}{2}\right) \quad (1.36)$$

So for a rectangular frequency spectrum one obtains the same behavior of the $g^{(2)}$ function in the temporal than in the spatial regime. For small τ the $g^{(2)}$ function is > 1, bunched photons can be measured, for large τ the $g^{(2)}$ function becomes 1. To get an impression of the falling time of the $g^{(2)}$ function one can calculate the first zero of the *sinc* function which refers to

$$\frac{\tau_1\Delta\omega}{2} = \pi \Rightarrow \tau_1 = \frac{2\pi}{\Delta\omega} \quad (1.37)$$

In the wavelength regime one can say $\Delta\lambda = \lambda_a - \lambda_b$. Using $\lambda = \frac{2\pi c}{\omega}$ it can be written as

$$\Delta\lambda = \frac{2\pi c}{\omega_a} - \frac{2\pi c}{\omega_b} = \frac{2\pi c(\omega_b - \omega_a)}{\omega_a\omega_b} \approx \frac{2\pi c\Delta\omega}{\omega_0^2} \quad (1.38)$$

for small $\Delta\omega$ compared to the center frequency ω_0. Solved for $\Delta\omega$

$$\Delta\omega = \frac{\Delta\lambda\omega_0^2}{2\pi c} = \frac{\Delta\lambda 2\pi c}{\lambda_0^2} \quad (1.39)$$

Applied to equation 1.37 the first zero is

$$\tau_1 = \frac{\lambda_0^2}{\Delta\lambda c} \quad (1.40)$$

An important relation is $\tau_1 \propto \frac{1}{\Delta\lambda}$, meaning the smaller the optical bandwidth the stronger is the correlation signal. This matches with the consideration of a decreasing coherence for a broader wavelength spectrum. The formula in equation **1.40** is coincides with the definition of the coherence time in section 1.2.1. This shows that the concept of the coherence time is a useful tool of quantifying a system by its optical wavelength center and bandwidth.
Let's assume having a $\Delta\lambda = 1\,\text{nm}$ optical filter at $\lambda_0 = 532\,\text{nm}$ (a similar composition will be used in the lab), the first zero is at

$$\tau_1 = \frac{(532\,\text{nm})^2}{1\,\text{nm} \cdot c} = 0.9\,\text{ps} \tag{1.41}$$

That means that the bunching signal drops **within a picosecond** even for a quite narrow optical bandwidth filtering. This is a time range impossible to resolve with man-made photo-detectors and electronics respectively. Using a 1 nm optical filter will therefore not resolve the shape of the correlation function but only lead to an enhancement of the $g^{(2)}$ function at $\tau \approx 0$. Furthermore the value of $g^{(2)}(\tau = 0)$ drops from 2 to a number only slightly differing from 1. This is the greatest challenge of doing intensity interferometry. While being quite insensitive to atmospheric fluctuations one has to ensure a pretty good time resolution to measure a reasonable signal in a reasonable time. A quantitative view on this issue is taken in section 2.3.
For impact-broadened light sources with a Lorentzian shape of the power spectrum centered around ω_0 the corresponding first-order correlation function turns out to be [12]

$$g^{(1)}(\tau) = e^{-i\omega_0\tau - \frac{|\tau|}{\tau_c}} \tag{1.42}$$

where $\tau_c = \frac{1}{\Delta\omega}$ and hence according to the Siegert relation

$$g^{(2)}(\tau) = 1 + e^{-\frac{2|\tau|}{\tau_c}} \tag{1.43}$$

Another important case is Doppler-broadened light with a Gaussian power spectrum profile or light that passes a Gaussian-shaped optical filter. Since such a Gaussian optical filter will be used in section 4.3, it is worth it to take a special look at the quantitative behavior. Imagine a Power spectrum of the form

$$F(\omega) = \frac{1}{\Delta\omega} \exp\left[-\pi \frac{(\omega - \omega_0)^2}{\Delta\omega^2}\right] \tag{1.44}$$

with an angular frequency width $\Delta\omega$. The Wiener-Khintchine theorem reveals the first-order correlation function

$$g^{(1)}(\tau) = e^{-\pi(\Delta\nu\tau)^2 - i\omega_0\tau} \tag{1.45}$$

and therefore the second-order correlation function

$$g^{(2)}(\tau) = 1 + e^{-2\pi(\Delta\nu)^2} \tag{1.46}$$

where $\Delta\nu = \frac{\Delta\omega}{2\pi}$. Yet no statement about the exact definition of $\Delta\omega$ was done, however, it can be related to the sigma-width and the FWHM considering equation 1.44:

$$\frac{\pi}{\Delta\omega^2} = \frac{1}{2\sigma_\omega^2} \Rightarrow \Delta\omega = \sqrt{2\pi} \cdot \sigma_\omega \tag{1.47}$$

and using $\Delta_{\mathrm{FWHM}} = 2\sqrt{2\ln 2} \cdot \sigma$ the relation is

$$\Delta = \underbrace{\frac{1}{2}\sqrt{\frac{\pi}{\ln 2}}}_{\approx 1.06} \cdot \Delta_{\mathrm{FWHM}} \tag{1.48}$$

which holds for ω, ν and λ.

1.3. Realizations of intensity interferometry

1.3.1. Correlation methods

Doing intensity interferometry is all about evaluating the $g^{(2)}$ function.

$$g^{(2)}(P_1, P_2, \tau) = \frac{\langle I(P_1, t) I(P_2, t+\tau)\rangle}{\langle I(P_1, t)\rangle \langle I(P_2, t)\rangle} \tag{1.49}$$

This requires measuring the intensities at the positions P_1 and P_2 and correlating the channels either for the same time ($\tau = 0$) or with a relative delay between the channels. The correlation can be done "live" during the measurement using electronic correlators, if a time delay is required one signal has to be shifted i.e. by a cable delay to produce the requested τ. Another option is to save the measurement data, that is the photo-current or the arrival times of photons, respectively and doing digital correlations afterwards. This may need some computation time but it enables investigating the system in more detail. Since the data are stored, various computations can be done to analyze results. As this may be indispensable when the results do not match to expectations this is the method that will be used for experiments described in this thesis. Furthermore in this way measurements at two (or more) points can be taken without any optical or electronic connection between the detectors. The only condition is that the two measurements are synchronized in time, but each channel can be measured separately.

The way how intensities are recorded is another issue. There are actually two possibilities to do it, either measuring the photo-current produced by photo-detectors or detecting arrival times of photons.

Photo current measuring

Photo-detectors like PMTs produce a photo current. Each detected photon leads to a signal pulse.

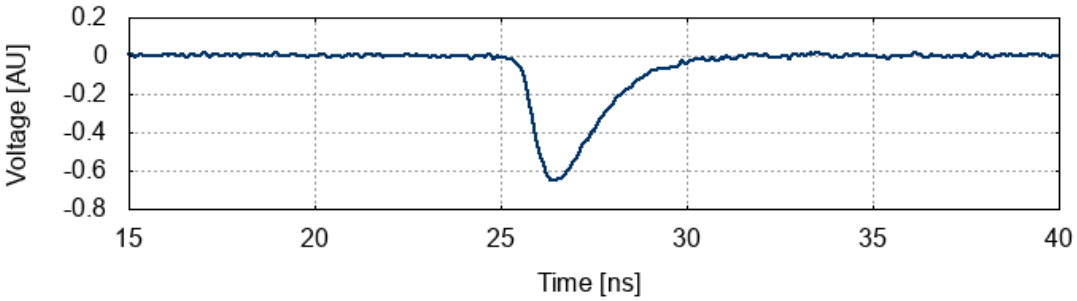

Figure 1.10.: Signal pulse produced by a PMT detecting a photon.

Photon pulses are in general negative here, the baseline is at 0. Another photon will produce the same signal with maybe slightly different amplitude. If multiple photons appear in a close time the signal pulses add up, the current intensity is then proportional to the signal height and intensity multiplication can be done. This method is quite simple and allows for measuring photon rates in the GHz regime without problems. Hanbury Brown and Twiss already used photo current correlations at the Narrabri Stellar Interferometer [2][24].
However, continuously sampling the photo current over a long time is difficult and typical electronics fail to sample on a sub-nanosecond scale. In contrast, as already seen, a good time resolution is essential for gaining a high correlation signal.

Photon time stamping

Photon time stamping is the method used for lab experiments in this thesis. Trigger thresholds are used to determine the arrival time of a photon instead of sampling the signal.
A threshold for the leading edge can be set to any level. When the signal from a photo-detector reaches the threshold an event is recorded, the corresponding time is the specific time tag of a photon. Correlating the signals does not mean multiplying intensities any more but comparing photon arrival time differences. Since the $g^{(2)}$ function is enhanced at $\tau = 0$ photons tend to arrive simultaneously at the two

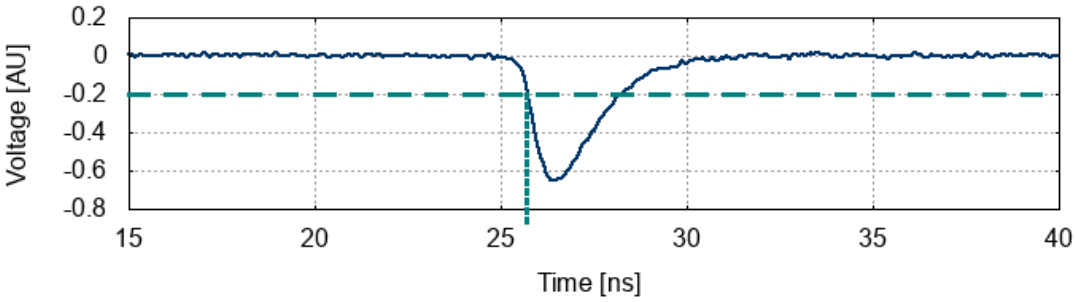

Figure 1.11.: When the signal exceeds a voltage threshold an event at time t is recorded.

detectors and photon combinations with $\tau \approx 0$ should exist more often than those with $|\tau| > 0$. By "only" recording time stamps of photons a more frequent time sampling/binning is possible than by sampling the PMT signal, electronics provide digitization cards time binning of $\Delta t_{\text{bin}} = 250\,\text{ps}$, of course time resolution of PMTs and electronics influence the total time resolution.

However, there are some disadvantages as well. When a second photon arrives shortly after a first when the PMT signal has not recovered to the baseline yet the second photon cannot be detected. Hence, for each channel there is a certain *dead time* after each detected photon. It lasts about 2 ns (in this case) until the signal intersected the threshold again. Photon bunching effects on picosecond scales are impossible to detect with only one detector in photon counting mode.

The photon rate cannot be increased over some MHz which makes time stamping mode useless in systems where very high rates are necessary to detect a signal.

The method that suites better to the specific situation depends therefore on many factors and should be considered well.

1.3.2. Stellar intensity interferometry

When doing intensity interferometry with stars one faces the problems of getting a high photon rate to keep the measurement time reasonable short (in more detail this can be seen in section 2.3). Therefore one uses telescopes with a collection area that is orders of magnitude above the size of the photo-cathode of common PMTs. The light has to be focused into a small area where the PMT can be put. Depending on the telescope and system suitable optics for filtering a narrow optical bandwidth is necessary to implement.

Movable telescopes

The $g^{(2)}$ function has to be evaluated at different telescope distances. When taking two telescopes and measuring, it is necessary to move at least one of the telescopes to increase or decrease the distance between them. That is no problem concerning small mobile telescopes like simple Fresnel lens barrels. However, larger telescopes are in general installed to the ground making shifts impossible. The Narrabri Stellar Intensity Interferometer where telescopes were movable on a circular track with a maximum distance of $d = 188\,\mathrm{m}$ [2] is a rare construction of such a telescope system.

Implementation in large telescope arrays

A way out of this dilemma are large telescope arrays consisting of many telescopes with different baselines. Such arrays are recently built and planned for different purposes. One of the mightiest ones may be the Cherenkov Telescope Array (CTA) which is currently built. Especially the CTA south array being built in the Atacama desert in Chile will consist of many telescopes of different sizes.

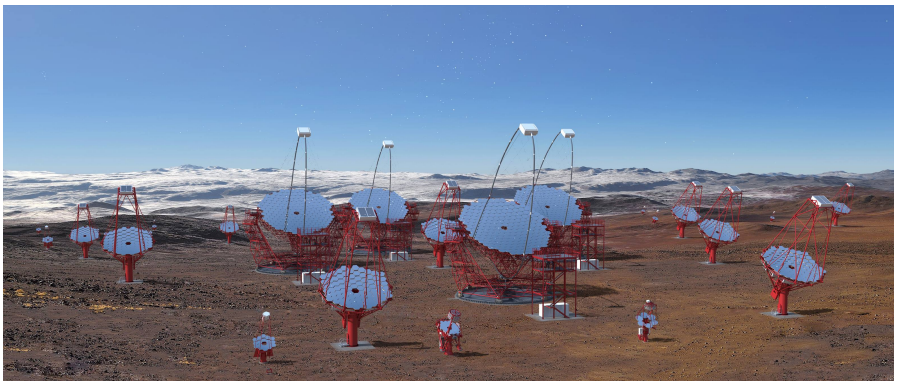

Figure 1.12.: Illustration of the CTA southern hemisphere array in the Atacama desert in Chile. Picture taken from [25]

CTA is actually constructed for investigating the gamma ray sky via detecting Cherenkov light produced by secondary particles of a gammay ray impact in the atmosphere [26]. That differs drastically from the idea of intensity interferometry, however, the telescopes that are being built can be used for it. The only necessary implementation is a detection unit in the telescope's camera plane where i.e. optical filters are installed before a photo detector. Stellar intensity interferometry could then be done during times when CTA or other telescope arrays are not in service i.e. in nights with a bright moon.

The telescopes in these arrays cannot be moved for measuring at different baselines, however, since it is an array of many telescopes there are many different baselines as well. Figure 1.13 shows a possible realization of the CTA southern hemisphere array, where 99 telescopes are spread over a 2 km · 2 km area.

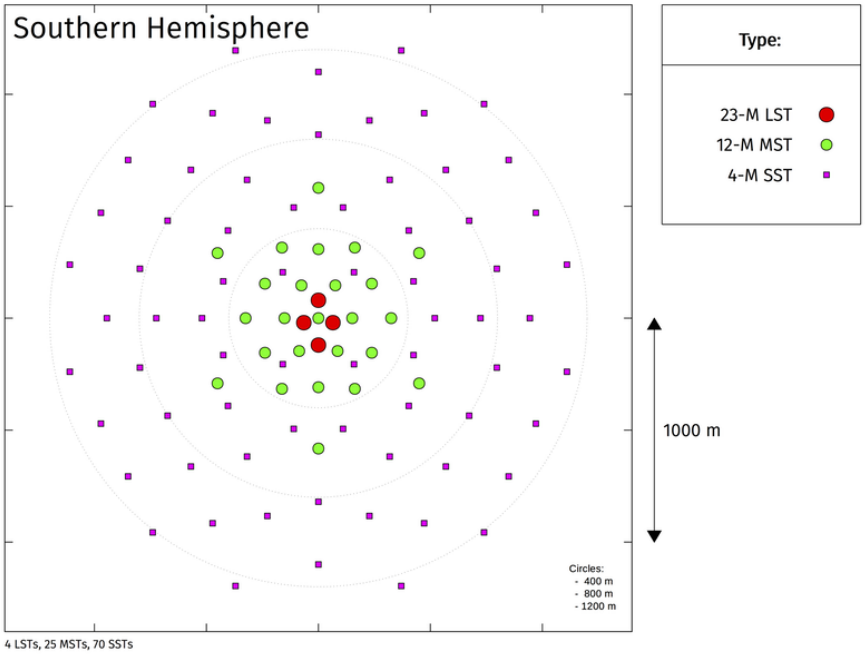

Figure 1.13.: A proposed arrangement of the CTA south array. Picture taken from [25]

The possible angular resolution can be estimated. Imagine two telescopes at a distance of $d = 2\,\mathrm{km}$ observing a star. The first zero in the correlation function is at $x_1 = 1.22 \cdot \frac{\lambda L}{D}$ with L the distance of the star from earth and D its diameter. This enables resolving the $g^{(2)}$ function up to the first minimum of stars with an angular diameter of

$$\varphi \approx \sin\varphi = \frac{D}{L} = 1.22 \cdot \frac{\lambda}{d} = 1.22 \cdot \frac{550\,\mathrm{nm}}{2\,\mathrm{km}} = 3.36 \cdot 10^{-10} \mathrel{\widehat{=}} 0.069\,\mathrm{mas} \qquad (1.50)$$

observing at $\lambda = 550\,\mathrm{nm}$. And - since there will be no need to measure the decrease of the $g^{(2)}$ function up to the first minimum - even smaller stars will be observable. Furthermore all baselines can be measured simultaneously, this reduces the total measurement time drastically compared to measuring at a distance and moving further afterwards.
All these factors make intensity interferometry to a very promising tool of measuring stellar angular diameters with such arrays in the future.

2.Detection process and analysis

Detecting (single) photon signals is an indispensable tool for photon counting intensity interferometry. Therefore PMTs with a quantum efficiency of up to 50% are used, their operation principle as well as the processing of the output signal until the photon time tag is saved on the computer will be explained in this section. Furthermore the analysis of the time tags is described. It will be shown how to calculate the $g^{(2)}$ function from the single time stamps.
Finally it is also important to spend some thoughts on expectations from the measurements. As the bunching signals of thermal light sources with a short correlation time compared to the time resolution of the electronics are quite small, long measurement times are needed. The expected measurement times for any requested significance of the correlation signal can be calculated theoretically to test the measurement for usefulness. Since the long-term goal is stellar intensity interferometry it will be necessary to not measure for days or longer to see significant signals, reflections on this problem will be considered in the last section of this chapter.

Contents

Figure 2.1: Symbol for PMTs

2.1. Electronic devices

On the way to quantitative bunching experiments with a mercury lamp and a LED multiple setups were used differing slightly for test measurements, optimizing noise suppression etc., however there are three standard components that are always installed in the photo-detection chain of each channel. Photomultipliers detecting the photons, amplifiers and the digitization card time tagging the signals.

2.1.1. Photomultiplier

Photomultipliers (PMTs) are used to detect photons. Impacting on the photo-cathode photons get absorbed and accelerate electrons which leave the cathode. The electrons are focused by an electrode onto the dynode chain where they are multiplied when hitting a dynode. Finally, the electrons arrive at the collection anode where the output signal is created. [27]
These signal pulses look like in figure 1.11. Since the pulses vary in height and rise time until the threshold is reached especially when multiple photons are detected at once there is a time spread causing a decreasing time resolution of the system.

Figure 2.2.: Different photomultipliers used during the measurements: R5600 (left), H3164-10 (center) and H10770-40 (right)

A quality criterion for PMTs is the quantum efficiency depending on the photo-cathode material. A high quantum efficiency is desired since high photon rates are wanted for the measurement decreasing the measurement time. The PMT providing a quite high quantum efficiency in the visible optical range is the H10770-40 from Hamamatsu in figure 2.2 using a GaAsP photo-cathode, its radiant sensitivity is shown in figure 2.3.
The quantum efficiency η can be deduced from the radiant sensitivity $S(\lambda)$ via [29]

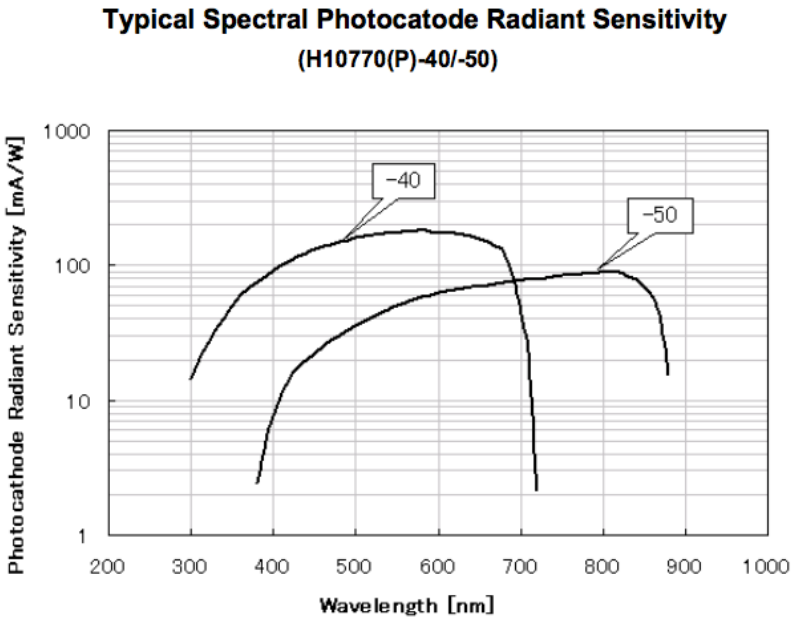

Figure 2.3.: Photo-cathode radiant sensitivity. The -40 is used in quantitative correlation measurements in chapter 4. Taken from [28]

$$\eta(\lambda) = \frac{hc}{\lambda q_e} \cdot S(\lambda) \tag{2.1}$$

At $\lambda = 550\,\text{nm}$ the radiant sensitivity is $176\,\frac{\text{mA}}{\text{W}}$ [28] ending up in a quantum efficiency of

$$\eta(550\,\text{nm}) = 39,7\,\% \tag{2.2}$$

Since the output current is restricted to $2\,\mu\text{A}$ at a gain of 10^6 which is the order of magnitude of the electron multiplication factor [28] the maximum photon rate is restricted to about $\dot{N}_{\text{max}} \approx 12.5\,\text{MHz}$.

2.1.2. Amplifier

The amplifier of the type PAM 102-P from PicoQuant is used to amplify the PMT signals. It is providing a fast rise time of the amplified pulses with a gain of 25 dB over a broad bandwidth of at least 1 GHz [30] which enables achieving a high time resolution of the system.
The amplified signal is brought directly to the digitization card.

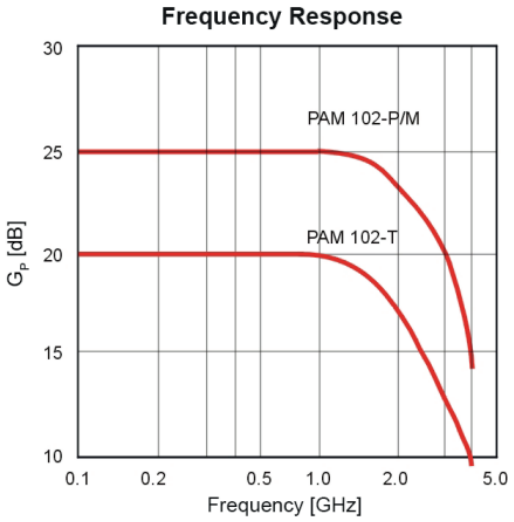

Figure 2.4: Gain characteristics of the PAM 102. The used amplifier is the PAM 102-P. Taken from [30]

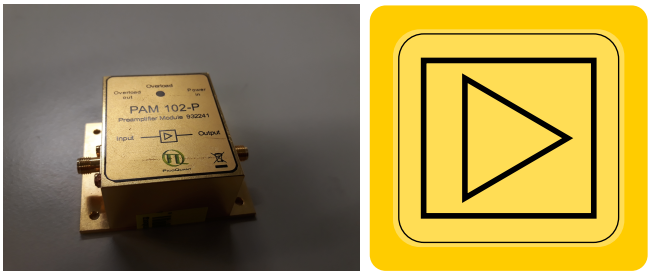

Figure 2.5.: Amplifier PAM 102-P and its symbol used in sketches

2.1.3. Digitization card

The digitization card is the last element in the electronics chain with two input channels. Actually it is developed for start-stop single photon counting measurements where an external synchronization signal is thought to be adapted to the "sync" channel [31], which will always be called channel 0 from now. The other channel, channel 1, is expected to be connected to a photo-detector, however, as the channels can be treated equally PMT electronics can be connected to channel 0 as well. In the corresponding software a voltage threshold can be set. When the input signals exceed the threshold value an event in the corresponding channel is detected. There are different measurement modes. While directly measuring time differences between channel 1 and channel 0 events is possible absolute time tags can be stored as well. Since also time differences of non-neighboring photons are of interest latter mode is used during the experiments and correlation is done by a software developed during this thesis.
The internal time measurement is done by a Time-to-digital-converter (TDC) with a minimum time binwidth of 250 ps while providing a count rate of up to 40 MHz

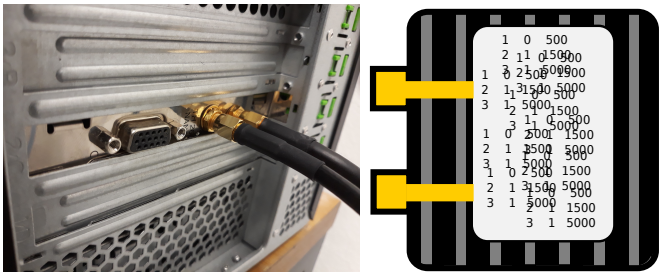

Figure 2.6.: TimeHarp 260N, already implemented in the computer and its illustration symbol in this thesis

per channel [32] which is far above the maximum PMT rate of about 12.5 MHz at maximum gain. The digitization card can directly be installed into the computer to store the time tags to disc.

2.2. Basic data analysis

2.2.1. Input data

When running a measurement with the TimeHarp hard- and software a binary output file is created, a ".ptu"-file which contains the information about the arrival times of the photons for each channel. A ptu file reader available from the PicoQuant company can produce a human-readable output file including a photon list. The list is not sorted by input channels but by the original arrival times, so each time tag contains basically three information:

- The **event number** which is simply a counting index increasing by one for each new event.
  However, it must be mentioned that it periodically omits one number, namely when the arrival time of the photon stored in the binary file exceeds its buffer size. Then an "overload" event is recognized which is no photon but just tells the computer to restart the time tag at zero. The ptu-reading program then adds one extra buffer size time value to the stored arrival time in order to keep the correct arrival times, as it is crucial to obtain genuine time differences later in the analysis.

- The **channel number** which gives the information about the input channel the photon was recognized. As only two input channels 0 and 1 exist, this value is either 0 or 1.

- The **arrival time** of the photon which is given in picoseconds and is a multiple of 250 ps, as this is the bin size of the TDC.

These three information allow for a complete analysis of the correlation measurement. A fictional example extract of such a list is shown in table 1 in section 2.2.2. Note that all TimeTag values are dividable by 250.

2.2.2. Time difference spectra

Customization of $g^{(2)}$ parameters to measurement parameters

The goal is to run an analysis method which creates a graph that can be interpreted as the $g^{(2)}$ function. Therefore let us recall the definition of the temporal $g^{(2)}$ function:

$$g^{(2)}(\tau) = \frac{\langle I(t) \cdot I(t+\tau) \rangle}{\langle I(t) \rangle^2} \tag{2.3}$$

For each time difference τ one has to compare intensities at a time t with intensities at a time $t + \tau$ for all t. While there is no natural quantization of t in the $g^{(2)}$ function, it is in fact in the measurement due to the TDC binning. This yields the first adaptation of "nature" to the experiment:

- The former continuous **time** t is quantized by the minimum bin width $\Delta t_{\text{bin}} = 250\,\text{ps}$. This holds for the **time difference** τ as well, since time differences of multiples of 250 ps are again multiples of it.

The second problem is the interpretation of *intensity*. Again in an natural system there is no limit and no quantization of intensity, it is a continuous curve evaluating in time, however, the only thing one can obtain from the measurement is whether there is a photon time stamp at a certain time t or not. There is also no information about the number of photons.

- The **intensity** $I(t)$ at a time t consists of only two states: $I(t) = 1$ if there is a photon, $I(t) = 0$ if there is none.

What do these perceptions mean to the numerator of equation 2.3? Averaging over the product $I(t) \cdot I(t + \tau)$ does not mean integrating over t any more, but summarizing this expression over all possible time stamps:

$$\int_t I(t) \cdot I(t+\tau) dt \rightarrow \sum_t I(t) \cdot I(t+\tau) \tag{2.4}$$

The argument of the sum is the product of two intensities which can only be 0 or 1, hence this holds also for the product itself, it is comparable to an *and gate*. The sum over all time bins t at a given time difference τ returns the absolute number of coincidences corresponding to τ.

Creating the time difference spectra

A spectrum showing the number of coincidences for each time difference τ is already very close to the $g^{(2)}(\tau)$ function. It only has to be normalized which is done by the denominator in equation **2.3**. The normalization in the measurement analysis is explained below, but first, it will be shown how to create the time difference spectrum in an optimal way that requires the shortest possible computation time. There are two different types of time difference spectra depending on the channels that contribute to them.

- **Auto-correlation spectra** contain only photon time differences of the same channel, so channel 0 events minus channel 0 events or channel 1 events minus channel 1 events. As one will see in auto-correlation spectra certain electronic effects like the dead time of the electronics or afterpulsing systematics can be found.

- **Cross-correlation spectra** contain photon time differences of photons of different channels, namely channel 1 events minus channel 0 events or channel 0 events minus channel 1 events. Cross-correlation spectra are the most interesting ones since photon bunching is visible here.

These two kinds of histograms can again be split into two spectra of each kind. Concerning the auto-correlation one can distinguish between the channel 0 auto-correlation and the channel 1 auto-correlation which can systematically differ if e.g. the PMTs have different behaviors. The cross-correlations can be divided into one histogram where channel 1 events are subtracted from channel 0 events and one where channel 0 events are subtracted from channel 1 events.
As seen above these time difference spectra can be generated by calculation of the coincidence number for one time difference τ and finally varying τ in the desired range. For one time difference this can work in the following way:

- Take the first entry of the measurement list e.g according to table **1** and look at the arrival time tag t. This photon will be called *basic photon*.

- Check, if there is a coincidence photon at the time difference $t + \tau$ by passing through the list. The algorithm can stop when the time difference of a photon to the basic one exceeds $\tau_{\max}$, as successive photons can only have a larger time difference.

- If a photon with matching time difference was found, the value of the bin corresponding to τ in the histogram is increased by one. Here it is important to check if the compared photon belongs to the same channel as the basic one ore not. Only if the channels are different, the histogram of the cross-correlation can be filled.

- Switch to the next (the second) entry of the list and repeat the procedure.
- After all entries, the value of the time difference τ can be changed and the same analysis can be done again until all desired values τ are investigated.

By this analysis method, the time difference spectrum can be systematically generated. However, this computation takes a rather long time and is not very efficient, since there are lots of compare operations which do not lead to a coincidence, especially if the photon rate is low. This can be illustrated by the following example:
Imagine a measurement with photon rates of $\dot{N}_0 = \dot{N}_1 = 10\,\mathrm{MHz}$, which is quite a lot. Setting a bin width of $\Delta t_{\mathrm{bin}} = 250\,\mathrm{ps}$ and measuring $T = 1\,\mathrm{s}$ leads (also for uncorrelated photons) to an expected event number of $M = \dot{N}_0 \dot{N}_1 \Delta t_{\mathrm{bin}} T = 25000$ per bin (see section 2.3.1). In contrast, the total size of the photon list is $(\dot{N}_0 + \dot{N}_1) \cdot T = 20 \cdot 10^6$. This means that the success fraction of finding a coincidence e.g. for the cross-correlation spectrum is $\frac{25000}{20 \cdot 10^6} = 0,125\%$.
Luckily there is a more efficient method of creating the spectrum:

- Take the first entry and look at the arrival time of this basic photon.
- Go to the next photon, called *investigation photon* and calculate the time difference. This value can directly be filled into the time difference spectrum of the corresponding τ. The only thing one has to check is the relation between the two channels. If the channels are the same, the time difference event belongs to the auto-correlation of one PMT. If they differ, the event belongs to the cross-correlation.
- Switch to the next investigation photon and calculate the time difference to the basic photon again, the same procedure can be done until the time difference between the basic and the investigation photon exceeds the maximum τ one is interested in.
- switch to the second photon as basic photon and repeat the method again.

By this procedure, the time difference spectra can be generated efficiently, as **every** comparison leads to a coincidence now. However, there is still a difference between coincidences of the same channel (auto-correlation) and coincidences of different channels (cross-correlation) which have to be separated. Later in the experiments, the cross-correlation between channels 0 and 1 is of higher interest, but having the chance to analyze the auto-correlation has some benefits as well, since it contains interesting information about systematics of the measurement.

Examples and types of time difference histograms

When having a photon list the time difference spectra/histograms can be built. There are four different histograms that are created: The two auto-correlation histograms for channel 0 and 1, respectively, and two cross-correlation histograms which compare events of channel 0 with events of channel 1 in the "0-1 histogram" and vice versa in the "1-0 histogram". Let's try this out with the example from table 1.

Event number	Channel	TimeTag [ps]
1	1	750
2	0	2250
3	1	4000
4	1	4250

Table 1.: Example photon arrival list

The first basic photon has the time tag $t = 750\,\text{ps}$ and was detected in channel 1. The comparison to the second photon gives a time difference of $\tau = 2250\,\text{ps} - 750\,\text{ps} = 1500\,\text{ps}$. Therefore a time difference spectrum is filled by 1 at the value 1500 ps. As the second photon was detected in channel 0, the coincidence event must be filled into the **1-0-histogram**. The nomenclature of the histogram works in the following way: The channel ID of the basic photon is mentioned firstly, the ID of the investigation photon secondly. The 1-0-histogram belongs to the cross-correlation histograms, as different channel events are stored here.
Now the investigation photon is event number 3, which has a time tag of 4000 ps, the time difference to the basic photon is $\tau = 3250\,\text{ps}$, the corresponding bin value in the histogram is increased by 1. The investigation channel is 1 as well as the basic channel, therefore the value must be filled into the **1-1-histogram**. This is the auto-correlation histogram of channel 1.
Finally, the last photon in the list is event number 4 at time 4250 ps with $\tau = 3500\,\text{ps}$, which belongs to the 1-1-histogram as well. After reaching the last photon for investigation or a photon's time difference that exceeds the maximum evaluation time difference, the basic photon ID is switched to the second one. This event again can be compared to all other entries, even to entries that are earlier in time, like event 1. The time difference of basic photon 2 to investigation photon 1 is $\tau = 750\,\text{ps} - 2250\,\text{ps} = -1500\,\text{ps}$, a negative time difference that can be filled into the 0-1-histogram. One may recognize, that these two photons already have been compared and filled with their positive time difference into the 1-0-histogram. This is one of a few symmetry recognitions one can find about the time difference histograms:

- The **0-1** and **1-0 cross-correlation histograms** are mirror-inverted against each other around zero. This is due to the fact that a coincidence of a channel-0-photon with a channel-1-photon appears in the 0-1-histogram as well as in the 1-0-histogram, but with different sign.

- The **0-0** and **1-1 auto-correlation histograms** are mathematically independent from each other, but each auto-correlation histogram is mirror-symmetrical to itself around zero, as a the time difference of photon i with photon j will appear again with different sign, when photon j will be the basic photon.

Thus, all information could be stored by looking at only positive (or negative) time differences in the four time difference spectra. For the cross-correlation it would be sufficient to calculate either only one time direction (positive or negative) or one cross-correlation histogram. However, as the final algorithm is built in a way that it does not make more effort to fill all four histograms with all time differences, the four time difference spectra will be created within the whole evaluation range.
It should be mentioned that there is no need to set the bin sizes of the time difference histograms need to 250 ps, as the analysis software is written using the ROOT-package for C++ developed by CERN [33], which provides an easy way of creating histograms, any bin size can be set. Only bin sizes < 250 ps do not make sense since all time differences are multiples of 250 ps, smaller bin sizes would lead to strange binning effects.

2.2.3. Normalization - The $g^{(2)}$-function

Now it is clear how to build the time difference spectrum. However, there is still a difference between this spectrum and the $g^{(2)}$ function. Not even the numerator of equation **2.3** is evaluated correctly yet: In case of discrete time points the numerator becomes

$$\langle I(t) \cdot I(t+\tau) \rangle = \frac{1}{N} \sum_{i=1}^{N} I(t_i) \cdot I(t_i + \tau) \tag{2.5}$$

where N is the total number of datapoints. The denominator becomes

$$\langle I(t) \rangle^2 = \left(\frac{1}{N} \sum_{i=1}^{N} I(t_i) \right)^2 \tag{2.6}$$

and the whole expression for the $g^{(2)}(\tau)$

$$g^{(2)}(\tau) = \frac{\frac{1}{N}\sum_{i=1}^{N} I(t_i)\cdot I(t_i+\tau)}{\frac{1}{N^2}(\sum_{i=1}^{N} I(t_i))^2} = N\cdot\frac{\sum_{i=1}^{N} I(t_i)\cdot I(t_i+\tau)}{(\sum_{i=1}^{N} I(t_i))^2} \tag{2.7}$$

This expression also holds for intensities $I(t_i) > 1$[1].
Let's test if this equation is consistent with expectations by calculating an autocorrelation function: Consider an uncorrelated light measurement, where one expects $g^{(2)}(\tau) = 1\,\forall\tau$. Imagine now a series of uncorrelated photons which arrive at the times t_i. The total measurement time is T, the bin size is the minimum bin size of the electronics $\Delta t_{\mathrm{bin}} = 250\,\mathrm{ps}$. The total number of time bins in the rough measurement is therefore $N_{\mathrm{b}} = \frac{T}{\Delta t_{\mathrm{bin}}}$. In the whole measurement time N_{p} photons are detected. Figure 2.7 visualizes the time line with arriving photons.

Figure 2.7.: Idea of a measurement result: The squares are time bins, the blue dots symbolize randomly distributed arriving photons. Note that in the arrival time list the empty bins are not listed.

The $g^{(2)}(\tau)$ function according to equation 2.7 will be calculated, starting with the denominator:

$$\underbrace{(\sum_{i=1}^{N} I(t_i))^2}_{N_{\mathrm{p}}} = {N_{\mathrm{p}}}^2 \tag{2.8}$$

Since $I(t) = 1$ if there is a photon and $I(t) = 0$ if there is none. The N from equation 2.7 is N_{b}, the numerator can be calculated in two similar ways: The first way is by summarizing over all bins:

$$\sum_{i=1}^{N_{\mathrm{b}}} \underbrace{I(t_i)}_{P(1)=\frac{N_{\mathrm{p}}}{N_{\mathrm{b}}}} \cdot \underbrace{I(t_i+\tau)}_{P(1)=\frac{N_{\mathrm{p}}}{N_{\mathrm{b}}}} = \sum_{i=1}^{N_{\mathrm{b}}} \frac{{N_{\mathrm{p}}}^2}{{N_{\mathrm{b}}}^2} = N_{\mathrm{b}}\frac{{N_{\mathrm{p}}}^2}{{N_{\mathrm{b}}}^2} = \frac{{N_{\mathrm{p}}}^2}{N_{\mathrm{b}}} \tag{2.9}$$

as for randomly filled bins the probability for having a photon in the bin is $P(1) = \frac{N_{\mathrm{p}}}{N_{\mathrm{b}}}$. The second way is by starting only with photon-containing bins t_j:

[1] $I(t_i) > 1$ could occur if one summarizes certain time bins in the arrival time list, however this method does not make sense concerning photon counting as one loses time resolution and had to measure for a long time to see bunching effects.

$$\sum_{j=1}^{N_\mathrm{p}} \underbrace{I(t_j)}_{1} \cdot \underbrace{I(t_j+\tau)}_{P(1)=\frac{N_\mathrm{p}}{N_\mathrm{b}}} = \sum_{t_i=1}^{N_\mathrm{p}} \frac{N_\mathrm{p}}{N_\mathrm{b}} = N_\mathrm{p}\frac{N_\mathrm{p}}{N_\mathrm{b}} = \frac{{N_\mathrm{p}}^2}{N_\mathrm{b}} \tag{2.10}$$

Both methods, of course, lead to the same result. The total expression of the $g^{(2)}(\tau)$ is then

$$g^{(2)}(\tau) = N_\mathrm{b} \cdot \frac{\sum_{i=1}^{N} I(t_i)\cdot I(t_i+\tau)}{(\sum_{i=1}^{N} I(t_i))^2} = N_\mathrm{b} \cdot \frac{\frac{{N_\mathrm{p}}^2}{N_\mathrm{b}}}{{N_\mathrm{p}}^2} = 1 \tag{2.11}$$

which is in agreement with expectations. The described formula is therefore the correct way to normalize the time difference spectrum, however, it is rather complicated and there is a more convenient experimental way: As one expects $g^{(2)}(\tau) = 1$ for $|\tau| \gg 0$, it is also possible to normalize the time difference spectrum by calculating the mean value of it in a range far beyond the correlation regime. Since this is just one computation step from the time-difference histograms to the $g^{(2)}$ function, division by the mean value in the "tail" region of the histograms, this is the way the correlation spectra shown in this thesis usually will be normalized. A fictional example is given in figure 2.8. Here a time-difference histogram with several bins is plotted. The average count number per bin of ≈ 20 is extreme small compared to measurements later. At $\tau = 0$ there is an excess in coincidence counts which can origin in photon bunching, however, the supposed signal is not very significant.

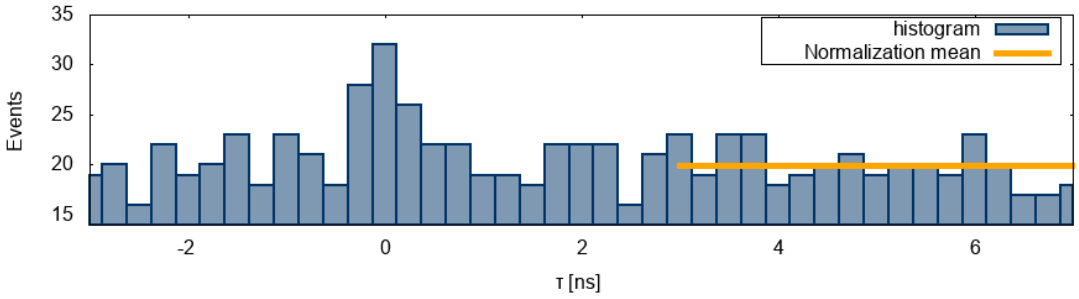

Figure 2.8.: Example time difference histogram. In the outer region the mean is calculated for normalizing.

In the "outer" range defined as $\tau > 3\,\mathrm{ns}$ the mean event value is calculated. The normalization can now be done by just dividing every bin value by the mean, the shape of the graph does not change but only the values of the vertical axis.

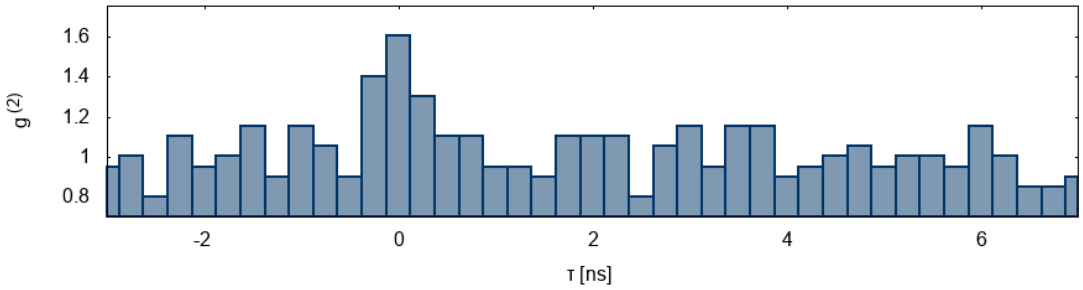

Figure 2.9.: The normalized time difference histogram can be interpreted as $g^{(2)}$ function.

The clue of only taking the outer part of the histogram for normalization is that possible signals have no influence on normalization. If one would take the whole range the enhancement at $\tau = 0$ would decrease the overall $g^{(2)}$ level to < 1. Normally this effect is extreme small especially when only bunching signals increase the histogram counts, however, as one will see there are certain disturbances around zero beyond photon bunching that have an effect on the spectra which should be excluded for normalization.

2.3. Expectations on statistics and measurement times

This section deals with the question, how long is it necessary to measure until one sees a signal with a certain significance? In other words, how trustworthy is a measurement which shows a supposed signal in the $g^{(2)}$ function that is elevated compared to the statistical fluctuations of the uncorrelated part in the $g^{(2)}$ function? Therefore it is essential to calculate the expected number of counts in each time difference bin, its uncertainty and the effect on the normalized $g^{(2)}$ function.

2.3.1. Statistics in an uncorrelated regime

To compute the expected event number depending on the binwidth Δt_{bin} one can imagine a measurement with total measurement time T_{t} and total numbers of events N_0 and N_1 in channel 0 or 1. The total number of possible coincidences in the whole time regime is $N_0 \cdot N_1$, as every photon from channel 0 can be compared to every photon in channel 1. Summing up all these coincidences one has to take into account that the corresponding time differences τ are also negative, e.g. the last photon in channel 0 has a time difference to the first photon in channel 1 of nearly $\tau = -T_{\mathrm{t}}$. Furthermore, consider that large time differences cannot occur as

often as small ones, restricted by T_t. While the maximum number of events per bin should lie in the region around $\tau = 0$ it decreases linearly towards zero at $\tau = T_t$ or $\tau = -T_t$. Figure 2.10 shows the expected event numbers.

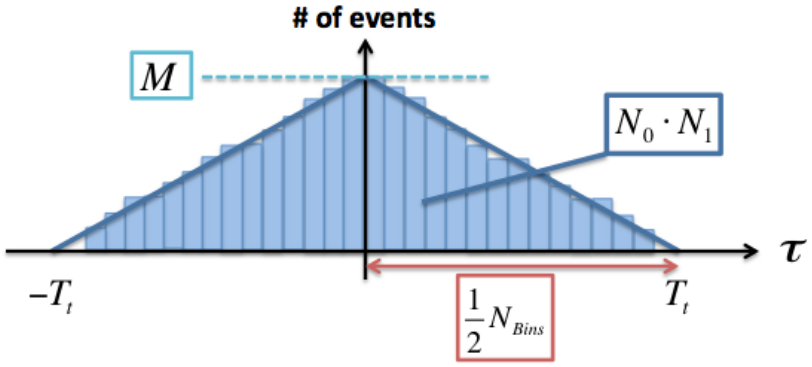

Figure 2.10.: Number of coincident events depending on the time difference τ

The binning shown in figure 2.10 would correspond to an either extremely big binwidth Δt_{bin} or an extremely short measurement time T_t. The binwidths are typically in the range of $< 1\,\text{ns}$ (the smallest reasonable binwidth is the TDC-binning of the TimeHarp hardware, which is $\Delta t_{\text{bin}} = 250\,\text{ps}$). Usually the evaluation region is only a few hundred nanoseconds, whereas measurement times are in the range of minutes or even hours. Therefore the effect of decreasing event numbers in the time-difference spectrum with larger time differences is extremely small in the evaluation regime, one expects a fluctuation of the event numbers per bin around the value M drawn in the plot.
This value M can be derived by setting up equation 2.12, deduced geometrically from figure 2.10:

$$N_0 \cdot N_1 = 2 \cdot \Delta_{0MT_t} = 2 \cdot \frac{1}{2} \cdot \frac{1}{2} N_{\text{Bins}} \cdot M \tag{2.12}$$

where Δ_{0MT_t} is a triangle with corners at the origin, M and T_t. Solved for M using $N_{\text{Bins}} = \frac{2T_t}{\Delta t_{\text{bin}}}$

$$M = N_0 \cdot N_1 \cdot \frac{\Delta t_{\text{bin}}}{T_t} \cdot \frac{T_t}{T_t} = \dot{N}_0 \cdot \dot{N}_1 \cdot \Delta t_{\text{bin}} \cdot T_t \tag{2.13}$$

Where $\dot{N}_0 = \frac{N_0}{T_t}$ and $\dot{N}_1 = \frac{N_1}{T_t}$ are the (average) count rates. Assuming Poisson statistics for the fluctuations in event numbers the uncertainty is

$$\Delta M = \sqrt{M} = \sqrt{\dot{N}_0 \cdot \dot{N}_1 \cdot \Delta t_{\text{bin}} \cdot T_t} \tag{2.14}$$

In the picture of the $g^{(2)}$ function one just has to normalize the time difference spectrum via dividing each bin by the average number of coincidences, which is almost exactly M in the evaluation region, the theoretically expected fluctuation of the baseline is

$$\sigma_{g^{(2)}} = \frac{\Delta M}{M} = \frac{1}{\sqrt{M}} = \frac{1}{\sqrt{\dot{N}_0 \cdot \dot{N}_1 \cdot \Delta t_{\mathrm{bin}} \cdot T_{\mathrm{t}}}} \tag{2.15}$$

Comparing the experimental results with this theory value is a good criterion to judge whether the baseline is stable or not for any measurement time.

2.3.2. Height of the correlation signal and significance

The effect of a correlation signal in the measured $g^{(2)}(\tau)$ spectrum can be calculated when knowing the correlation time of the light source and its line width, respectively. The $g^{(2)}$ function in theory follows the equation $g^{(2)}(\tau) = 1 + e^{-\frac{2|\tau|}{\tau_c}}$ for Lorentzian light and $g^{(2)}(\tau) = 1 + e^{-2\pi(\Delta\nu\tau)^2}$ for Gaussian light. Even if one assumes a small time resolution of the electronics which is then dominated by the TDC binning of $\Delta t_{\mathrm{bin}} = 250\,\mathrm{ps}$ the time steps are still orders of magnitude above typical correlation times which lie in the range of picoseconds or below. It is therefore impossible to sample the shape of the $g^{(2)}$ function but the whole effect of a larger number of counts will affect only one bin at $\tau = 0$. Broadening of the peak into several bins of course can occur due to a time resolution in the range of a few hundred picoseconds. The total effect can be calculated from the area under the curve of the $g^{(2)}(\tau)$ function relative to 1, as figure 2.11 shows.

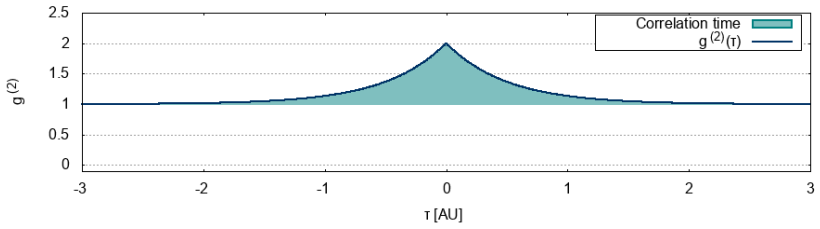

Figure 2.11.: $g^{(2)}(\tau)$ for Lorentzian light on picosecond time-scale. The filled area is τ_c

The signal strength turns out to be the correlation time:

$$S = \int_{-\infty}^{\infty} g^{(2)}(\tau) - 1 \; d\tau = \int_{-\infty}^{\infty} e^{-\frac{2|\tau|}{\tau_c}} = \tau_c \tag{2.16}$$

When observing Gaussian light the same result can be found by defining the correlation time appropriate. In section 1.2.3, equation 1.46 the shape of the $g^{(2)}$

function of chaotic light with Gaussian-shaped profile was derived. The integrated signal turns out to be

$$S = \int_{-\infty}^{\infty} e^{-2\pi(\Delta\nu\tau)^2} = \frac{1}{\sqrt{2}\cdot\Delta\nu} = \frac{\lambda_0^2}{\sqrt{2}\cdot c\cdot 1.06\Delta\lambda_{\mathrm{FWHM}}} = \tau_{\mathrm{c,\ Gaussian}} \tag{2.17}$$

when defining the correlation time as

$$\tau_{\mathrm{c,\ Gaussian}} := \underbrace{\frac{1}{1.06\cdot\sqrt{2}}}_{:=k}\cdot\frac{\lambda_0^2}{c\cdot\Delta\lambda_{\mathrm{FWHM}}} \tag{2.18}$$

where $k \approx 0.667$ describes the factor differing from the conventional definition of the correlation time.

Ideal electronics: No timing jitter

Considering a perfect system with an electronic time resolution of $\tau_e = 0$, but with a TDC binning of 250 ps. The whole correlation signal is now stored in the first bin[2]. Choosing the smallest binwidth $\Delta t_{\mathrm{bin}} = 250\,\mathrm{ps}$ the expected height of the first bin relative to 1 can be calculated.

$$S = \tau_c = h\cdot\Delta t_{\mathrm{bin}} \Rightarrow h = \frac{\tau_c}{\Delta t_{\mathrm{bin}}} \tag{2.19}$$

A quantitative statement of the measured signal is the significance n as the ratio of the signal bin and the background

$$n = \frac{S}{B} \tag{2.20}$$

In theory one expects the background to be Poissonian according to equation 2.15. The significance then is

$$n = \frac{h}{\sigma_{g^{(2)}}} = \frac{\tau_c\cdot\sqrt{\dot{N}_0\dot{N}_1 T_{\mathrm{t}}\Delta t_{\mathrm{bin}}}}{\Delta t_{\mathrm{bin}}} = \tau_c\cdot\sqrt{\frac{\alpha}{\Delta t_{\mathrm{bin}}}} \tag{2.21}$$

introducing the **statistic factor** $\alpha = \dot{N}_0\dot{N}_1 T_{\mathrm{t}}$.
Equation 2.21 has an important consequence: The count rates of the single detectors as well as the measurement time enter the equation in the radicand. This means that doubling the significance without changing other parameters requires

[2] The phrase 'first bin' is used for the bin which corresponds to $\tau = 0$. As the evaluation range can be chosen arbitrarily with also negative τ, this might and will not necessarily be the first bin in the $g^{(2)}$-histograms.

a four times bigger measurement time. Same holds for the counting rates, it is therefore desirable to adjust the measurement set-up in a way that the rates become maximal to minimize the measurement time.

Real electronics with timing jitter

The time resolution of the electronics, predominantly caused by the timing jitter of the PMT pulses, spreads the correlation signal over several bins. The signal strength S, which should again be the correlation time τ_c, if there are no losses, is now the peak area.
The resulting peak can be assumed to be Gaussian, the signal strength S can now be calculated by determining the area under the Gauss peak. Figure **2.12** shows the correlation signal of the mercury lamp, as it will be discussed in section 4.2 and a fit of a Gaussian function of the form

$$f(\tau) = A \cdot e^{-\frac{(\tau-\mu)^2}{2\sigma_t^2}} + B \tag{2.22}$$

The offset B should be close to one, as the $g^{(2)}$ function is normalized. Therefore it is also reasonable to set this parameter to 1 without fitting it.

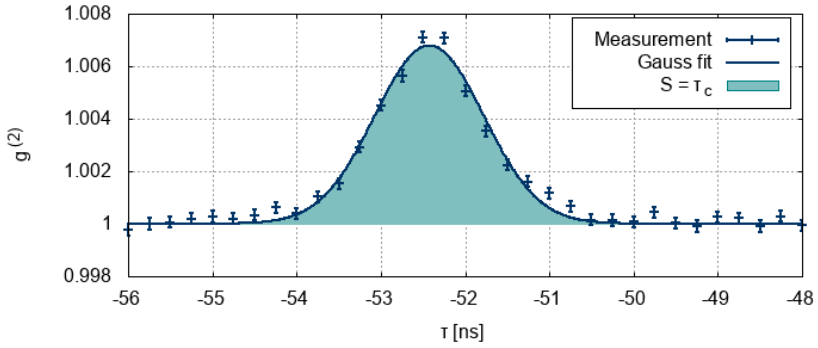

Figure 2.12.: Measured correlation signal of the mercury lamp

The integral of the entire Gauss-function (blue area in figure **2.12**) is given by

$$S = \tau_{\text{c, measured}} = a \cdot \sigma_t \cdot \sqrt{2\pi} \tag{2.23}$$

The problem which needs to be solved for calculating the significance $n = \frac{S}{B}$ is to evaluate the background B of this peak. Therefore imagine to calculate the peak area by summarizing the bin values s_i of N_{bins} bins in the peak regime. The signal would then be

$$S = \Delta t_{\text{bin}} \cdot \sum_{i=1}^{N_{\text{bins}}} s_i \tag{2.24}$$

Hence, the uncertainty is

$$\Delta S = \Delta t_{\text{bin}} \cdot \sqrt{\sum_{i=1}^{N_{\text{bins}}} \Delta s_i^2} \tag{2.25}$$

where Δs_i is the uncertainty of one bin. It can be determined by filling the measured $g^{(2)}(\tau)$ in a time regime, where no correlations should exist and white noise is expected, into a histogram and calculating the RMS. But it again can be computed theoretically via equation 2.15. This follows the assumption that all signal bins have the same uncertainty $\Delta s_i = \Delta s \, \forall \, i$. Then the background signal uncertainty becomes

$$\Delta S = \Delta t_{\text{bin}} \sqrt{N_{\text{bins}} \Delta s^2} = \Delta t_{\text{bin}} \Delta s \sqrt{N_{\text{bins}}} \tag{2.26}$$

Of course equation 2.26 requires start- and end-bins for the calculation to gain the parameter N_{bins}, which are not given by the nature of the Gaussian function as its values never decrease to zero. Hence, as a convention the range of two standard deviations σ_t left and right from the medium of the Gaussian are set as limits. This total evaluation length is called D.

$$D = 4 \cdot \sigma_t \tag{2.27}$$

Transferring this to the bin view

$$D = N_{\text{bins}} \Delta t_{\text{bin}} \Rightarrow N_{\text{bins}} = \frac{D}{\Delta t_{\text{bin}}} \tag{2.28}$$

the uncertainty on S, which is the background, can be derived.

$$B = \Delta S = \Delta t_{\text{bin}} \Delta s \sqrt{\frac{D}{\Delta t_{\text{bin}}}} = \Delta s \sqrt{4 \Delta t_{\text{bin}} \sigma_t} \tag{2.29}$$

This gives an expression for the significance

$$n = \frac{S}{B} = \frac{\tau_c}{\Delta s \sqrt{4 \Delta t_{\text{bin}} \sigma_t}} \tag{2.30}$$

Assuming no systematics the expected significance depending on the measurement time can be derived using equation 2.15:

$$n = \sqrt{\frac{\tau_c^2 \alpha}{4\sigma_t}} = \sqrt{\frac{\tau_c^2 \dot{N}_0 \dot{N}_1 T}{4\sigma_t}} \Leftrightarrow T = \frac{4n^2\sigma_t}{\tau_c^2 \dot{N}_0 \dot{N}_1} \tag{2.31}$$

This gives an expectation of the required measurement time T for any significance n. Again it grows quadratically with the significance.
One also can express the correlation time by the optical bandwidth via $\tau_c = k \cdot \frac{\lambda_0^2}{c\Delta\lambda}$.

$$T = \frac{4n^2\sigma_t c^2 (\Delta\lambda)^2}{k^2 \lambda_0^4 \dot{N}_0 \dot{N}_1} \tag{2.32}$$

where $k = 1$ for Lorentzian and $k = 0.667$ for Gaussian light.
Latter formula has interesting consequences: It is actually important to keep the optical bandwidth as small as possible to maximize the $g^{(2)}$ signal. However, i.e. doubling the optical bandwidth $\Delta\lambda$ should also double each photon rate $\dot{N}_0$ and $\dot{N}_1$, these two effects cancel out in equation **2.32**. Therefore the optical bandwidth in general does not affect the required measurement time for a given significance. The reason is that a broader bandwidth reduces the absolute height of the bunching signal, but in the same time higher statistics decrease the uncertainties on each bin.
Nevertheless there are good reasons to keep $\Delta\lambda$ small. High rates on a broader bandwidth necessitate more disc storage since more photon time tags are recorded and lead to longer evaluation times to create the $g^{(2)}$ spectra out of the raw data. Furthermore it might cause some problems to keep the baseline of the $g^{(2)}$ function stable in terms of showing no systematics or unexpected fluctuations on even smaller dimensions.
However, when intensity interferometry is done with huge telescopes like CTA or HESS where light beams from different parts of the telescope mirrors arrive in different angles making interference filtering difficult one might make use of the general independence of the measurement time from the optical filtering.
Let's look at three examples that can be executed in the lab or with small telescopes: A gas discharge lamp with an optical linewidth of $\Delta\lambda = 50\,\mathrm{pm}$ centered at $\lambda_0 = 546\,\mathrm{nm}$ which may correspond to a mercury lamp. If one achieves 10 MHz at each PMT and requests a significance of $n = 5$ the required measurement time according to equation **2.32** is

$$T_{\mathrm{Hg}}(n = 5) = 3.7\,\mathrm{s} \tag{2.33}$$

where $\sigma_t = 650\,\mathrm{ps}$ which is a reasonable time resolution. LEDs have a broad wavelength range so that they may be actively optically filtered. A LED that will be used in this thesis can be brought to photon rates of 10 MHz per PMT using a $\Delta\lambda = 1\,\mathrm{nm}$ interference filter centered at $\lambda_0 = 532\,\mathrm{nm}$. Then, in theory

$$T_{\mathrm{LED}}(n = 5) = 27\,\mathrm{min} \tag{2.34}$$

Finally, imagine observation of a star with same filter properties as the LED but with lower rates. Even with telescopes with a diameter of 0.5 m photon rates of only 2 MHz per PMT are expected for bright stars. Thus one obtains

$$T_{\mathrm{Star}}(n = 5) = 11\,\mathrm{hr} \tag{2.35}$$

which is already more than a whole night. Furthermore upper calculations still did not take signal losses and systematics into account that further increase T.

3. Temporal correlation measurements

After putting together all devices for detecting and processing photon signals correlation measurements can be done. Different light sources are used for different purposes. At first a handable setup using a laser beam hitting a rotating ground glass disc is arranged which creates gaussian-shaped correlation patterns with a correlation time of a few microseconds. It can be used to check if electronics and analysis work correctly. Incidentially effects like PMT afterpulsing and deadtime of the electronics can be seen in the $g^{(2)}$ spectra.
On picosecond time scale the electronics, especially the digitization card, reveal some periodic effects like nonlinearity of the time-to-digital converter and show influences of mobile communication frequencies to the $g^{(2)}$ spectrum. These effects have to be eliminated to see the small correlation signals of thermal light sources, the calibration methods are shown in this chapter.

Contents

3.1. Correlations on micro-second time scales

3.1.1. Setup with a laser and a rotating ground glass disk

The first correlation measurements were taken using the set-up shown below. Light source is a laser with a wavelength of $\lambda = 532\,\text{nm}$. As already described, a laser does not create bunching effects but should lead to a perfect $g^{(2)}(\tau) = 1\,\forall\tau$. But the laser can be used to simulate a quasi-thermal light source with a correlation time in the range of a few microseconds when putting a rotating ground glass disc

into the beam. The disk acts as a scatterer, light beams that enter the disc at a slightly different position travel another way through it with a different path length resulting in a complex diffraction pattern (speckle). By rotating the disk a specific speckle only exists as long as the disk area creating it is illuminated, only during that time artificial photon bunching can be measured. By varying the rotation speed the correlation time can be changed.
The beam can be guided to a beamsplitter to allow for measuring with two PMTs and channels at the same optical position. Auto-correlation spectra as well as cross-correlation histograms can be computed.

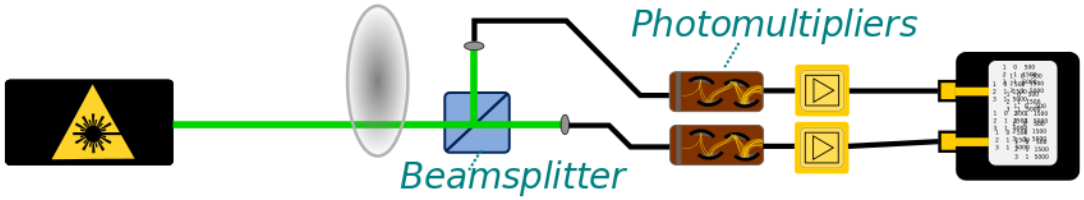

Figure 3.1.: Laboratory setup: A laser beam enters a rotating ground glass disc and afterwards the beamsplitter, before hitting fibers that lead to the PMTs

As the experiment deals with large and adjustable correlation times it can be used as a test measurement for the detection system. Furthermore it is a useful experiment to get familiar with the concept of time difference histograms and the effects that can be seen in this spectra.

3.1.2. Shape of the $g^{(2)}$ function

Theory

Laser light beams of the angular frequency ω_0 that impact the disc in different angles get shifted in frequency by different amounts $\Delta\omega$. Assuming a Gaussian incident angle distribution the resulting $\Delta\omega$ distribution is Gaussian as well which can be directly transferred to a Gaussian Power spectrum of the system [34]. According to the Wiener-Khinchine theorem the resulting $g^{(1)}$ function is again Gaussian-shaped, same holds due to the Siegert relation for the $g^{(2)}$ function.
A quantitative calculation yields the following expression for the $g^{(2)}$ function [34]

$$g^{(2)}(\tau) = 1 + e^{-\frac{\tau^2}{\tau_c^2}} \tag{3.1}$$

where $\tau_c = \frac{1}{v_{\mathrm{rot}}\sigma_k}$ with σ_k the width of the distribution of incident wave vectors. The formula nicely shows the decreasing coherence time with increasing rotation speed of the disk.

Auto-correlation spectra

Figure 3.2 shows the auto correlation time difference spectrum of one measurement with the former explained set-up at a rotation speed voltage of the ground glass disk of $U_{\text{rot}} = 1.3\,\text{V}$, and hence a relative slow rotation. The number of events is plotted against the time differences, this is not yet the normalized $g^{(2)}$ function. The bin size of this histogram was chosen to be $\Delta t_{\text{bin}} = 2\,\text{ns}$.

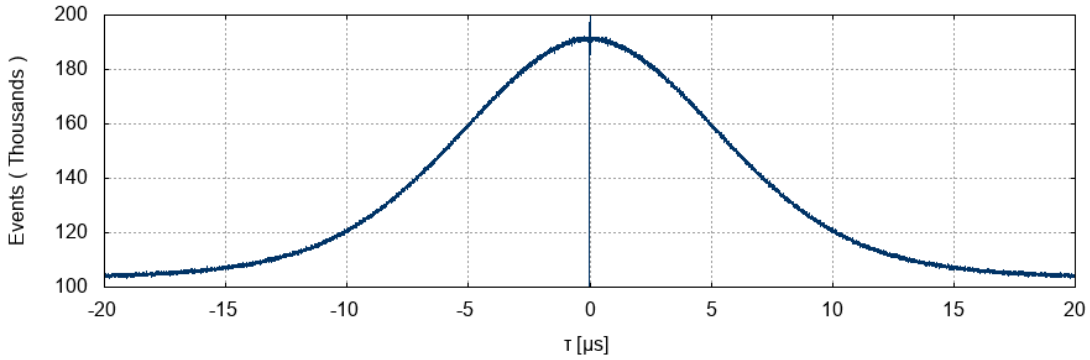

Figure 3.2.: Total coincidence events of PMT 0 at $U_{\text{rot}} = 1.3\,\text{V}$

The first thing that can be seen nicely is that the shape of the time difference spectrum looks like a gaussian function, just as expected. At small time differences[1] the number of events is much higher than at large ones, if one looks quantitatively at the event numbers it is approximately a factor of two, which will be shown below in detail when the normalized spectrum is given. This means that small time differences appear more often than large ones, but there is an exception: At very small time differences, there is a drastic drop of the event number, which can be guessed from figure 3.2 as the blue data points image a narrow line at $\tau = 0$. A more detailed look at this phenomenon is given in figure 3.3.
The bin size is now $\Delta t_{\text{bin}} = 250\,\text{ps}$ to investigate the effect in more detail. One can see that the event number is indeed 0 at small time differences and increases at about $|\tau| = 2\,\text{ns}$. The reason of this event drop is the dead time of the electronics: When a photon is detected, there is no other detection at the same channel until about 2 ns later, until a single photon pulse at the discriminator intersected the trigger threshold again. As mentioned before, this is the reason why temporal intensity interferometry with only one PMT with photon counting electronics does not work at correlation times smaller than the dead time of the electronics.
Another visible effect in the auto correlation function, seen in figure 3.2 as well as in figure 3.3 is the mirror symmetry around 0. This is not just a statistical effect, it is

[1] The expression "small time difference" refers to the absolute value of τ, which means $|\tau| \approx 0$.

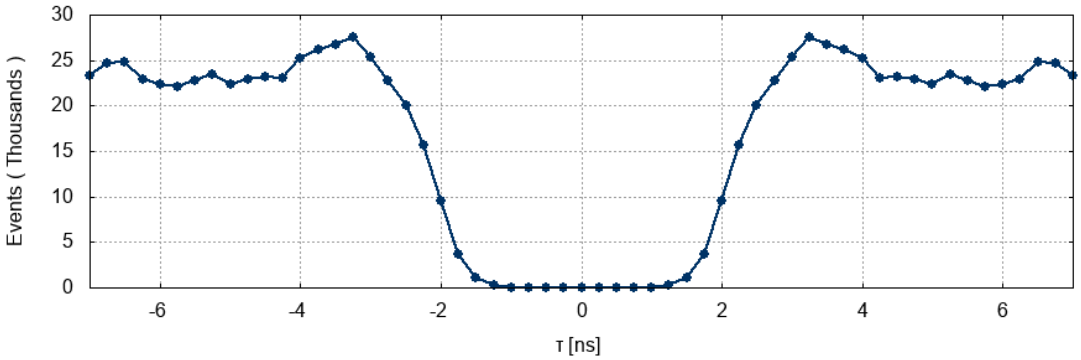

Figure 3.3.: Coincidence events vs. time difference: deadtime of the electronics causes event drop at small time differences

an exact mathematical fact, since in the auto-correlation, positive time differences appear in the negative spectrum as well when swapping basic and investigation photon.
Upper measurement was taken using multi-mode fibers at count rates of 9.8 MHz. When measuring with low rates of e.g. 0.4 MHz caused by using a single-mode fiber another effect becomes visible: afterpulsing. In figure 3.4, in which again the effect of less events at small τ can be seen, an event excess summarized in two peaks between $\tau = 20$ ns and $\tau = 30$ ns is measured. These peaks are PMT afterpulsing peaks, caused by ions that travel back to the photo-cathode and knock out another electron. As such afterpulsing events are strongly correlated in time with the first electron leaving the cathode, they create a clear signal in the time-difference spectrum.

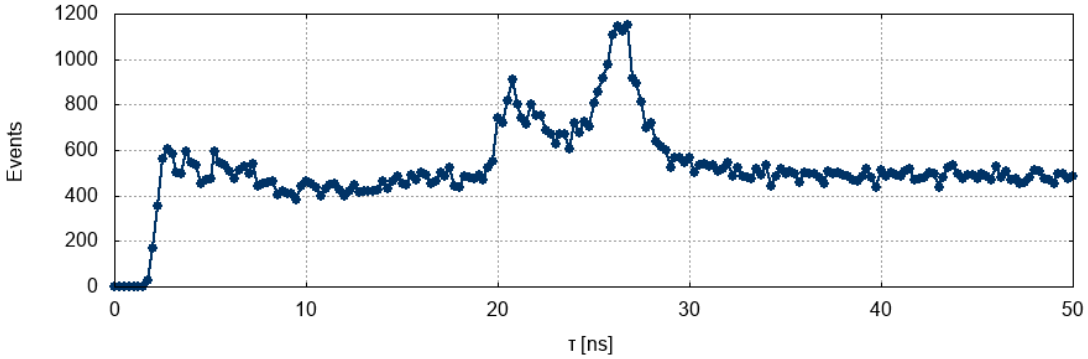

Figure 3.4.: Afterpulsing peaks in the range of 20 to 30 ns in the auto-correlation spectrum

The plots show that a few effects can be seen in the time-difference spectrum beside bunching peaks and could also be used as a tool to detect afterpulsing and to measure the dead time of the electronics.

$g^{(2)}$ patterns at different rotation speeds

The correlation time in this arrangement should be determined by the rotation speed of the ground glass disk. Varying this rotation speed is another test of the electronics and analysis. The faster the disk is rotating, the shorter the time a speckle influences the entry area of the fibers and the shorter the correlation time. These effects were measured as well as seen in figure **3.5**. The value on the vertical axis is now not the total event number any more, but normalized by the event number at large time differences. Therefore now these data equal $g^{(2)}$ values.

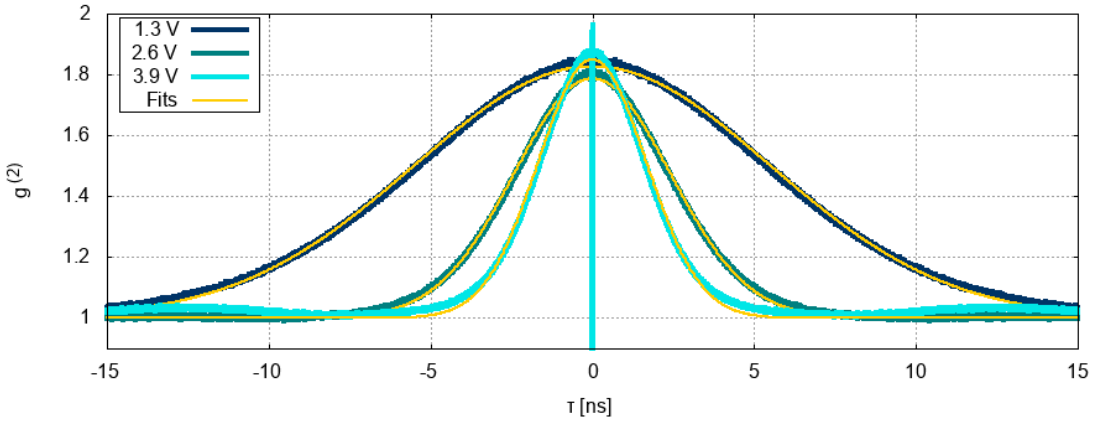

Figure 3.5.: $g^{(2)}(\tau)$ auto-correlation functions at different rotation speeds of the ground glass disk

Three different rotation voltages of the ground glass disk $U_{\text{rot}} \in \{1.3\,\text{V}, 2.6\,\text{V}, 3.9\,\text{V}\}$ are used, the angular velocity of the disk is directly related to the voltage, in the leading order the relation can be approximated to be linear. Figure **3.5** coincides qualitatively with expectations: The faster the disk is rotating, the shorter the correlation time. For a quantitative analysis Gaussian functions were fitted into the curves shown as yellow lines.
The correlation time τ_c can now be defined by the standard deviation σ of the Gauss fits. In figure **3.6** the resulting correlation times are plotted against the rotation voltage, a hyperbolic function is fitted into the data, as the correlation times are expected to be indirectly proportional to the angular velocity of the disk. Although there are only three data points the figure indicates that the system

behaves like expected, even if there are no further investigations on the concrete relation between the rotation speed and the voltage.

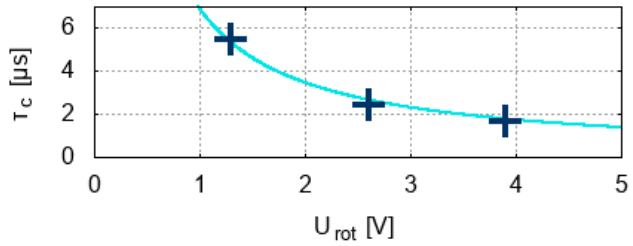

Figure 3.6.: Correlation time τ_c as σ of the Gauss fits of the auto-correlation functions with different rotation velocities of the disk (dark blue) and a hyperbolic fit (light blue)

As the spectra in figure **3.5** are normalized, the maximum $g^{(2)}$ value can directly be read from the curves at the maximum point near $\tau = 0$. It turns out to be close to 2, which is the theory value at $\tau = 0$, but below. This may have several effects. The normalization value may not be calculated perfectly, as it depends on the exact range one uses for computation, however, also physical effects can matter: Spatial coherence losses can decrease the signal as well.

Now it is time to look at the very first cross-correlation spectrum measured. As the correlation time of the system is large compared to typical real thermal light sources it is possible to measure the correlation signal using only one PMT and one channel. However, the same results should occur when viewing the cross-correlation between channel 0 and 1, at least if the fiber entries are placed at the same optical position compared to the beamsplitter. The cross-correlation $g^{(2)}(\tau)$ functions of the three measurements are given in figure **3.7**.

Again the decrease of the correlation time with increasing rotation speed is visible, as the Gauss functions become narrower, however, there is an obvious difference: The curves are not centered around $\tau = 0$, but shifted towards bigger time differences. Additionally they are shifted against each other, too. The smaller the rotation speed the larger is the shift of the curves to bigger τ. A reason for this effect can be found by looking at the set-up.

When the fibers are not located at the exact same optical position, which is quite an effort, they "see" another part of the ground glass disk and may not be within the same speckle. As the disk is moving, it can happen that the speckle then moves from the field of view of channel-0-fiber into the one of channel 1 within a certain time. This time duration causes the shift of the $g^{(2)}$ functions to exactly the duration time. The faster the disk is moving, the shorter is the time the disk

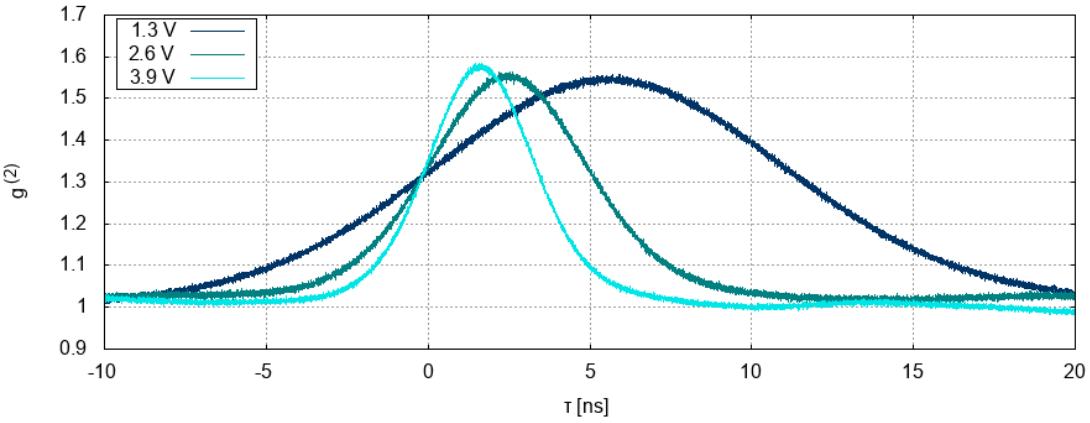

Figure 3.7.: $g^{(2)}(\tau)$ cross-correlation functions at different rotation speeds of the ground glass disk

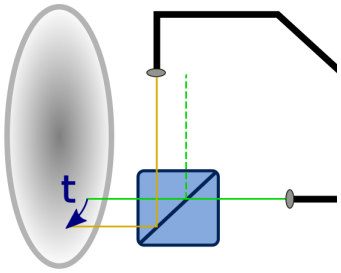

Figure 3.8: Exaggerated illustration: If the fiber entries are not placed at the same optical position, the cross-correlation maximum is shifted by the time t the disk needs to move into the focus of the other fiber.

needs to overcome this distance and therefore the shift in the $g^{(2)}$ histogram, which is exactly what is observed.

All in all this experiment shows that electronics and analysis work correctly at timescales of microseconds. To create the $g^{(2)}$-functions shown in this section the needed measurement time lies in the range of $T < 1\,\mathrm{s}$, except for the afterpulsing imaging, caused by the low counting rate the measurement time was $T = 5\,\mathrm{s}$. When moving to real thermal light sources with correlation times in the range of picoseconds, the produced signals are much smaller and the measurement times increase dramatically up to some hours. Apart from this, $g^{(2)}$ histograms which show signals on microsecond time scales do not need to have bin widths of $\Delta t_{\mathrm{bin}} = 250\,\mathrm{ps}$ but can be computed with $\Delta t_{\mathrm{bin}} \geq 2\,\mathrm{ns}$. This changes when measuring on picosecond times, as bunching effects are small enough that they are much less visible at bin sizes larger than a few hundred picoseconds. On this

time scales new problems will arise that need to be solved to see significant photon bunching peaks, as it will be shown hereafter.

3.2. Problems on pico-second time scales

Figure 3.9 shows a cross correlation measurement evaluated in the range of 25 ns around zero. One can see the absolute number of events as well as the normalized spectrum which is the $g^{(2)}$ function. For this measurement the photo-multipliers are separated to a distance of about 40 cm parallel to each other, illuminated by a LED. The photon rates at the PMTs are $\dot{N}_0 = 4.9\,\mathrm{MHz}$ and $\dot{N}_1 = 4.4\,\mathrm{MHz}$. The measurement time is $T = 30\,\mathrm{min}$, so for the first time this is a high-statistics measurement. As the PMTs are distant to each other no bunching signal is expected, this is a conscious arrangement to test the system for systematics, with this set-up one expects a perfect "1" everywhere in the $g^{(2)}$ spectrum, only influenced by statistical fluctuations. Choosing the smallest binwidth of $\Delta t_{\mathrm{bin}} = 250\,\mathrm{ps}$ for the $g^{(2)}$ spectrum, one can calculate the expected count numbers M for each bin and the fluctuations according to section 2.3.1.

$$M = \dot{N}_0 \cdot \dot{N}_1 \cdot \Delta t_{\mathrm{bin}} \cdot T_{\mathrm{t}} = 4.9\,\mathrm{MHz} \cdot 4.4\,\mathrm{MHz} \cdot 250\,\mathrm{ps} \cdot 30\,\mathrm{min} = 9.7 \cdot 10^6 \quad (3.2)$$

Looking at the event axis in figure 3.9 this fits quite well with theory. The expected fluctuations are

$$\sigma_{g^{(2)}} = \frac{1}{\sqrt{M}} = \frac{1}{\sqrt{9.7 \cdot 10^6}} = 3 \cdot 10^{-4} \quad (3.3)$$

That means the $g^{(2)}$ values are expected to lie mainly (1σ-uncertainty) within the range of $[0.9997 : 1.0003]$.
The figure displays that the $g^{(2)}$ distribution does not match the expectations at all but lie about an order of magnitude above. Furthermore the pattern shows distinct systematics, there is a high-frequency oscillation dominating the entire spectrum, however, there are other oscillations as well differing from statistics.
Apart from the fact that the spectrum does not look uniformly, is there a need of getting rid of the systematics? Yes, it is, as the expected signal later will be on a scale of 10^{-3} (Hg lamp) to 10^{-4} (LED) in the $g^{(2)}$ function. These signals would get lost in the big oscillations.
To get an idea of the kinds of oscillations a Fourier transformation uncovers all participating frequencies, as shown in figure 3.10.
There are two main peaks at 500 MHz and 1500 MHz, latter is a harmonic multiple of the first one. In section 3.2.2 it is shown that these peaks origin in the nonlinearity of the TDC inside of the digitization card.

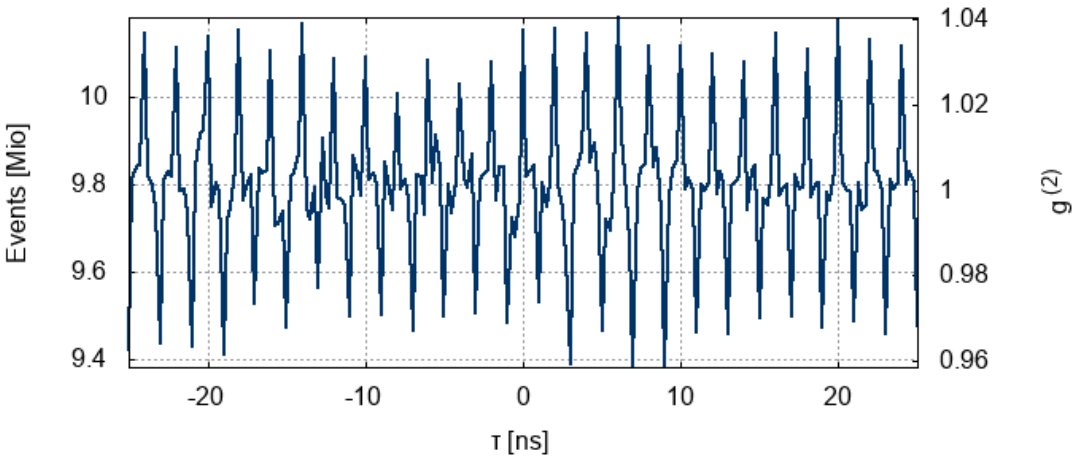

Figure 3.9.: The $g^{(2)}$ function is dominated by periodic peaks. The spectrum contains about 10 million counts per bin.

3.2.1. Mobile communication frequencies

However, there are two additional peaks at around 800 MHz and 950 MHz, note that the Fourier transform in figure **3.10** is plotted logarithmically, so these peaks are significantly smaller that the TDC peaks, but still influential enough to affect the $g^{(2)}$ spectrum.

These frequencies turn out to be mobile communication frequencies: There are various mobile telephone masts of Telekom, Telefonica and Vodafone near the university, radiating, inter alia, LTE and GSM09 [35]. While LTE has a frequency band at about 800 MHz GSM provides frequencies of $935 - 960$ MHz, among others [36]. The frequencies match with the measured ones. They periodically raise the baseline of the signal which lead to a periodical enhanced probability of "detecting" an event. In this way the mobile communication frequencies can influence the $g^{(2)}$ spectrum.

To get rid of them two improvements to the set-up were performed: At first the whole electronics, including the PMTs, were shielded by copper films and galvanized copper which can be seen at the right PMT in figure **2.2**. This is a very effective way of suppressing the frequencies at 800 MHz, however, the higher ones still enter the system. Therefore an other element is implemented into the electronics: A low-pass filter (XLF-42M+) seen in figure **3.12**. With its cut-off frequency at about 350 MHz [37] the high-frequency oscillations can be suppressed successfully while the slow photon pulses can pass the filter.

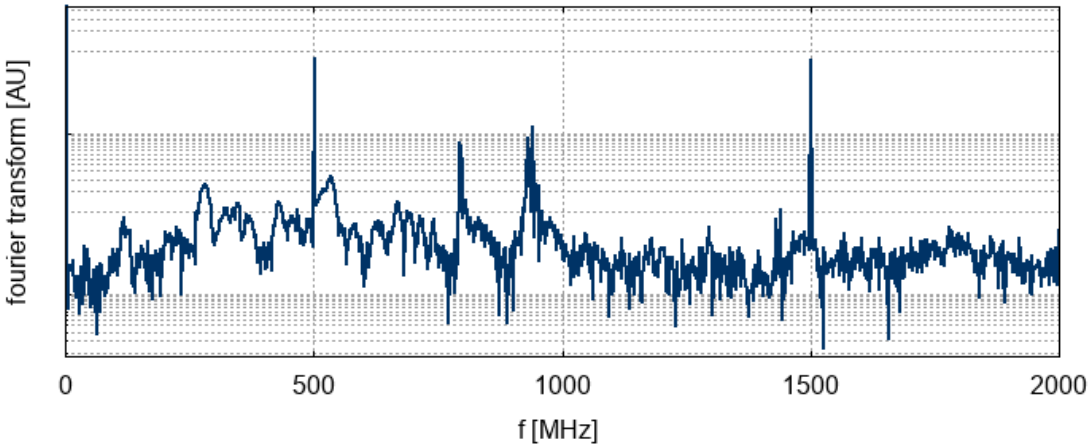

Figure 3.10.: The fourier transform (displayed logarithmically) reveals the TDC-nonlinearity at 500 MHz and 1500 MHz dominating the spectrum, however, mobile communication frequencies at about 800 MHz and 950 MHz influence the shape of the $g^{(2)}$ function as well.

3.2.2. TDC nonlinearity

The remaining frequencies in the Fourier spectrum are the two sharp peaks at 500 MHz and 1500 MHz which lead to the strong oscillation in the $g^{(2)}$ function. The origin of this oscillation can be found when looking at an other observable: the distribution of the TDC time tags. Here not the time differences of events are of interest, but the absolute time tags observed in each channel. When running a 30 min measurement with a rate of 5 MHz on one channel, there are $5\,\text{MHz} \cdot 30\,\text{min} = 9 \cdot 10^9$ time tags distributing on the eight different time bins of the TDC.

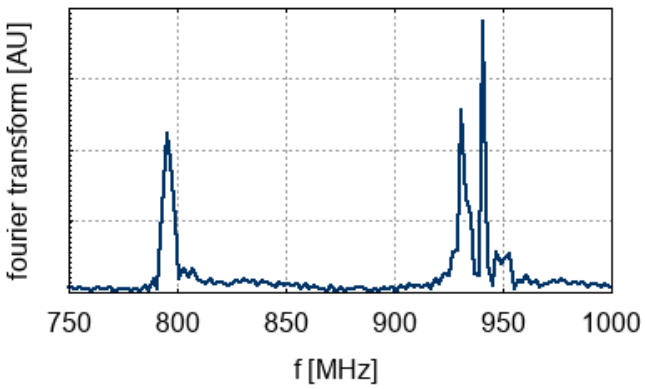

Figure 3.11: Detailed look into the Fourier transform (linear axes) in the region of mobile communication frequencies

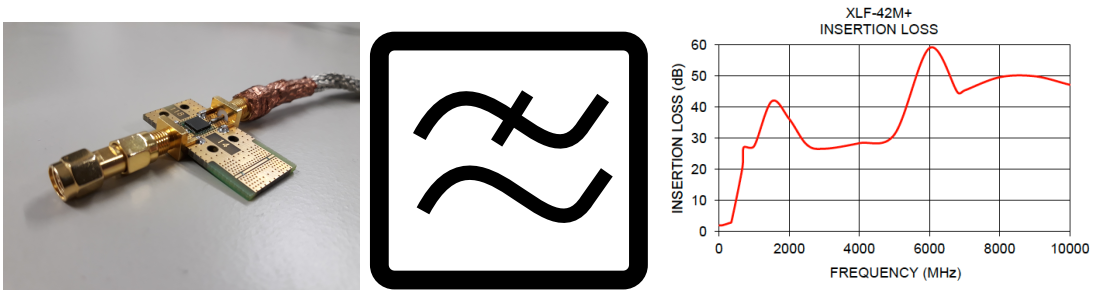

Figure 3.12.: The low-pass filter, its illustration and its spectum. Latter is taken from [37]

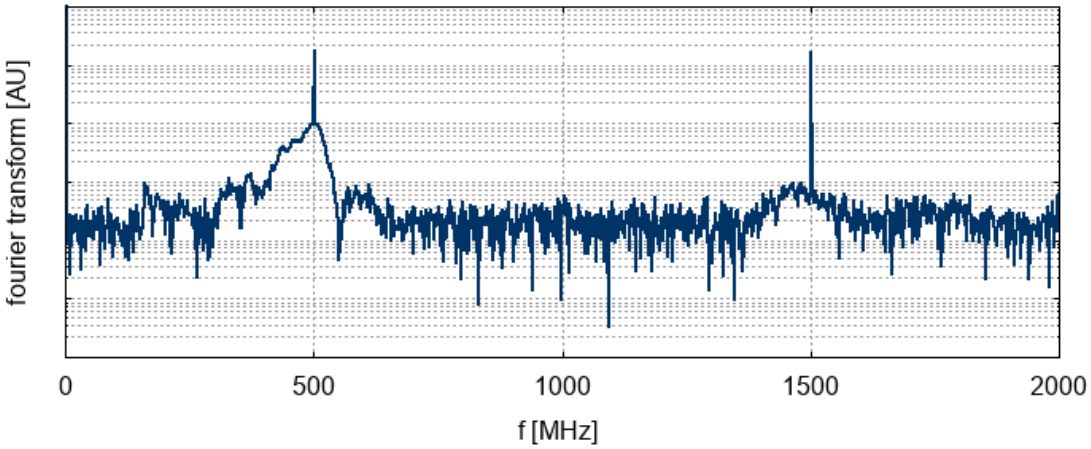

Figure 3.13.: After shielding and installing low-pass filters mobile communication influences could be eliminated. The TDC-nonlinearity effects remain.

Even if one expects correlation signals in the $g^{(2)}$ function, the distribution over the eight TDC bins should be uniform as correlations average out on long measurements. Imagine for example a photon correlation that leads to an accumulating occurrence of signals in consecutive bins, then one of these couples may lie in bins 2 and 3, the next one in 0 and 1 or in 7 and 0 and so on. On average, all TDC bins should contain almost the same number of counts (differing only by statistics).

Figure 3.14 checks this by presenting the counts cumulated in the TDC time bins both of channel 0 and 1 during the whole measurement.

It is obvious that the distribution is not uniform at all in both channels. While there are significant less counts in bin 0, bin 4 contains an excess compared to the average. Bins 0 and 4 actually differ by more than a factor of 2.

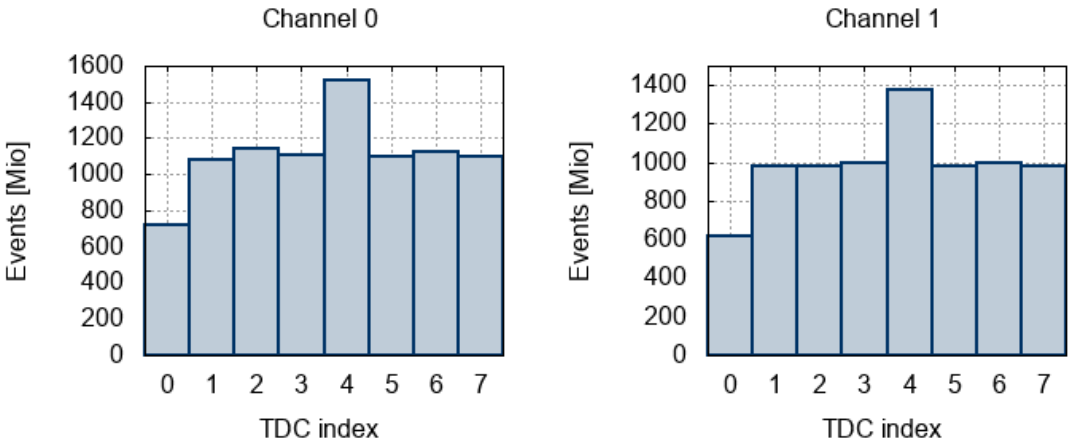

Figure 3.14.: The time stamp histograms of channel 0 and channel 1 demonstrate the TDC-nonlinearity

That means that the TDC bins do not have the same "sizes", but bin 4 has about twice the size of bin 0, so that the probability of recognizing an event in bin 4 is two times the one for bin 0. This asymmetry is called TDC-nonlinearity.
Is it possible to deduce the oscillations in the $g^{(2)}$ spectrum from this nonlinearity? For this purpose assume an uncorrelated light measurement where one expects a 1 everywhere in the ideal $g^{(2)}$ spectrum. Now think about the effect of TDC-nonlinearity. As bin 4 appears above-average often, time differences *from* or *to* bin 4 appear more often in the time difference/$g^{(2)}$ histogram, whereas time differences with bin 0 involved appear less often.
However, for each possible time difference all bins are involved. For instance, time difference 3 (which refers to $\tau = 750\,\text{ps} + N \cdot 2\,\text{ns}, N \in \mathbb{Z}$) is the difference between bins 3 and 0, but also between 4 and 1, between 5 and 2 and so on. A comparable number for each time difference j is C_j, as introduced now:

$$C_j = \sum_{i=0}^{7} TDC_{i,\text{ channel 0}} \cdot TDC_{(i+j) \mod 8,\text{ channel 1}} \tag{3.4}$$

This parameter goes over each TDC bin and multiplies the bin content with the one that is the difference j away. Since the 0-1-cross correlation spectrum is observed here, the bins of channel 0 must be compared to the ones of channel 1, but the same procedure could be executed for any of the four correlation histograms. This can be done for all 8 differences $0 - 7$[2], the resulting C_j can be normalized to

[2]Difference 8 which is $\tau = 2\,\text{ns}$ is the same as difference 0 or 16 or 24,..., as all 2 ns the probability pattern shown in figure 3.14 repeats . This is the reason for the modulo operation.

compare them with the measured $g^{(2)}$ function. The comparison is shown in figure 3.15. The computed normalized C_j are plotted as bars, as visible on the "difference index" axis this pattern repeats every eight bins.

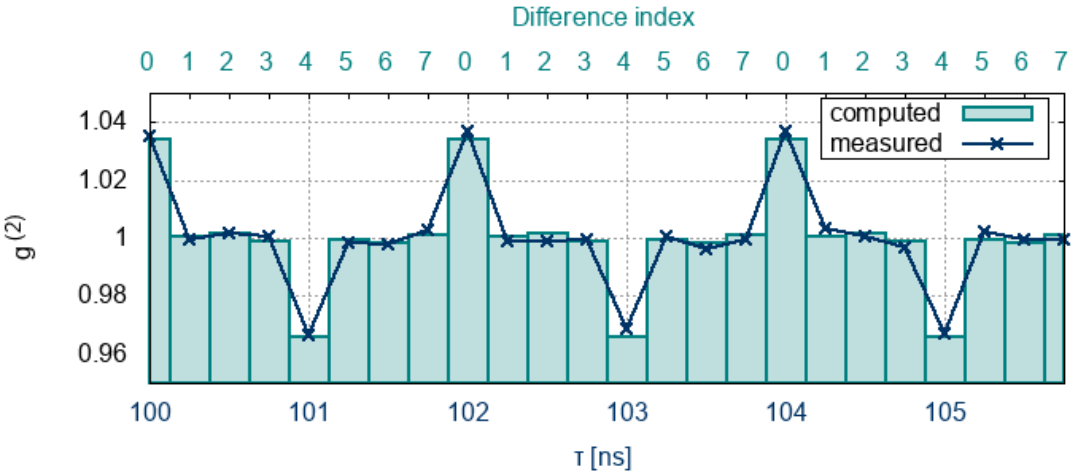

Figure 3.15.: Comparison of the computed $g^{(2)}$ pattern with the measurement in an arbitrary time range. The computed bars are the normalized C_j values, repeating every eight bins.

The measured values are plotted in the range from 100 to 106 ns. This is an arbitrary range, one could chose any range, just make sure to shift the time difference pattern to the correct position (time difference $\tau = 0$ is also time difference index 0). The reason why figure 3.15 does not show time differences around $\tau = 0$ is that there are some additional disturbances around the zero-region, these will survive a calibration as seen later.
The comparison shows that the TDC-nonlinearity explains the observed $g^{(2)}$ pattern very well, this proves the remaining frequencies at 500 and 1500 MHz originate from the TDC. Nevertheless this effect has to be calibrated out to see significant correlation signals, the different methods used are described in the following section.

3.2.3. Calibrating the nonlinearity

Two different methods are used to calibrate the measurement for eliminating the TDC-nonlinearity. One requires a reference measurement with a non-correlated light, the other deals with the fact that even in a $g^{(2)}$ spectrum where bunching is expected there are uncorrelated regimes in the outer regions of the spectrum where $|\tau| \gg 0$.

Calibration with non-correlated light

The method of using a reference measurement run works as follows: A $g^{(2)}$ measurement with a conscious uncorrelated light source is executed to receive only the systematics of the electronics. Total uncorrelated light should produce a perfect 1 everywhere in the $g^{(2)}$ spectrum, the actual spectrum can be seen as a response function of the system. Especially the nonlinearity of the TDC contributes to the shape of the response function. After doing the measurement one can use this $g^{(2)}$ pattern as a calibration pattern, such a measurement will be called "calibration measurement". The resulting $g^{(2)}$ function can be pinned to 1 by dividing each bin by the reference bin in the calibration measurement (when calibrating the calibration measurement itself this is trivial since each bin is divided by its own value, this would lead to a mathematical perfect 1). When taking a measurement with a correlated light source, a so called "correlated measurement", the same procedure can be done again. Expectation is now, that the uncorrelated regime will become 1 when dividing by the calibration bins, only in the correlation region around $\tau = 0$ some divergence will remain, namely $g^{(2)} > 1$, if a bunching signal is expected (and e.g. $g^{(2)} < 1$ for an anti-bunching measurement). This signal remains as it differs from the calibration measurement and will not be calibrated out. In other words, a bunching signal in a bin raises the bin in the correlation measurement additional to some disturbances, in the reference measurement this bin is only influenced by disturbance. Calibration only eliminates the disturbance, the bunching signal survives.

Instead of dividing each measurement bin in the $g^{(2)}$ function by the corresponding calibration bin value, one also could subtract it, this should eliminate the TDC-nonlinearity as well.

What light sources can be used for such a calibration? Of course any that do not produce a bunching signal. Avoiding correlations is actually quite easy. One can take a light source that does not produce bunching at all, like a laser, for the reference measurement. However, even thermal/chaotic light sources can be used when not fulfilling coherence conditions. For this calibration, sunlight is used. Even though the sun is a thermal light source, a possible correlation signal can be avoided by not filtering a specific wavelength but detecting the whole sun spectrum. Furthermore the sunlight is not lead through a small slit but enters the lab through the door that is far too big to create a macroscopic coherence cell.

Using sunlight instead of laser light simplifies the measurement procedure as there is no need to install a laser first for the calibration measurement and removing it later for the correlation measurement again.

Figure **3.16** shows the result of two measurements: A 7 hr measurement of unfiltered sunlight with average rates of $\dot{N}_0 = 2.6\,\mathrm{MHz}$ and $\dot{N}_1 = 3.8\,\mathrm{MHz}$ that will be used for calibration, and a 7 hr measurement of a LED filtered to 1 nm with rates of

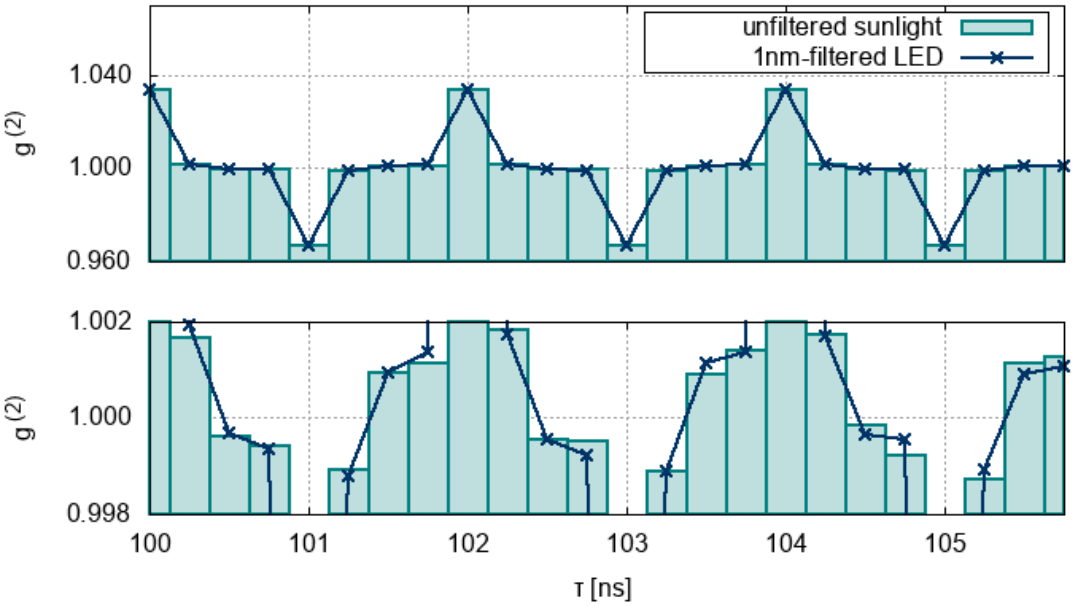

Figure 3.16.: The calibration run (unfiltered sunlight) and the "correlation" measurement (filtered LED) cannot be distinguished in the upper plot, as they look too similar. One has to zoom in to see the differences (below).

4.8 MHz and 3.3 MHz. This measurement in fact could be used to see bunching effects, however, the statistics is still too small to observe a significant signal that stands out of the remaining disturbances at $\tau = 0$, but it can be used as a test of the calibration method(s). Expectations from the calibration are to obtain a $g^{(2)}$ function that is 1 everywhere, and maybe some very small non-significant correlation peak around zero.

When looking at the $g^{(2)}$ functions of the calibration/reference and the "correlation" measurement in figure **3.17** there is no visible difference. Only after observing it in detail deviations from one curve to the other become apparent. Of course they do not look exactly the same even in a non-correlated regime as statistical fluctuations come into play, nevertheless the calibration via dividing the LED measurement by the sunlight measurement can be executed and is plotted in figure **3.17**.

At first one can look at the scale on the vertical axis: The fluctuations of the calibrated $g^{(2)}$ function is now on the order of $\sigma_{g^{(2)}} < 10^{-4}$. A signal from a mercury lamp line should already be observable, a 1 nm filtered thermal light source requires even higher statistics. In the central region there is still a small signal increase due to some oscillation visible. That means that there is some kind of crosstalk between the channels when two signals arrive (almost) at the same time at the digitization

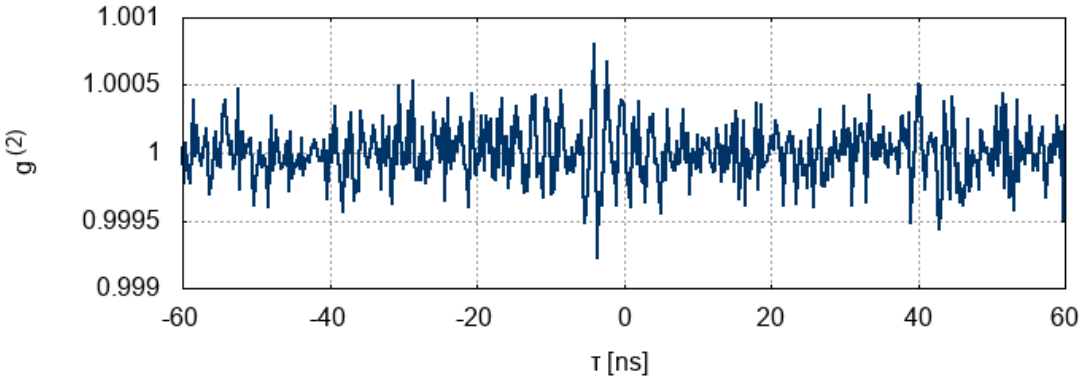

Figure 3.17.: The "correlation" measurement calibrated via division by the calibration run. While there are still some (small) disturbances remaining around zero, the outer regions do not show obvious systematics.

card that is different from measurement to measurement so that it is not calibrated out totally. However, in the outer regions almost only random fluctuations remain.

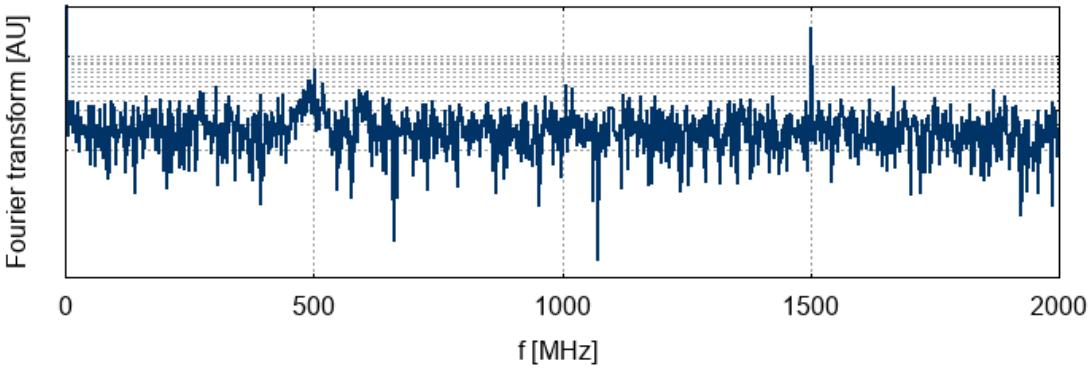

Figure 3.18.: Fourier transform of the calibrated $g^{(2)}$ function. The TDC-nonlinearity is still existent, but attenuated extremely due to calibration.

The Fourier transform in figure **3.18** reveals that the nonlinearity of the TDC is measurable, although it is now reduced drastically by calibration. Since it is not calibrated out fully, the digitization card may not work in the exact same way when doing several measurements (at different times, different temperatures, ...). Nevertheless, the effect is strongly suppressed, one can calculate the RMS from the measurement now for checking consistency with theory.

The RMS in a range from $\tau = 150\,\text{ps}$ to $\tau = 250\,\text{ps}$ for the calibrated $g^{(2)}$ function turns out to be

$$\sigma_{g^{(2)},\,\text{exp}} = 0.175 \cdot 10^{-3} \tag{3.5}$$

This interval is chosen to be far away from $\tau = 0$ to make sure to just look at the random fluctuation region without any disturbances that are still existent in the center region.
For comparison, the expected fluctuations considering the rates and measurement time can be calculated. Note that there are two separate measurements contributing to the final calibrated $g^{(2)}$ function, therefore uncertainties of both must be taken into account. The uncertainties on the separate measurements are σ_{calib} for the calibration measurement and σ_{corr} for the correlation measurement. They can be computed according to section 2.3.1.

$$\sigma_{\text{corr}} = \frac{1}{\sqrt{4.8\,\text{MHz} \cdot 3.3\,\text{MHz} \cdot 250\,\text{ps} \cdot 7\,\text{hr}}} = 1.00 \cdot 10^{-4} \tag{3.6}$$

$$\sigma_{\text{calib}} = \frac{1}{\sqrt{2.6\,\text{MHz} \cdot 3.8\,\text{MHz} \cdot 250\,\text{ps} \cdot 7\,\text{hr}}} = 1.27 \cdot 10^{-4} \tag{3.7}$$

As the calibrated $g^{(2)}$ function is $g^{(2)} = \frac{g^{(2)}_{\text{corr}}}{g^{(2)}_{\text{calib}}}$ the uncertainty can be calculated via error propagation:

$$\sigma_{g^{(2)},\,\text{theo}} = \sqrt{\left(\frac{\partial g^{(2)}}{\partial g^{(2)}_{\text{corr}}}\sigma_{\text{corr}}\right)^2 + \left(\frac{\partial g^{(2)}}{\partial g^{(2)}_{\text{calib}}}\sigma_{\text{calib}}\right)^2} = \sqrt{\frac{{\sigma_{\text{corr}}}^2}{{g^{(2)}_{\text{calib}}}^2} + \frac{{g^{(2)}_{\text{corr}}}^2 {\sigma_{\text{calib}}}^2}{{g^{(2)}_{\text{calib}}}^4}} \tag{3.8}$$

In this equation one can set $g^{(2)}_{\text{corr}} = g^{(2)}_{\text{calib}} \approx 1$ as the functions are normalized and fluctuating around 1. The expression simplifies to

$$\sigma_{g^{(2)},\,\text{theo}} = \sqrt{{\sigma_{\text{corr}}}^2 + {\sigma_{\text{calib}}}^2} = 0.161 \cdot 10^{-3} \tag{3.9}$$

The experimental value from equation 3.5 is therefore only slightly higher than expected from theory. This may originate in the lasting (weak) existence of the nonlinearity.
The described calibration method works quite well, however, it causes some problems. As seen, the $g^{(2)}$ pattern is very sensitive for small differences in the set-up, another temperature, other cables and so on. This requires a calibration run for every new correlation measurement with at least equal measurement times. This effectively causes a factor 2 in time, the fluctuations increase due to division by about a factor $\sqrt{2}$ (if correlation and calibration measurements have the same

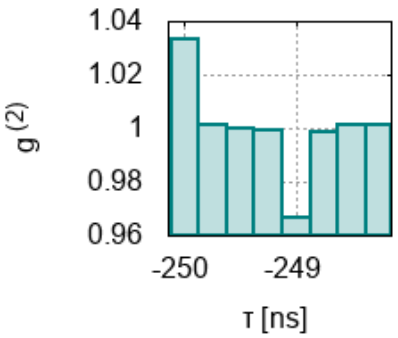

Figure 3.19: The 8-bin template of the outermost part of the evaluated $g^{(2)}$ spectrum can be taken to calibrate the entire spectrum.

statistics), again requiring a longer measurement time to see significant signals. These problems can be solved when using another calibration method.

Calibration using a non-correlated time region

Upper procedure deals with the fact that there is no correlation in the reference spectrum, so that it can be used as a calibration. However, even if one takes a correlation measurement there are regimes in the $g^{(2)}$ function, where no correlation is expected, namely all parts where $\tau \ncong 0$. The TDC-nonlinearity effect repeats every 2 ns, that is 8 bins in the standard spectrum with $\Delta t_{\text{bin}} = 250\,\text{ns}$. This repetition can be used wisely: Only one 8-bin part in a region where $|\tau| \gg 0$ has to be taken to calibrate the **whole** $g^{(2)}$ function.
Usually the $g^{(2)}$ function is evaluated in the regime $\tau \in [-250\,\text{ns} : 250\,\text{ns}]$, so to be absolutely safe the first 8 bins from -250 ns to -248 ns far far away from the center where correlations and disturbances appear are taken for the calibration pattern. Thus this method is called "tail calibration". When having the template every bin in the spectrum has to be divided by the corresponding calibration bin of the template, that is, the ninth bin by the first template bin, the tenth bin by the second template bin,... . Every eight bins the template repeats.
As a consequence there is no need to take an extra calibration measurement, one saves a factor of 2 in measuring time. Furthermore it is ensured that the measurement conditions of the correlation and the calibration are identical, even the statistics are equal which simplifies uncertainty estimation.
However, this procedure can be optimized further. When dividing each bin by the corresponding calibration bin there is still an increase of the statistical fluctuations by a factor of $\sqrt{2}$ compared to a system that has no need for calibration, since both dividend and divisor contain uncertainties (which should be equal when the statistics are the same).

$$\sigma_{g^{(2)},\,\text{theo}} = \sqrt{{\sigma_{\text{corr}}}^2 + {\sigma_{\text{calib}}}^2} = \sqrt{{\sigma_{\text{corr}}}^2 + {\sigma_{\text{corr}}}^2} = \sigma_{\text{corr}} \cdot \sqrt{2} \tag{3.10}$$

Latter uncertainties (σ_{calib}) can now be decreased by adding statistics, figure **3.20** explains how it works. Now not only one 8-bin pattern is used to create the calibration template, but it is averaged over many in the tail of the $g^{(2)}$ spectrum.

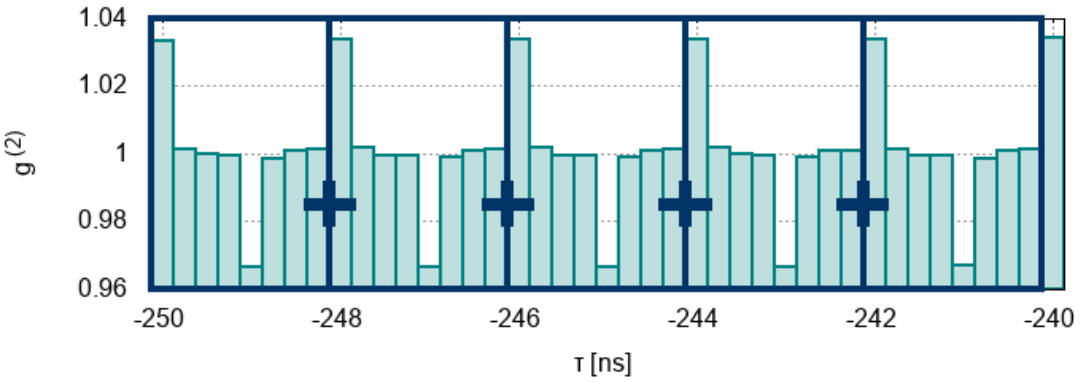

Figure 3.20.: Improved calibration method: 8-bin patterns in the non-correlation-region are superimposed to create a high-statistics calibration template.

Usually 63 8-bin patterns are used, which refers to a range of $63 \cdot 2\,\text{ns} = 126\,\text{ns}$ and therefore the region $[-250\,\text{ns} : -124\,\text{ns}]$ is used for creating the calibration template. Here it is necessary to find a compromise between a calibration range as big as possible to gather statistics and the danger of running into disturbances in the central region of the $g^{(2)}$ spectrum. Especially when changing the set-up e.g. by adding other cables or extra elements it has to be ensured that the the calibration range does not contain disturbances that influence the calibration pattern and falsify the calibration.
When taking 63 patterns, the statistics increases by this factor, the uncertainties of the template decrease by a factor of $\sqrt{63} = 7.93$. Thus the calibration does not increase the fluctuations by a factor of $\sqrt{2} = 1.414$ but only by

$$\frac{\sigma_{g^{(2)},\,\text{theo}}}{\sigma_{\text{corr}}} = \frac{\sqrt{{\sigma_{\text{corr}}}^2 + {\sigma_{\text{calib}}}^2}}{\sigma_{\text{corr}}} = \frac{\sqrt{{\sigma_{\text{corr}}}^2 + \frac{1}{\sqrt{63}^2} \cdot {\sigma_{\text{corr}}}^2}}{\sigma_{\text{corr}}} = \sqrt{1 + \frac{1}{63}} = 1.008 \tag{3.11}$$

Using this method the increase of uncertainties due to the calibration procedure is actually negligible. When trying to measure a correlation signal with a certain significance this method **again** reduces the required measurement time by another factor of 2.
Figure **3.21** shows the result of such a calibration on the LED measurement already observed in the upper section.

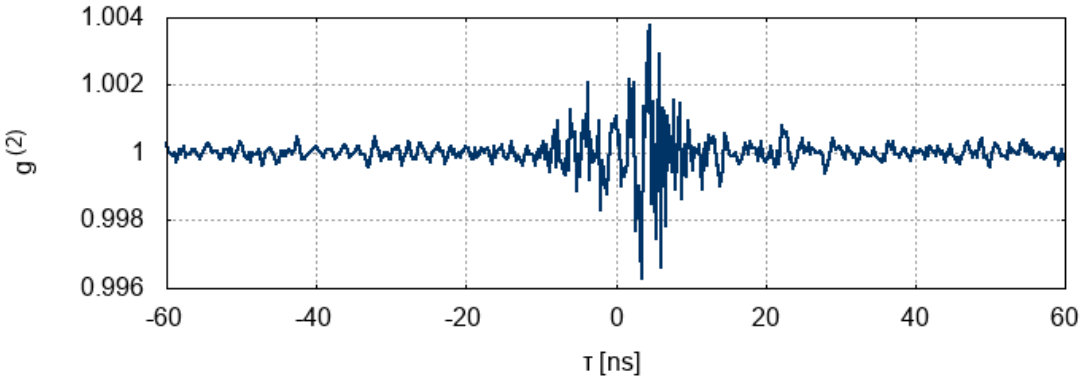

Figure 3.21.: The TDC nonlinearity could be eliminated by the new calibration method as well, the fluctuations decrease in the outer regions. In contrast, disturbances in the central region increase.

At first sight one recognizes that the disturbances in the center region increased compared to the calibration with the reference measurement. Whereas the reference calibration method includes these fluctuations around $\tau = 0$ the tail calibration does not, hence this is not surprising. So there might be a disadvantage using the new tail calibration method when looking for signals at $\tau = 0$.
However, let's take a look at the outer regions. While the theoretical RMS (equation **3.6**) is $0.10 \cdot 10^{-3}$ ($\cdot 1.008$), the actual RMS in the range $[150\,\text{ns} : 250\,\text{ns}]$ turns out to be

$$\sigma_{g^{(2)},\,\text{exp}} = 0.11 \cdot 10^{-3} \tag{3.12}$$

which matches expectations excellently. That means there are no systematics left in the tail region, recognizing a hypothetical signal in the outer parts with a requested significance is now only influenced by statistics following section 2.3.
Additionally this method does not require normalization before calibration. The 8-bin template can also be made of absolute event numbers[3]. Thus calibration and normalization is done in one step.
However, the disturbances in the center region still cause problems when trying to see a signal. A solution may be to shift the signal region out of the center of the $g^{(2)}$ function. This is possible by adding a delay within the electronics of one channel. It is done by replacing the cable running from the amplifier to the digitization card in *one* of the channels. In this way a correlated signal at the PMT gets delayed in one of the channels, by choosing a specific cable delay any point on the τ-axis

[3] When taking several 8-bin patterns for the calibration template one has to divide each bin in the resulting pattern by the number of 8-bin patterns, so in general 63

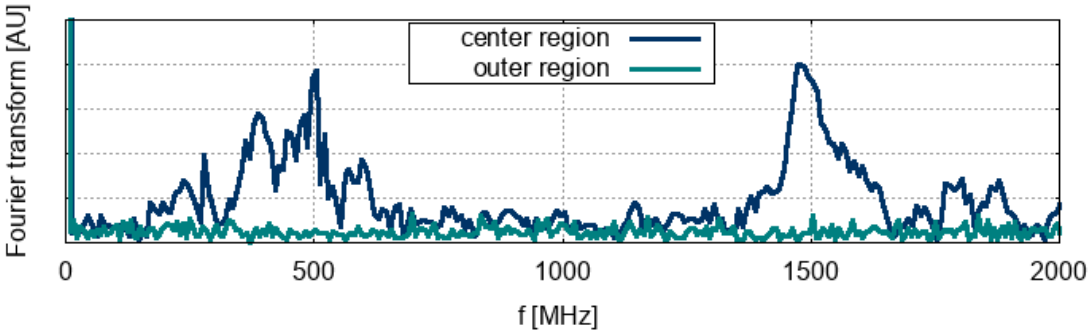

Figure 3.22.: Linear plot of the Fourier transform using the tail calibration method: in the center region (here: $[-60\,\text{ns} : 60\,\text{ns}]$) there still exist frequencies matching to the TDC-nonlinearity, in the outer regions ($[100\,\text{ns} : 250\,\text{ns}]$) they do not.

can be selected for the signal region. This is also a possibility of analyzing the disturbances. When they move with the delay, the emerge before the delay (near or at the PMTs), when they remain at $\tau = 0$ they are cross talk effects in the digitization card.
A test of the delay can be executed with a pulsed laser.

3.3. Setup characterization using a pulsed laser

A pulsed laser is a very useful tool to characterize the setup. A short laser pulse (FWHM $\approx$ 40 ps [38]) enters the beamsplitter and the PMTs. It simulates a coincidence signal, but with a way bigger signal rate. When adjusting the pulse frequency to some MHz there are at least one million coincidence events and basically no background. When implementing a delay the coincidence peak gets shifted in the $g^{(2)}$ spectrum and reveals the actual position where to look for the later correlation signal of thermal light sources. In addition the electronic time resolution of the whole system can be determined by measuring the width of the coincidence peak.
The measured coincidence peak is shown in figure **3.23**. The measurement is exactly the same like measuring the $g^{(2)}$ functions, however, here it is not useful to speak in terms of $g^{(2)}$ but show absolute coincidence event numbers, since normalization would fail as no tail events are expected except from background noise, however, it can be seen in the figure that the background rate is quite low. When looking at the resulting spectrum in a bigger range, other peaks of the same strength exist beside the one shown here, since the laser pulse frequency is high enough to produce coincidence peaks of photons of one laser pulse to photons of the next one (and

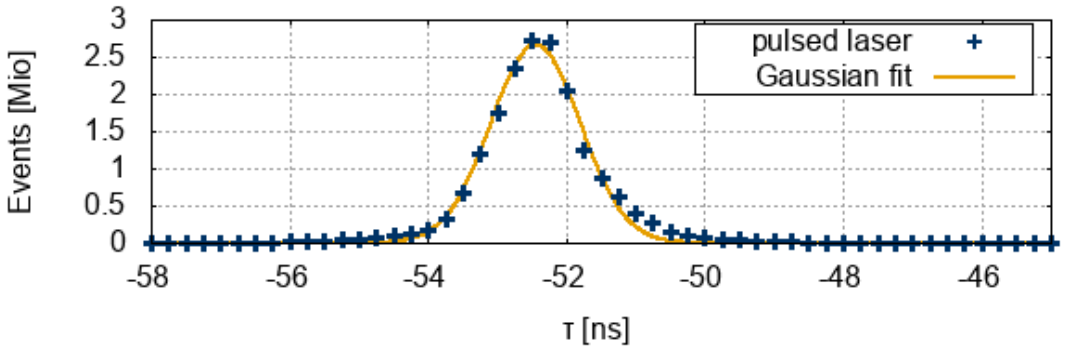

Figure 3.23.: The coincidence peak of the pulsed laser reveals the cable delay and the time resolution of the system.

even further ones, depending on the laser frequency). Hence it is important to ensure that the observed peak is the real "zero"-peak.
A Gaussian fit is added to the spectrum that reveals the desired information.

$$g(x) = A \cdot e^{-\frac{(x-\mu)^2}{2\sigma^2}} \tag{3.13}$$

The mean μ refers to the cable delay, the standard deviation σ can be interpreted as time resolution. Actually the resulting broadening of the peak is a convolution of the electronic time resolution and the pulse width of the laser which is negligible here. Delay and time resolution turn out to be

$$\mu = (-52.44 \pm 0.01)\,\text{ns} \tag{3.14}$$

$$\sigma = (645 \pm 8)\,\text{ps} \tag{3.15}$$

The fact that the mean is negative is an outcome of the arbitrary choice of the channel the delay cable is implemented. Here it is built into channel 0, thus the channel 0-signal gets delayed by about 52 ns and arrives later, or from the other perspective, the channel 1-signal arrives 52 ns earlier which causes a coincidence at -52 ns in the $0-1$ histogram which is always observed.
The σ is of special interest here as it should not be influenced by the cable delay but resemble the time resolution of the whole system (PMTs + amplifiers + band-pass filters + all cables + digitization card) that should not change (much) when the setup is changed slightly. In section 2.1.1 the time resolution of the PMTs was already discussed qualitatively, now there is an additional element impairing the resolution, the digitization card.

The measurement with the pulsed laser can be used to check the later bunching measurements for consistency since the resulting correlation peaks should contain the same time resolution.

4. Intensity interferometry of thermal light sources

As the fluctuations of the $g^{(2)}$ function after calibration match the statistical expectations at least at the level of 10^{-4}, one can move on to measuring photon bunching effects of real thermal/chaotic light sources. A mercury lamp with a line width of only some picometers and therefore a rather big correlation time[1] will be investigated. The signal is strong enough to perform some system tests with it, measurement times of $T \lesssim 1\,\mathrm{hr}$ are sufficient to see a significant signal.
Whereas the measurements with the mercury lamp make use of the natural linewidth of the light source, a LED can be used to measure a broad-bandwidth source. Here the light must be actively filtered to achieve a measurable signal using a 1 nm interference filter. This measurement is a practical test simulating intensity interferometry with a stellar source in the laboratory.

Contents

4.1. Setup for bunching measurements

In this section the setup used for temporal intensity interferometry of thermal light sources is described. The general setup holds for both sources the mercury lamp and the LED. Specific details are mentioned in the corresponding sections. Figure 4.1 shows a schematic of the setup, figure 4.2 two photos.

[1] Note that even the mercury lamp has a correlation time of only a few picoseconds

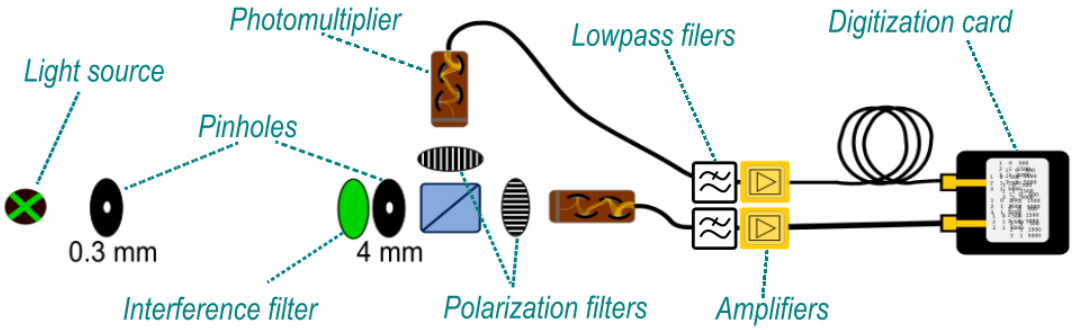

Figure 4.1.: The setup for the bunching measurements

The light source will be either the mercury lamp or the LED, the emitted light passes a circular pinhole with a diameter of $D_\mathrm{p} = 300\,\mu\mathrm{m}$. The pinhole is needed to keep the effective light source small and thus the coherence cell macroscopic. Between the light source and the first pinhole several optical lenses are installed (not shown in the figure) in order to generate the maximal possible photon rate at the PMTs.
Nevertheless the coherence cell is still quite small so that even PMTs placed right next to each other exceed the size. Hence, a beamsplitter is added in the beam to allow an arrangement of the PMTs at the same optical position and an effective separation distance of 0. Finally, to ensure measuring within one coherence cell a second pinhole is installed in front of the beamsplitter with a diameter of $d_\mathrm{P} = 4\,\mathrm{mm}$. The distance between the pinholes are $L_\mathrm{Hg} = 3.46\,\mathrm{m}$ and $L_\mathrm{LED} = 3.39\,\mathrm{m}$. Hence the sizes G_i of the coherence cell (from minimum to minimum, see section 1.2.3) are

$$G_\mathrm{Hg} = 2 \cdot 1.22 \cdot \frac{L_\mathrm{Hg}}{D_\mathrm{p}} \cdot \lambda_\mathrm{Hg} = 2 \cdot 1.22 \cdot \frac{3.46\,\mathrm{m}}{300\,\mu\mathrm{m}} \cdot 546\,\mathrm{nm} = 15.4\,\mathrm{mm} \tag{4.1}$$

$$G_\mathrm{LED} = 2 \cdot 1.22 \cdot \frac{L_\mathrm{LED}}{D_\mathrm{p}} \cdot \lambda_\mathrm{LED} = 2 \cdot 1.22 \cdot \frac{3.38\,\mathrm{m}}{300\,\mu\mathrm{m}} \cdot 532\,\mathrm{nm} = 14.7\,\mathrm{mm} \tag{4.2}$$

The coherence cell is therefore bigger than the pinhole, however, there are always spatial coherence losses when the transmission area of the pinhole is extent. Figure 4.3 shows the dimensions of the spatial coherence loss. Here the $g^{(2)}$ function for the LED setup (and in a good approximation for the Hg lamp setup as well) is drawn, also is the pinhole region from $d = 0\,\mathrm{mm}$ to $d = 4\,\mathrm{mm}$[2]. While one may

[2]Remember that the $g^{(2)}$ function is not a static function in the observation plane like the diffraction pattern but a function depending on the distance between two "detectors"

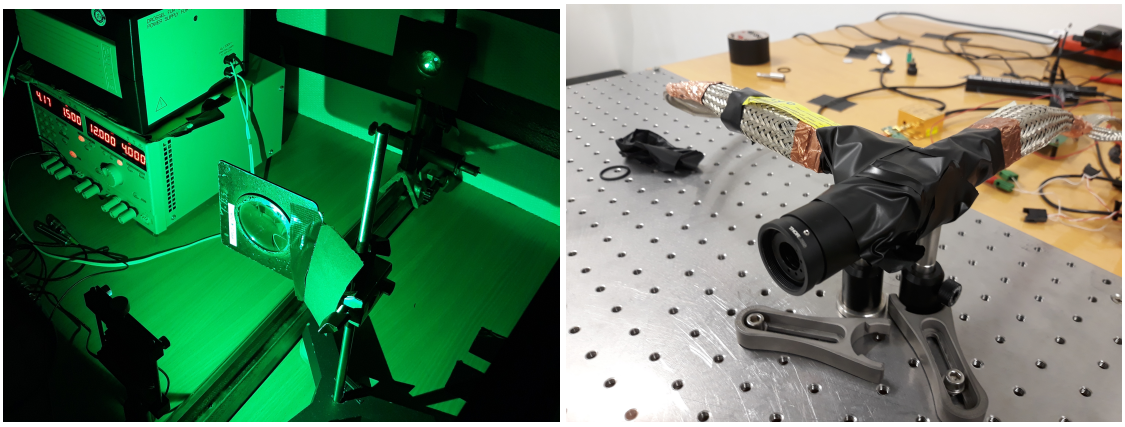

Figure 4.2.: Photos of the setup. On the left: The LED "in action" is mounted in the corner down on the left. The light is focused by some optical lenses onto the 300 µm-pinhole which is embedded in the polystyrene wall. Right: The detection setup: The interference filter, the 4 mm-pinhole, the beamsplitter and the polarization filters are completely covered in the black tube system.

assume the $g^{(2)}$ function to be 2 in the whole area there are possible distances where $g^{(2)}(d)$ is significantly below 2.

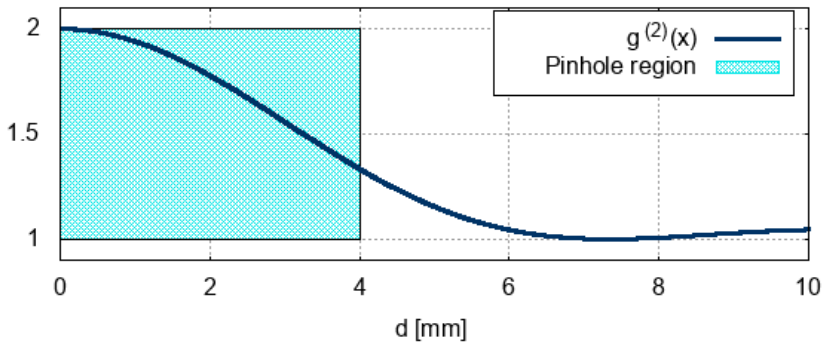

Figure 4.3.: Spatial loss due to the extent of the pinhole

Using the parameters from the experiment the reduction factor can be computed numerically using a Monte-Carlo simulation with equally distributed photon pairs within the circular pinhole which is done by Peter Deiml and Adrian Zink.

The resulting loss factor turns out to be 77% which means the signal is expected to be 23% weaker than in the ideal case which could only be achieved when the entrance pinhole area converges towards zero. However, an infinitesimal small

pinhole would lead to a vanishing photon counting rate, thus a compromise had to be found.
To obtain a measurable signal an interference filter is placed within the tube before the beamsplitter. For the LED this is indispensable as the broad spectrum of an unfiltered LED would not allow to see a signal at all. For the Hg lamp the filter is used to eliminate all emission lines which lower the contrast of the signal (since each emission line creates bunching but acts as background for the other lines) except one.
After the light is separated by the beamsplitter it enters a polarization filter on each way to the PMTs. The reason for implementing the filters is to prove that a measured signal is a bunching signal and not some systematic cross talk between the channels. The filters can be oriented such that the transmitted polarization is the same ("parallel orientation") or twisted by 90° against each other to obtain orthogonal polarization ("perpendicular orientation"). Since the intensity of the electromagnetic field in case of orthogonal polarization of two light beams is independent of relative phases no diffraction patterns exist and hence no photon correlations are expected. While in the first case the photon correlation signal should be maximal, in the latter case no enhancement at $g^{(2)}(\tau = 0)$ should be measured.
The signals from the PMTs pass low-pass filters to eliminate mobile communication frequencies and get amplified before entering the digitization card. One of the channels gets delayed by $\approx 52\,\text{ns}$ for the Hg lamp and $\approx 61\,\text{ns}$ for the LED to shift the real zero out of the center region in the $g^{(2)}$ spectrum where crosstalk disturbances occur.

4.2. A narrow-bandwidth source: The mercury lamp

4.2.1. Physics of the mercury lamp

A mercury (Hg) lamp is a gas discharge lamp filled with mercury gas inside a tube. When a voltage is applied between the ends of the tube electrons are passing the gas colliding with the gas atoms and exciting them by raising electrons of the atoms into high energy orbitals. When they deexcite they emit photons of the deexcitation energy ΔE. [39]
These photons have in principle very well defined wavelengths of $\lambda = \frac{hc}{\Delta E}$ only line broadened by the life time of the radiation state according to Heisenberg's uncertainty principle. However, when the atoms are in a gas they collide with other atoms which can lead to an early deexcitation resulting in a broader line width depending on the pressure. [40]

The spectrum of a collision/pressure broadened source is Lorentz-shaped of the form [41]

$$F(\omega) = \frac{\gamma}{\pi} \cdot \frac{2}{(\omega - \omega_0 - \beta)^2 + \gamma^2} \tag{4.3}$$

where γ is a damping constant and β the shift in angular frequency which may be neglected. Defining $\tau_c = \frac{1}{\gamma}$ one can write the power spectrum as

$$F(\omega) = \frac{1}{\pi\tau_c} \cdot \frac{1}{(\omega - \omega_0)^2 + (1/\tau_c)^2} \tag{4.4}$$

Applying the Wiener-Khinchine theorem the first-order correlation function has an exponential decrease in $|\tau|$ [13].

Since different excitation levels are possible different lines can be observed. A typical spectrum can be seen in figure 4.4. Very dominant is the 546 nm line which also is in the range where the used PMTs have a high quantum efficiency, hence this line is chosen for measurement. To avoid influences of other emission lines an interference filter with a FWHM of about 10 nm is installed to filter out other lines, the actual line width of the 546 nm-line is orders of magnitude below.

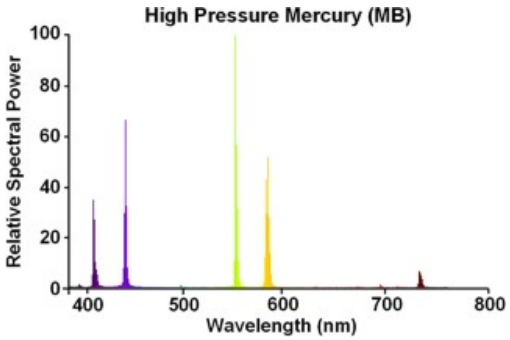

Figure 4.4.: Spectrum of a mercury lamp. Taken from [42]

The measure of $\Delta\lambda$ is not easy for the mercury lamp, since common spectrometers fail to provide a wavelength resolution that makes such a measurement possible. Therefore a special spectrometer from the Max-Planck institute in Erlangen was taken. Figure 4.5 shows the results of this measurement: The mercury lamp curve looks Gaussian, hence it can be fitted and its σ or FWHM could be assumed to be the linewidth. However, the actual line width is folded with the wavelength resolution of the system which has to be known first. Therefore a calibration has to be done using a source with a very small width, namely a special low-pressure mercury calibration source.
The broadening of the mercury lamp line compared to the calibration line yields the actual line width of the Hg lamp σ_{Hg}. Since

$$\sigma_{\mathrm{calib}}{}^2 + \sigma_{\mathrm{Hg}}{}^2 = \sigma_{\mathrm{total}}{}^2 \tag{4.5}$$

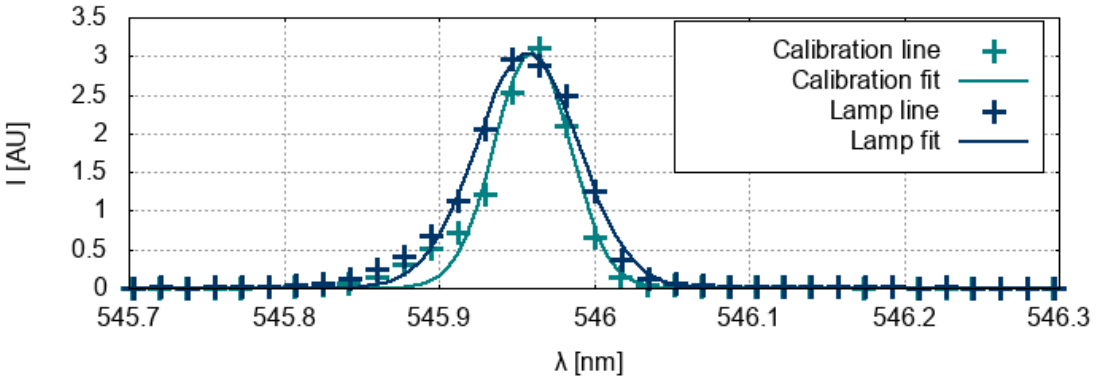

Figure 4.5.: The wavelength spectra of a calibration line and the mercury lamp line with corresponding Gaussian fits. The difference of the lines reveal the actual line width of the mercury lamp.

σ_{Hg} can be calculated from the fit parameters of calibration and total Hg line width that are $\sigma_{\mathrm{calib}} = (24.5 \pm 0.7)\,\mathrm{pm}$ and $\sigma_{\mathrm{total}} = (33.0 \pm 0.6)\,\mathrm{pm}$. One obtains

$$\sigma_{\mathrm{Hg}} = (22.1 \pm 1.1)\,\mathrm{pm} \Rightarrow \Delta\lambda \approx 2.3548 \cdot \sigma_{\mathrm{Hg}} = (52.0 \pm 2.6)\,\mathrm{pm} \tag{4.6}$$

when $\Delta\lambda$ is defined as FWHM. However, since the linewidth of the mercury lamp seems to be very close to the spectrometer resolution or even smaller the measurement may not be reliable, since furthermore the actual linewidth of the calibration line is not known and the calibration of the spectrometer itself had to make use of different calibration lines in different wavelength regimes. However, it can act as an order-of-magnitude estimation to see that the linewidth is on picometer scale.

4.2.2. Correlation signal

The measurement times of both the measurements with parallel and perpendicular orientated polarization filters are $T_{\parallel} = T_{\perp} = 100\,\mathrm{min}$ with rates at $\dot{N}_{0\parallel} = \dot{N}_{0\perp} = 4.2\,\mathrm{MHz}$ and $\dot{N}_{1\parallel} = \dot{N}_{1\perp} = 3.6\,\mathrm{MHz}$. The resulting $g^{(2)}$ functions in the expected correlation region around the "real" zero at $\tau \approx -52\,\mathrm{ns}$ are given in figure 4.6.
The measurement with parallel polfilters shows the expected enhancement due to photon bunching, for the first time a real bunching signal is observed with this electronics. The perpendicular measurement demonstrates the physical nature of the peak. Since it is not visible in this measurement it is guaranteed that the origin of the parallel signal is a bunching correlation signal.

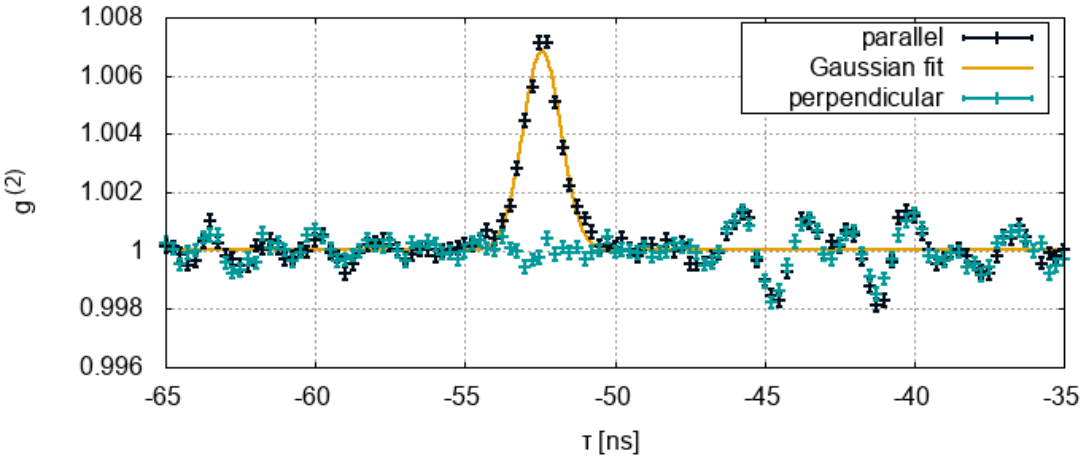

Figure 4.6.: Two measurements with the mercury lamp, one with parallel and one with perpendicular orientated polarization filters

The two measurements are plotted with error bars. These are the theoretical expected uncertainties resulting from the statistics, namely

$$\sigma_{\text{theo}} = \frac{1}{\sqrt{4.2\,\text{MHz} \cdot 3.7\,\text{MHz} \cdot 250\,\text{ps} \cdot 100\,\text{min}}} = 2.1 \cdot 10^{-4} \tag{4.7}$$

Again the experimental RMS in the outer region can be checked, in the region $\tau \in [100\,\text{ns} : 250\,\text{ns}]$ it is $\sigma_{\text{exp}} = 1.9 \cdot 10^{-4}$ which is even slightly below the expected. Beside the existence of the peak it can be seen that there still exist disturbances on both sides of the peak for the parallel as well as for the perpendicular measurement. These are moving with the cable delay and are therefore disturbances that arise *before* the cable, thus maybe some crosstalks between the PMTs. The height of these signals is not influencing the bunching signal strongly here, but it will when measuring the LED.

Figure 4.7 shows two mercury lamp measurements with parallel polfilters differing by the installed cable delay. Whereas the "short cable" refers to a real zero at $\approx -52\,\text{ns}$ as used in most measurements, the "long cable" has a delay of $\approx -72\,\text{ns}$. Such a measurement is another prove of consistency. The bunching signal moves when the cable is replaced to the new "real" zero just as expected.

Additional information about disturbances can be drawn from this plot: While the small oscillations again move with the peak, there is also some crosstalk remaining at the center region for both measurements. Hence, this crosstalk arises *after* the cable delay and therefore inside of the digitization card. However, these disturbances are

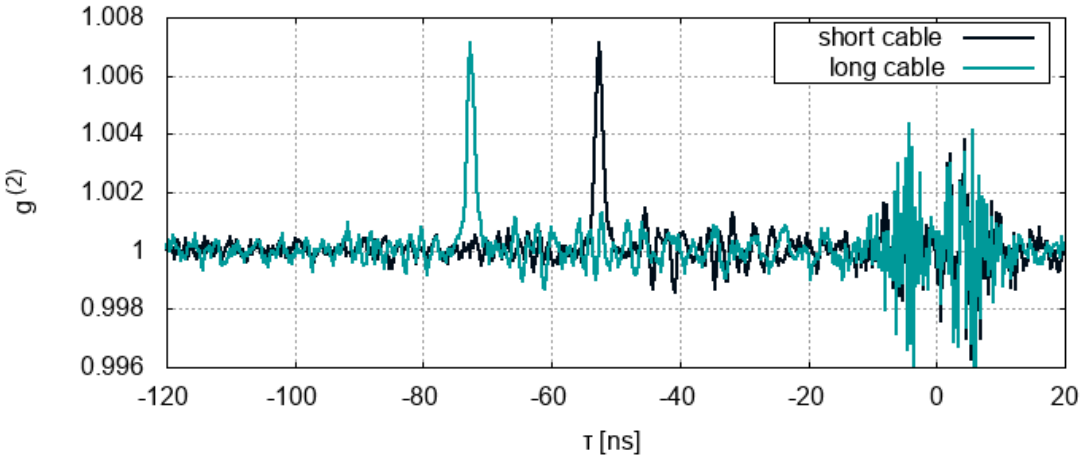

Figure 4.7.: The correlation peak moves when implementing a cable with another delay. In the center region there are still disturbances left.

no problem at all since the signal can be shifted easily out of the central region by installing a cable delay.
When performing quantitative analyses of the bunching signal it is desirable to get rid of any disturbances. A possibility of approaching this goal is to subtract the $g^{(2)}$ function of the perpendicular measurement from the parallel $g^{(2)}$ function. One can guess from figure 4.6 that the oscillations around the bunching peak may vanish. The peak itself should not get affected much by subtraction since there are hardly some deviations from 1 in the perpendicular measurement just in the bunching peak region. The subtraction is done in figure 4.8.
The uncertainty on this plot increases by $\sqrt{2}$ due to subtraction. There are now visible disturbances left in the plot range, thus the signal can be analyzed well. A Gaussian fit of the form

$$g(\tau) = A \cdot e^{-\frac{(\tau-\mu)^2}{2\sigma^2}} + B \tag{4.8}$$

is applied to the data to reveal interesting information:

- The **amplitude** A as indicator for the visibility of the peak. If the quotient of the amplitude and the RMS is high, the signal is well apparent.

$$A = (7.0 \pm 0.2) \cdot 10^{-3} \tag{4.9}$$

- The **medium** μ can be compared to the one from the pulsed laser measurement. Since the used cable delay is the same the center of the peaks should be equal as well.

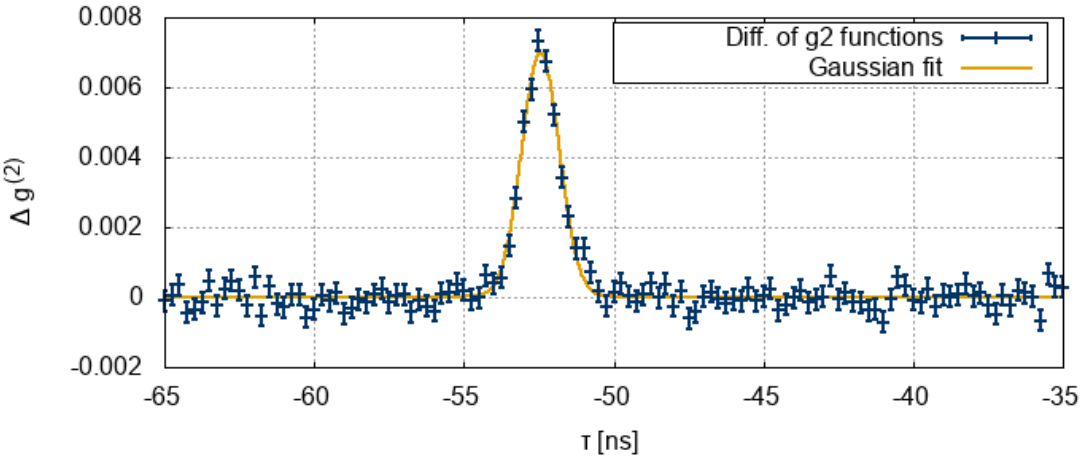

Figure 4.8.: Difference of the parallel and the perpendicular measurement. Systematics vanish on this statistic level.

$$\mu = (-52.44 \pm 0.04)\,\text{ns} \tag{4.10}$$

Both measurements match.

- The **width** σ as time resolution. Again the parameter should fit to the one from the pulsed laser measurement.

$$\sigma = (628 \pm 19)\,\text{ps} \tag{4.11}$$

the time resolution of this measurement is a little bit smaller than from the laser measurement, but still in good agreement considering the uncertainties. Furthermore the time resolution may be influenced slightly by external parameters like temperature or photon rate at the PMTs.

- Finally the **offset** B which is close to zero since both $g^{(2)}$ functions are normalized before subtraction. It would also be defendable to fit without the offset in this measurement.

$$B = (2.0 \pm 3.9) \cdot 10^{-5} \tag{4.12}$$

The significance n of the signal can now be calculated as follows according to section 2.3.2. Remember the equation for n

$$n = \frac{S}{B} = \frac{\tau_c}{\Delta s\sqrt{4\Delta t_{\text{bin}}\sigma}} \tag{4.13}$$

where $\tau_c = \int g(\tau)d\tau = A\sigma\sqrt{2\pi}$ is the correlation time as area under the Gaussian fit curve and Δs is the uncertainty on each bin which should be $\sqrt{2}$ times the uncertainty of the single measurements (parallel or perpendicular) due to subtraction. Inserting the Gaussian parameters for τ_c the equation becomes

$$n = \frac{A\sigma\sqrt{2\pi}}{\Delta s\sqrt{4\Delta t_{\text{bin}}\sigma}} = \underbrace{\sqrt{\frac{\pi}{2\Delta t_{\text{bin}}}}}_{=:K_{\text{bin}}} \cdot \frac{1}{\Delta s} \cdot \underbrace{A\sqrt{\sigma}}_{\text{error-prone}} \tag{4.14}$$

where K_{bin} is a universal constant for any measurement of a defined binwidth Δt_{bin}[3]. The uncertainty on n can be computed taking the uncertainty on the fit parameters into account.

$$\Delta n = \sqrt{\left(\frac{\partial n}{\partial A}\Delta A\right)^2 + \left(\frac{\partial n}{\partial \sigma}\Delta\sigma\right)^2} = \frac{K_{\text{bin}}}{\Delta s}\sqrt{\sigma(\Delta A)^2 + \frac{A^2(\Delta\sigma)^2}{4\sigma}} \tag{4.15}$$

The experimental RMS in $[100\,\text{ns} : 250\,\text{ns}]$ for the $g^{(2)}$-difference is $\Delta s = \sigma_{\text{exp, diff}} = 2.6 \cdot 10^{-4}$, furthermore $K_{250\,\text{ps}} = 79267\frac{1}{\sqrt{s}}$, the significance turns out to be

$$n = 53.5 \pm 1.7 \tag{4.16}$$

The interpretation of the uncertainty on n is quite difficult since n gives already a statement on the reliability of the measurement, so in general the value of n is sufficient to interpret the measurement. It shows that 100 min parallel and perpendicular are absolutely sufficient to measure an extreme significant bunching signal of the mercury lamp.

4.2.3. Theoretical and experimental signal

The obtained signal is absolutely satisfying concerning significance. However, the strength of the signal can be compared to theory to get an impression on the lab conditions. As already discussed the correlation time of the light source can be computed by integrating the signal area in the $g^{(2)}$ histogram.

$$\tau_{\text{c, exp}} = A\sigma\sqrt{2\pi} \Rightarrow \Delta\tau_{\text{c, exp}} = \sqrt{2\pi} \cdot \sqrt{(\sigma\Delta A)^2 + (A\Delta\sigma)^2} \tag{4.17}$$

From the Gaussian fit one gets

[3] The choice of the binwidth Δt_{bin} should not affect the result of n very much, so one would expect the factor to vanish in the equation for n, and in theory it does since $\frac{1}{\Delta s} \propto \sqrt{\Delta t_{\text{bin}}}$

$$\tau_{\text{c, exp}} = (11.02 \pm 0.46)\,\text{ps} \tag{4.18}$$

The theoretical value can be calculated from section 1.2.3 according to the following formula

$$\tau_{\text{c, theo}} = k\frac{\lambda^2}{c\Delta\lambda} \tag{4.19}$$

where $\Delta\lambda$ denotes the linewidth of the source (FWHM) and $k = 1$ for Lorentz-broadened light.
Hence the Signal as area under the $g^{(2)}$ curve including the spatial coherence loss should be

$$S = 0.77 \cdot \tau_{\text{c, theo}} = (14.7 \pm 0.7)\,\text{ps} \tag{4.20}$$

The experimental signal is therefore slightly smaller than expected, however since the measurement of the line width is not very reliable and there may be some losses due to the adjustments of the polarization filters the two results match together quite well.

4.3. A broad source: The light-emitting diode (LED)

The LED is a more challenging light source due to its broad natural bandwidth. This resembles the problems one has to deal with when moving on to stars, active optical filtering is required for a visible bunching signal in a reasonable time at reasonable rates, it is a perfect simulation of stellar intensity interferometry under lab conditions.

4.3.1. Physics of the LED

LEDs are actually normal pn-diodes. p- and n-doped semiconductors are brought together and a depletion region is created. When a voltage in forward direction is applied which means connecting the p-type with the positive terminal and the n-type with the negative terminal the weakly bound electrons in the n-type semiconductor can overcome the small potential barrier formed by the depletion zone charges and enter the p-type semiconductor where they can recombine with holes. [43]
Referring to the band model electrons travel in the conduction band to the p-type region. When recombining with holes they "fall down" by emitting photons which make the LED shine. Since the recombination processes of different electron-hole

pairs can assumed to be independent from each other the LED can be called thermal and photon bunching should be observable.

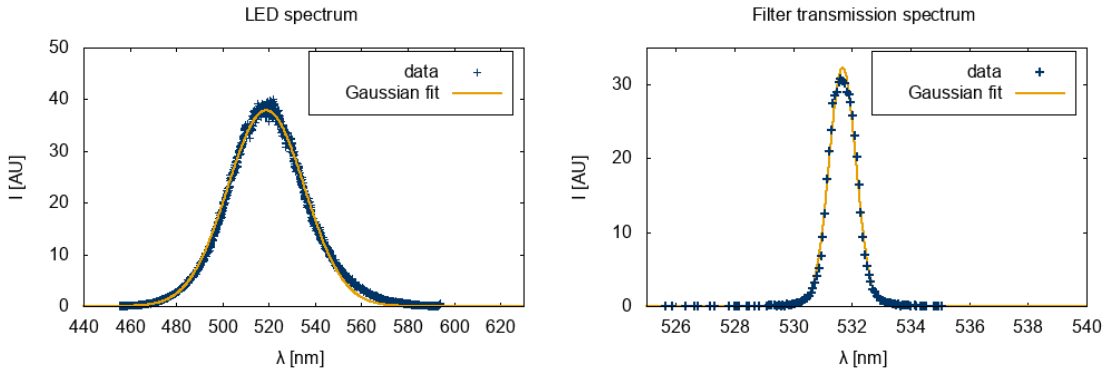

Figure 4.9.: Wavelength spectrum of the LED and the interference filter used for keeping the optical bandwidth small.

In contrast to the mercury lamp the LED has a broad optical wavelength spectrum shown in figure 4.9 on the left. Applying a Gaussian fit the width of the spectrum turns out to be FWHM $\approx 39\,\mathrm{nm}$. Especially since the LED power can be increased to measure even at $\Delta\lambda = 1\,\mathrm{nm}$ photon count rates of about $\dot{N} = 10\,\mathrm{MHz}$ per PMT optical filtering increases the significance at a given measurement time. Thus an optical filter acting as a Fabry-Perot interferometer is used, its transmission spectrum is shown in figure 4.9 on the right. Again a Gaussian fit is applied, the filter width which directly determines $\Delta\lambda$ is

$$\Delta\lambda_{\mathrm{FWHM}} = (1.076 \pm 0.006)\,\mathrm{nm} \tag{4.21}$$

Not only the effective linewidth but also the shape of the spectrum of the detected light is now predominantly defined by the filter transmission spectrum. Therefore there is no need to know the exact light emission profile of the LED to determine the $g^{(2)}$ function but rather important is to know the filter function which is achieved by the fit in figure 4.9 on the right. According to the Wiener-Khinchine theorem the theoretical $g^{(2)}$ function can be determined out of the filter function which is proportional to $F(\omega)$.

4.3.2. Parallel and perpendicular polfilters

Since the optical bandwidth of the LED even after optical filtering to 1 nm is still orders of magnitude above the line width of the mercury lamp, the measurement times to see significant signals increase drastically. Furthermore the absolute height of the signal decreases, a stable baseline on an even lower fluctuation level is

necessary to obtain a reasonable signal analysis. This necessitates taking a reference measurement with perpendicular oriented polarization filters to take systematics of the system into account. This can also be seen in figure 4.10, where the results of the LED measurement is shown. Here $T = 29\,\mathrm{hr}$ of data both for parallel and for perpendicular measurements with varying photon rates between 7 and 11 MHz per PMT [4] are shown.

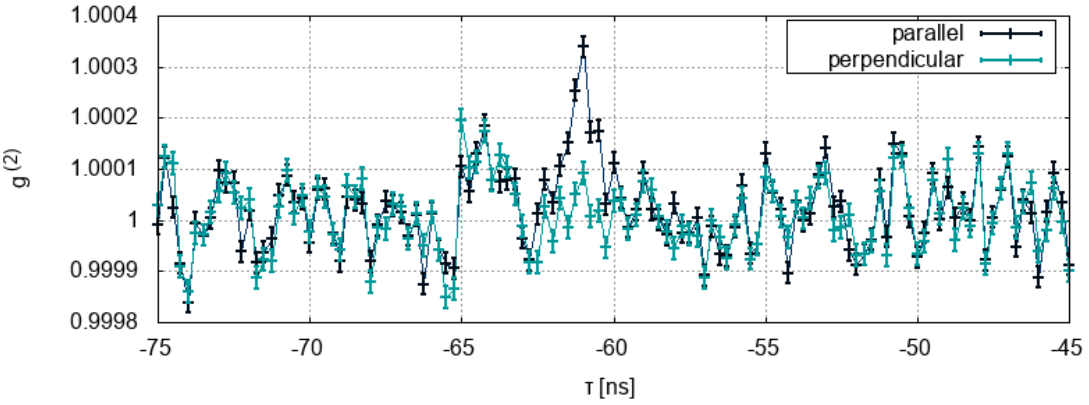

Figure 4.10.: LED measurement with parallel and perpendicular oriented polarization filters

In comparison to the mercury lamp measurement a different cable delay is used, the bunching peak is now expected to be at $\tau \approx -61\,\mathrm{ns}$ and - indeed - one can see an enhancement of the parallel measurement compared to the perpendicular. However, the peak is now in the same order of magnitude as the baseline oscillation which is apparently not stable on the level of 10^{-4}, but the oscillations appear in both measurements so that they cancel out by subtraction as visible in figure 4.11. When subtracting the RMS in the outer regions is extremely close to expectations[5]: Since the rates are fluctuating one cannot just use the same formula like in equation 4.7 but has to divide the total 29 hours into smaller parts and evaluating the cumulative statistical expectation. Doing this one obtains a theoretical RMS of $\sigma_{\mathrm{theo}} = 3.00 \cdot 10^{-5}$ the experimental RMS is $\sigma_{\mathrm{exp}} = 3.32 \cdot 10^{-5}$. This allows for adding theoretical error bars to the non-subtracting $g^{(2)}$ functions of figure 4.10 since the oscillations are of systematical nature.

[4] Obviously the LED does not shine with a constant brightness during the entire measurement time

[5] in contrast to the non-subtracting $g^{(2)}$ functions where the oscillations raise the RMS

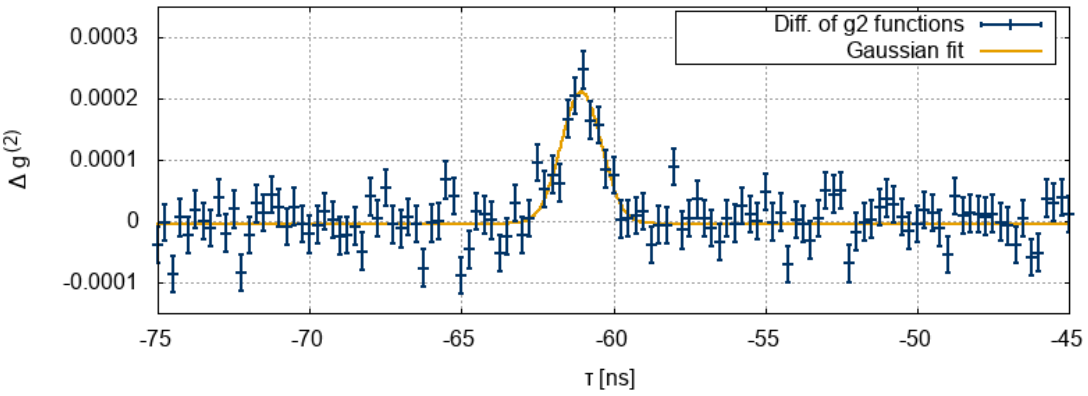

Figure 4.11.: The difference of the $g^{(2)}$ functions of measurements with the LED with parallel and perpendicular oriented polfilters.

4.3.3. Signal analysis

In figure 4.11 a Gaussian fit was applied just like in section 4.2 with the following parameters

- The amplitude A decreased compared to the mercury lamp measurement as already mentioned.

$$A = (2.1 \pm 0.2) \cdot 10^{-4} \tag{4.22}$$

- The medium changed as well due to the longer cable

$$\mu = (-61.05 \pm 0.08)\,\text{ns} \tag{4.23}$$

- The width determined by the time resolution should not change and - concerning the uncertainties - it does not

$$\sigma = (659 \pm 73)\,\text{ps} \tag{4.24}$$

The significance of the signal according to formulas 4.14 and 4.15 turns out to be

$$n = 13.1 \pm 1.4 \tag{4.25}$$

which clearly shows that the LED is (at least partially) a thermal light source producing photon bunching and can be used as a simulation of a star in the lab.

Furthermore it can be checked if the signal is consistent with theory. The integrated Gaussian signal originating from the fit parameters is

$$S_{\text{exp}} = A\sigma\sqrt{2\pi} = (0.35 \pm 0.05)\,\text{ps} \tag{4.26}$$

In contrast the theoretical value from integrating the theoretical $g^{(2)}$ curve of a Gaussian-shaped thermal source according to equations 2.17 and 2.18 in section 2.3 is

$$S_{\text{theo}} = \tau_{\text{c, Gaussian}} = \underbrace{0.77}_{\text{spatial losses}} \cdot \underbrace{0.667}_{\text{Gaussian-shaped}} \cdot \frac{\lambda_0^2}{c \cdot \Delta\lambda_{\text{FWHM}}} = 0.45\,\text{ps} \tag{4.27}$$

for $\lambda_0 = 531.6\,\text{nm}$ and $\Delta\lambda_{\text{FWHM}} = 1.076\,\text{nm}$ which come from the fit in figure 4.9. The theoretical result is thus two standard deviations away from the measurement, hence there are additional losses not mentioned yet. The most reasonable loss originates in the imperfect arrangement of the polarization filters. If they are not fully parallel oriented one loses signal. Same holds for the perpendicular measurement. If they are not perfectly perpendicular oriented one measures signal that will be subtracted afterwards. Both cases reduce the effective measured signal which can explain the loss.

4.3.4. Significance at shorter measurement times

The correlation signal was clearly measured within a time range of 58 hr divided in 29 hr parallel and 29 hr perpendicular. However, when moving on to stars it is indispensable to shorten the measurement time. Assuming same conditions like in the lab (optical filter width of $\Delta\lambda_{\text{FWHM}} \approx 1\,\text{nm}$ and photon rates of $\dot{N} \approx 10\,\text{MHz}$ per PMT) one can test how significant the signal is when measuring shorter which can be done using the same 58 hr-measurement since the evaluated measurement time can be chosen arbitrarily from the total measurement.
In figure 4.12 two different combinations of one hour parallel minus one hour perpendicular is evaluated. Especially on the left the signal can already be seen, on the right it is hard to see it by eye, also since the error bars are still quite big. Fitted into the function is again a Gaussian fit, however its width is not being fitted but set to 659 ps which is the outcome of 29 hr and is reasonable to hold for the shorter measurements because the time resolution should not change and otherwise the fit would not work at all.
Same restriction also holds for 3 hr and 5 hr combinations shown in figures 4.13 and 4.14. Again on the left side the signal peak is well visible, on the right even at $T = 5\,\text{hr}$ combinations can be found where the bunching peak only can be surmised. When 29 hr of data for each the parallel and the perpendicular measurement are taken one can divide the measurement in 29 one-hour combinations, 9 three-hour

combinations or 5 five-hour combinations to investigate the fluctuations of different measurement results. From the figures **4.12**, **4.13** and **4.14** the significance can be calculated using equations **4.14** and **4.15**. The results are shown in figures **4.15**, **4.16** and **4.17**. Here the significance of each combination is plotted on the right vertical axis, on the left the reduced chi-squared of the fit determining n and Δn is drawn as well which however should not be overemphasized: Since the error bars are still quite large even at $T = 5\,\mathrm{hr}$ a "good" chi-squared close to 1 represented by the green dashed line is not surprising and does not necessarily connect to a good fit.
The blue dashed line shows the mean significance. After one hour measurement of parallel and perpendicular polfilters (which is in total 2 hours) the mean significance of the bunching signal of the LED is $n_{1\ \mathrm{hour}} = 2.6$, after three hours it is $n_{3\ \mathrm{hours}} = 4.4$ and finally after five hours $n_{5\ \mathrm{hours}} = 5.6$. In general one can demand for $n = 5$ to state having a signal, in this case one needs about 10 hours to measure this significance (5 hours with parallel and 5 hours with perpendicular polfilters). If it can be ensured that the baseline is stable even on different days, in different environments and under different other conditions like another temperature etc. which has not been checked yet it is sufficient to take the reference measurement with perpendicular oriented polarization filters only once with high statistics to create a reference template. This would reduce the required measurement time by the factor 2 for future measurements of the same set-up.

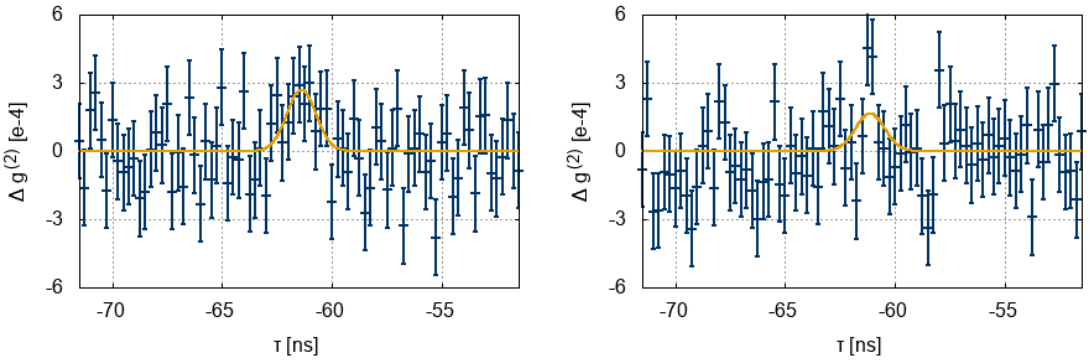

Figure 4.12.: Two 1 hr-combinations, the left one looks quite nice, the right one does not

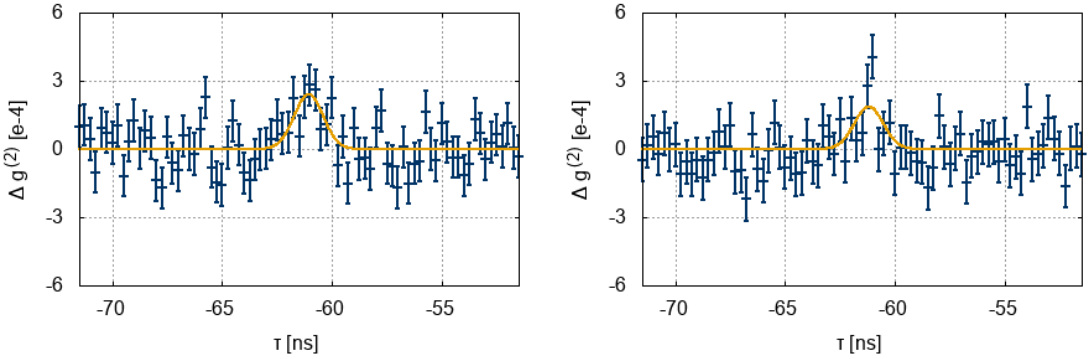

Figure 4.13.: Two 3 hr-combinations, the left one looks quite nice, the right one does not

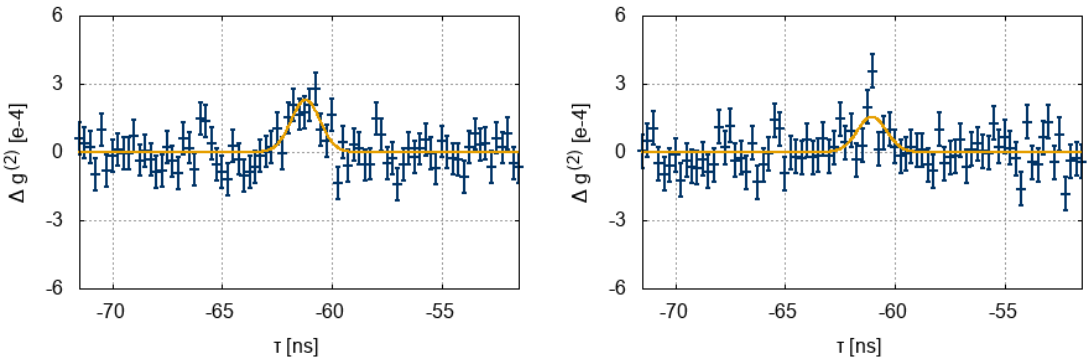

Figure 4.14.: Two 5 hr-combinations, the left one looks quite nice, the right one does not

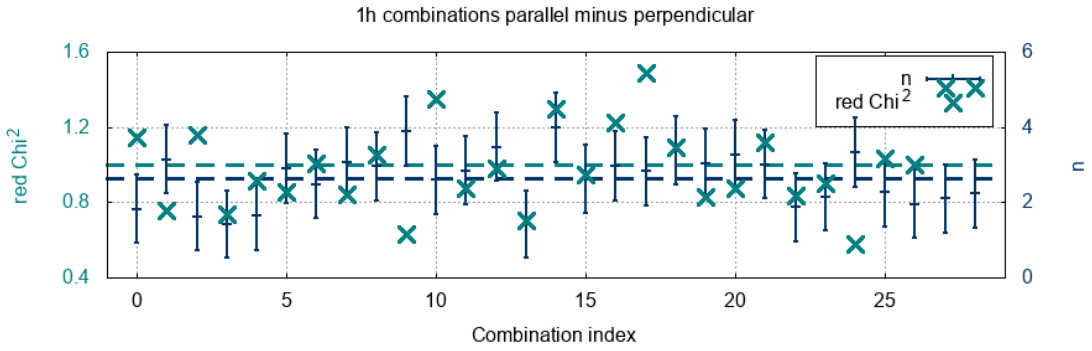

Figure 4.15.: Significances of 29 one-hour combinations of parallel minus perpendicular polfilters.

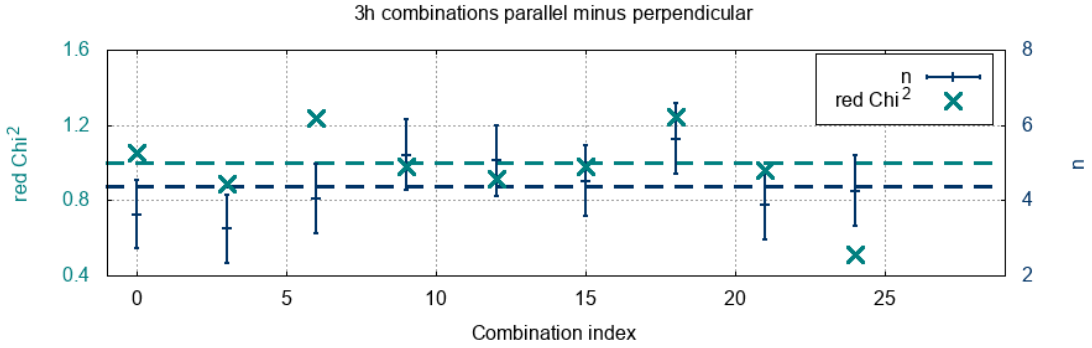

Figure 4.16.: Significances of 9 three-hour combinations of parallel minus perpendicular polfilters.

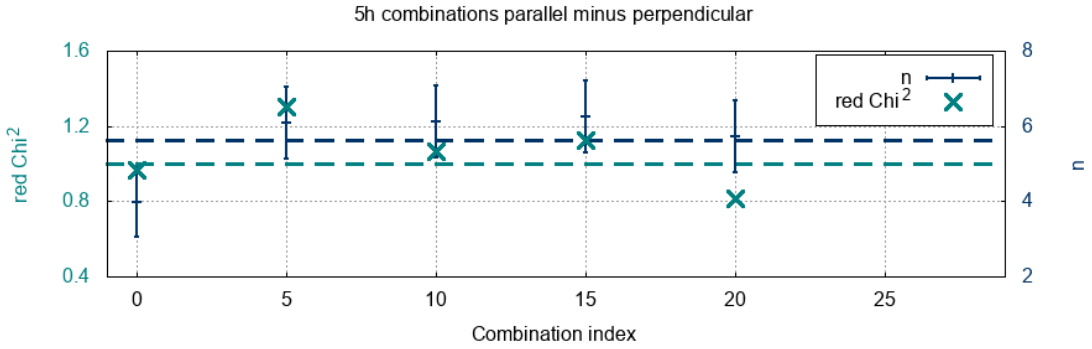

Figure 4.17.: Significances of 5 five-hour combinations of parallel minus perpendicular polfilters.

5.Conclusion and Outlook

When starting the intensity interferometry project first tests with the new digitization card were performed using a laser and a rotating ground glass disc. The convenient setup with a large adjustable coherence time could be used to check the system and to build the software analyzing the time stamps and evaluating the $g^{(2)}$ function. It could be seen that the system works on that big timescales on small statistics and a big binwidth Δt_{bin} well showing the Gaussian-shaped correlation spectra with decreasing coherence time when the rotation speed of the disc was increased.

When moving on to picosecond timescale dominant systematics arised. An oscillation pattern coming from the nonlinearity of the TDC in the digitization card contributed to the signal as well as mobile communication frequencies. While latter could be eliminated by shielding the whole setup and installing low pass filters the TDC-nonlinearity had to be calibrated. Two calibration methods were introduced, either using a non-correlated reference measurement or using information of the same measurement where the signal is expected, but from regions far away from $\tau = 0$ where no correlation should appear. Latter method turned out to be more suitable since noise is reduced here and the measurement time could be halved by not having to take a reference measurement. A cable delay in one of the channels could shift the expected signal into a region in the $g^{(2)}$ function away from zero, since there, still crosstalk-disturbances between the channels remained.

After ensuring that the baseline RMS matched with expectations real thermal/chaotic light sources were investigated. Therefore a mercury lamp with a small linewidth and thus a big correlation signal in the order of $S = 10\,\text{ps}$ where a significant signal can be measured within an hour was used to execute some successful tests like the ability to shift the position of the signal in the $g^{(2)}$ spectrum to an arbitrary position by installing a specific cable delay.

The more challenging light source was a LED having a broad optical spectrum that had to be filtered actively to achieve a measurable signal. An interference filter with a width of $\Delta\lambda \approx 1\,\text{nm}$ yielded a measured signal of about $S = 0.36\,\text{ps}$ which differed from theory by a factor of 20%. Measurements with that small correlation signals need very high statistics accompanying with long measurement times even at high photon rates. On that level of statistics again systematics appeared requiring another reference measurement, this time by installing polarization filters that can be oriented perpendicular to each other to eliminate the correlation. After subtracting the perpendicular measurement again statistics was as expected and the signal could be analyzed. Imperfect adjustments of the filters can explain the loss factor of 20%.

It could be seen that five hours of measuring with parallel polarization filters and three hours with perpendicular polarization filters at photon rates of about $\dot{N} = 10\,\mathrm{MHz}$ and a time resolution of about $\sigma_t = 660\,\mathrm{ps}$ are needed to detect a signal with a significance of $5\sigma_{\mathrm{background}}$. The next step is moving on to measuring the bunching signal of stars which however cannot be tuned to high photon rates like the LED can. Huge collection areas and therefore telescopes are needed. Two IceAct telescopes will be used in Erlangen to perform such measurements. They have a diameter of about half a meter using a Fresnel lens to focus the light (see figure 5.1).

Figure 5.1.: An IceAct telescope in the lab

First tests in the lab are already running, since the light enters the focal plane on different angles interference filtering needs additional parallelization optics that have to be tested. Nevertheless even with this telescope photon rates of $< 5\,\mathrm{MHz}$ are expected observing the brightest stars in the northern hemisphere. Similar restriction also holds for the telescopes of the observatory in Bamberg where measurements are in progress, too. Resuming the relation between the significance of the signal and the required measurement time

$$T = \frac{4n^2\sigma_t c^2(\Delta\lambda)^2}{k^2\lambda_0^4\dot{N}_0\dot{N}_1} \tag{5.1}$$

one can see that T increases by a factor of 4 when both rates will be reduced by a factor of 2 which is the case compared to the LED. This gets even more critical when measuring spatial correlations: The larger the distance between the telescopes the smaller the enhancement of $g^{(2)}(\tau = 0)$ becomes and the longer one has to

measure for a signal with a certain significance. Equation 5.1 reveals parameters that can be adjusted to decrease measuring time:

- Optimizing the time resolution σ_t of the system. However, while in the lab better time resolutions may be achieved by better electronics etc. big telescopes have a time-spread of a few nanoseconds since light that enters the outer parts of the telescopes travels a longer way to the focal plane than light entering near the center. Thus optimizing electronic time resolution has no significant effect on the total time resolution of the advanced system.

- Decreasing the filter width $\Delta\lambda$. As already mentioned small optical filtering gets more and more difficult the larger the telescope area and hence the angles of incoming light become. Furthermore reducing the optical width also reduce the rate which may cancel out in equation 5.1 when all photons can be collected.

- Moving to longer wavelengths can be promising since λ_0 enters the equation with the **fourth power** reducing T. When photo-detectors have a high quantum efficiency at larger wavelengths this can successfully reduce measurement time. In contrast, stars with small angular diameters create a quite large coherence cell on earth which increases linearly with the observed wavelength. Therefore it might become more difficult to sample the $g^{(2)}$ function of such stars on a sufficient large baseline.

- Increasing the rates seems to be the magic bullet in this issue. When telescope diameters of $< 1\,\mathrm{m}$ are too small for measuring high rates one can move to large telescopes with diameters in the order of 10 m. In theory the parameter photon rate has no practical limit since bigger and bigger telescopes could be built.

A telescope array already running is the High Energy Stereoscopic System (H.E.S.S) shown in figure 5.2 which is a Cherenkov telescope built for gamma ray astronomy. It consists of four telescopes with 12 m diameter and a big telescope in the center of the array with a diameter of 28 m. [44]
Since it contains only five telescopes it is not optimal suitable for spatial intensity interferometry only providing a small number of different baselines at once, however it can be used for first tests on really big telescopes and different baselines appear when the position of the star in the sky and thus the projected baseline onto the telescopes changes.
The long-term goal is to implement intensity interferometry electronics in the Cherenkov telescope array CTA, its benefits were already mentioned in section

Figure 5.2.: The H.E.S.S telescope array in Namibia. Taken from [44]

1.3.2. It could give high-significant correlation signals of innumerable different baselines within seconds.
As already mentioned when measuring at really high photon rates in the order of GHz the time-stamping method cannot be used any more but photo-current correlation has to be done. This method requires new electronics and new lab tests before moving to the big telescopes. Thus current correlation is a next big topic in the intensity interferometry research group at ECAP.
All in all the concept of intensity interferometry can open up a new era of stellar astronomy measuring the sizes of even the smallest stars, galaxies, exoplanets etc. even at different wavelengths to see if objects have different sizes in different colors.

A.List of Figures

B.List of Tables and Abbreviations

List of Tables

List of Abbreviations

HBT Hanbury Brown-Twiss
TDC Time-to-digital-converter
PMT Photo-multiplier tube
RMS Root mean square
CTA Cherenkov telescope array
ECAP Erlangen Centre for Astroparticle Physics
LED Light-emitting diode

Bibliography

[1] Robert Hanbury Brown and Richard Q. Twiss. "2. A Test of a New Type of Stellar Interferometer on Sirius". In: *A Source Book in Astronomy and Astrophysics, 1900-1975* (). DOI: 10.4159/harvard.9780674366688.c4.

[2] R. Hanbury Brown, J. Davis and L. R. Allen. "The Angular Diameters of 32 Stars". In: *Monthly Notices of the Royal Astronomical Society* 167.1 (1974), pp. 121–136. DOI: 10.1093/mnras/167.1.121.

[3] *Angular Diameter | COSMOS*. Called up: October 10, 2018. URL: http://astronomy.swin.edu.au/cosmos/A/Angular+Diameter.

[4] Mark Fox. *Quantum optics: an introduction*. Oxford University Press, 2007, pp. 13–14.

[5] *The Rayleigh Criterion*. Called Up: November 30, 2018. URL: http://hyperphysics.phy-astr.gsu.edu/hbase/phyopt/Raylei.html.

[6] WELT. *Weltraumbeobachtung: Groesstes Teleskop der Welt soll Einsicht in Dunkle Materie bringen - WELT*. 2017, Called up: October 29, 2018. URL: https://www.welt.de/wissenschaft/article164986333/Groesstes-Teleskop-der-Welt-soll-Einsicht-in-Dunkle-Materie-bringen.html.

[7] E. O'Gorman et al. "The inhomogeneous submillimeter atmosphere of Betelgeuse". In: *Astronomy & Astrophysics* 602 (2017). DOI: 10.1051/0004-6361/201731171.

[8] information@eso.org. *ALMA - das Atacama Large Millimeter/submillimeter Array*. Called up: October 10, 2018. URL: https://www.eso.org/public/germany/teles-instr/alma/.

[9] D. Mozurkewich et al. "Angular Diameters of Stars from the Mark III Optical Interferometer". In: *The Astronomical Journal* 126.5 (2003), pp. 2502–2520. DOI: 10.1086/378596.

[10] Tabetha Boyajian et al. "Stellar diameters and temperatures VI. High angular resolution measurements of the transiting exoplanet host stars HD 189733 and HD 209458 and implications for models of cool dwarfs". In: *Monthly Notices of the Royal Astronomical Society* 447.1 (2014), pp. 846–857. DOI: 10.1093/mnras/stu2502.

[11] John Davis. *Forty Years of Progress in Long-Baseline Optical Interferometry: 2005 Robert Ellery Lecture*. Called up: October 11, 2018. URL: http://www.publish.csiro.au/AS/Fulltext/as06012.

[12] Mark Fox. *Quantum optics: an introduction*. Oxford University Press, 2007, pp. 16–19.

[13] *F-Praktikum experiment 45: Photonenstatistik*. 2017, Called up: October 16, 2018. URL: http://www.fp.fkp.uni-erlangen.de/fortgeschrittenen-praktikum/versuchsangebot-fuer-bsclanf/BSc-Versuchsanleitungen/B45.pdf.

[14] Ingolf V. Hertel and Claus-Peter Schulz. *Atoms, Molecules and Optical Physics*. Springer, 2015, pp. 72–75.

[15] Mark Fox. *Quantum optics: an introduction*. Oxford University Press, 2007, pp. 115–117.

[16] Gordon. *The physics of Hanbury Brown–Twiss intensity interferometry: from stars to nuclear collisions*. 1998, Called up: October 15, 2018. URL: https://arxiv.org/abs/nucl-th/9804026.

[17] Gordon Baym. *Lectures on quantum mechanics*. Benjamin, 1969, pp. 431–434.

[18] Leonard (1927-2001). Mandel and Emil Wolf. *Optical coherence and quantum optics*. Cambridge University Press, 1995, pp. 188–193.

[19] Eugene Hecht. *Optics*. Addison-Wesley, 1974, pp. 411–418.

[20] *You could learn a lot from a ducky: the van Cittert-Zernike theorem*. 2010, Called up: October 19, 2018. URL: https://skullsinthestars.com/2010/06/12/you-could-learn-a-lot-from-a-ducky-the-van-cittert-zernike-theorem/.

[21] *Ducklings Jumping Into Water*. Time: 0:44 min, 2016, Called up: October 19, 2018. URL: https://www.youtube.com/watch?v=-DJtwZ_-2eY.

[22] Peter Deiml. "Investigation of Microparticle Suspensions using Statistical Optics". MA thesis. Friedrich-Alexander Universität Erlangen-Nürnberg, 2015, pp. 9–11.

[23] Joseph W. Goodman. *Introduction to Fourier optics*. 2nd ed. McGraw-Hill, 1996, pp. 75–79.

[24] R. Hanbury Brown and R. Q. Twiss. "Correlation between Photons in two Coherent Beams of Light". In: *Nature* 177.4497 (1956), pp. 27–29. DOI: 10.1038/177027a0.

[25] *Chile*. Called up: October 22, 2018. URL: https://www.cta-observatory.org/about/array-locations/chile/.

[26] *Detecting Cherenkov Light*. Called up: October 22, 2018. URL: https://www.cta-observatory.org/about/how-cta-works/.

[27] J.M. Schonkeren, H. Kater and L.J. Thompson. *Photomultipliers*. Electronic components and materials Bd. 1. Philips Gloeilampenfabrieken, 1970, p. 4.

[28] Hamamatsu. *Preliminary - H10770(P)B-40/-50 Specifications*. 2009, Called up: November 5, 2018. URL: http://labrigger.com/blog/datasheets/H10770B.pdf.

[29] Hamamatsu Photonics K.K. *Photomultiplier Tubes Basics and Applications*. 3rd ed. 2007, pp. 37–38.

[30] PicoQuant GmbH. *PAM 102 Pre-amplifier Module*. 2018, Called up: November 5, 2018. URL: https://www.picoquant.com/images/uploads/downloads/pam102.pdf.

[31] Michael Wahl. *Time-Correlated Single Photon Counting*. Called Up: December 18, 2018. URL: https://www.picoquant.com/images/uploads/page/files/7253/technote_tcspc.pdf.

[32] PicoQuant GmbH. *Time Harp 260 TCSPC and MCS board with PCIe interface*. 2018, Called up: November 5, 2018. URL: https://www.picoquant.com/images/uploads/downloads/timeharp260.pdf.

[33] *ROOT a Data analysis Framework*. Called up: September 27, 2018. URL: https://root.cern.ch/.

[34] Andre Pscherer. "Measurement of photon bunching on pico second time scales". MA thesis. Friedrich-Alexander Universität Erlangen-Nürnberg, 2016, pp. 34–36.

[35] *Bundesnetzagentur fuer Elektrizitaet, Gas, Telekommunikation, Post und Eisenbahnen*.

[36] *Welche Frequenzen nutzt der Mobilfunk in Deutschland*. Called Up: November 20, 2018. URL: http://www.informationszentrum-mobilfunk.de/technik/funktionsweise/frequenzen.

[37] Mini-Circuits. *MMIC Reflectionless Low Pass Filter XLF-42M+ datasheet*.

[38] Advanced Laser Diode Systems A.L.S. GmbH. *Picoseond Diode Laser (Serial number 821)- PiLas Manual*. 2015.

[39] *Lesson Four - Introduction to Energy Efficiency and P2 in Lighting*. Called up: November 8, 2018. URL: http://my.ilstu.edu/~gjin/p2/Lighting_P2_in_Energy/Lighting_P2_in_Energy7.html.

[40] *Harvard Natural Sciences Lecture Demonstrations*. Called up: November 7, 2018. URL: https://sciencedemonstrations.fas.harvard.edu/presentations/collisional-broadening.

[41] W. R. Hindmarsh, A. D. Petford and G. Smith. "Interpretation of Collision Broadening and Shift in Atomic Spectra". In: *Proceedings of the Royal Society A: Mathematical, Physical and Engineering Sciences* 297.1449 (1967), 296?304. DOI: 10.1098/rspa.1967.0068.

[42] Called up: November 7, 2018. URL: http://www.lamptech.co.uk/Documents/M9MB.htm.

[43] Asif Shaik. *Physics and Radio-Electronics - Free Online Tutorials*. Called Up: November 19, 2018. URL: https://www.physics-and-radio-electronics.com/.

[44] *ECAP Friedrich-Alexander Universitaet Erlangen-Nuernberg, The High Energy Stereoscopic System*. Calle up: November 15, 2018. URL: https://ecap.nat.fau.de/index.php/research/gamma-ray-astronomy/h-e-s-s/.

Danksagungen

Zu guter Letzt gibt es die obligatorischen aber teils auch berechtigten Danksagungen an einige Wegbegleiter während der Arbeit. Dazu zählen natürlich in erster Linie diejenigen, die direkt an unserer Forschung beteiligt sind und mir die Möglichkeit geben, ein Teil davon zu sein.

Gisela Anton für ihre sehr angenehme Art der Betreuung, ihre Mühen, sich immer wieder in meine Probleme einzudenken und ihre Offenheit für Diskussionen.

Thilo Michel für seine Co-Betreuerschaft, sein gewitztes und direktes Naturell und seine Unkonventionalität.

Peter Deiml für die hervorragende Art der Zusammenarbeit und Ausführung seiner Mentorenschaft. Dafür, dass ich ihn jederzeit mit meinen Fragen und Herausforderungen konfrontieren konnte und er diese ohne ein Wort der Beschwerde sofort aufgenommen und bearbeitet hat.

Adrian Zink für seine amüsant rationalen Gedanken und die Gewissheit, dass jedes elektronische Problem am nächsten Tag bereits gelöst ist.

Stefan Funk für seine kompetente und erfrischende Leitung unseres Meetings sowie seinen Überblick und seine wichtige Strukturierung unserer Forschungsgruppe.

Speziell die Zusammenarbeit mit Peter und Adrian ist hier hervorzuheben, aus der etliche Gedanken und Umsetzungen dieser Arbeit entstanden sind. Darüber hinaus konnte ich in den Genuss kommen, meinen Büroalltag täglich mit einer außergewöhnlichen Mischung an humorvollen Kollegen zu verbringen, die Freud und Leid freiwillig wie unfreiwillig mit mir teilen mussten.
Hierbei danke ich **Basti** für seinen humoristischen Ideenreichtum, seine allumfassende Hilfsbereitschaft und die zahllosen Pizza-Abende beim Tio, **Dennis** für unterhaltsame Gespräche oberhalb der Bildschirmkante aber unterhalb der Gürtellinie und seine (manchmal eigentlich unangebrachte) Ehrlichkeit in allen Situationen, **Franzi** dafür, dass sie jeden Spaß zumindest äußerlich mitmacht und für ihre ulkige, aber wenn nötig jederzeit ernste Erscheinung, weiterhin **Johannes** für seinen geschärften Sinn für gute Unterhaltung unsererseits, sowie dafür, dass er seine breite Brust nie verliert, **Michi T.** für die beinahe selbstlosen Begleitungen auf dem schönen Rückweg von der Mensa, seine Allzeitbereitschaft für Schabernack

und seine grundsätzliche erfrischende Dreistigkeit. Ich danke meinem einzigen echten Sitznachbarn **Michi W.** für die konsequente Ausübung seines ideologischen Lehrauftrags in sämtlichen Fachbereichen, sowie für kompetente Hilfe und Rat bei diversen fachlichen und organisatorischen Angelegenheiten, **Naomi** für ihre einzigartig interessante Persönlichkeit, ihre ansteckende Natürlichkeit und ihre Pommes in der Mensa, **Patrick** für die viel zu unregelmäßigen Tischtennispartien und einen Hauch von Seriösität, der mit ihm durch die Fluren wehte, und schließlich **Tobi** für seine überdurchschnittliche Anzahl an Berechtigungen im digitalen Bereich, seine heroische Organisation der Tollen Team Tage und sein entspanntes Gemüt.
Weiterhin möchte ich mich bei **Daniel** für das Lesen und Korrigieren dieser Arbeit fernab jeglicher fachlicher Zusammenarbeit bedanken und außerdem noch allen Anderen, die aufgrund der Kürze unserer Begegnung keinen persönlichen Platz in den Danksagungen erhalten haben.

Abschließend gilt natürlich noch besonderer Dank **meinen Eltern**, dafür, dass sie mir zu Hause eine absolute Wohlfühloase schaffen und mich in all meinen Entscheidungen ohne offensichtliches Nörgeln unterstützen. Zurecht werde ich regelmäßig daran erinnert, dass es mir eigentlich viel zu gut geht!

Statutory Declaration

I declare that I have developed and written the enclosed Master Thesis completely by myself, and have not used sources or means without declaration in the text. The Master Thesis was not used in the same or in a similar version to achieve an academic grading or is being published elsewhere.

Erlangen, December 19, 2018